

MECHANICAL BUCKLING OF INDIVIDUAL SILICON NANORIBBONS
ON A COMPLIANT SUBSTRATE

by

Siang Yee Chang

A dissertation submitted to the faculty of
The University of North Carolina at Charlotte
in partial fulfillment of the requirements
for the degree of Doctor of Philosophy in
Mechanical Engineering

Charlotte

2017

Approved by:

Dr. Terry T. Xu

Dr. Howie Fang

Dr. Haitao Zhang

Dr. Thomas Schmedake

Dr. Xinghua Shi

©2017
Siang Yee Chang
ALL RIGHTS RESERVED

ABSTRACT

SIANG YEE CHANG. Mechanical buckling of individual Silicon nanoribbons on a compliant substrate. (Under the direction of DR. TERRY T. XU)

About a decade ago, mechanical buckling evolves as a promising metrology to rapidly measure the elastic moduli of thin films and one-dimensional (1D) nanostructures. This form of metrology translates the geometrical measurements of the buckling profile into material property value. The strategy applied in the mechanical buckling-based metrology consists of three steps: i) applying pre-strain to the compliant substrate, ii) depositing or transferring 1D nanostructures onto the surface of the pre-strained compliant substrate, and iii) releasing the pre-strain of the compliant substrate so as to allow it to return to its original dimensions. The release of the pre-strain on the compliant substrate induces a compressive stress on the strain-free 1D nanostructures which later buckle spontaneously into sinusoidal shape in order to relieve the compressive stress. Using the Newtonian mechanics model, previous researchers developed a relation to identify the elastic properties of the 1D nanostructures by correlating the buckling wavelength with materials and geometric parameters of the system. However, previous work mainly emphasized on application of small strain (less than 40%), and single material system of relatively long and having equal moment of inertia (*e.g.* circular or hexagon). Without acknowledging the existence of the native sheath layer surrounding the nanostructures could lead to measurement error of ~15% or more.

In this dissertation work, silicon nanoribbons of variable aspect ratios (width B ranging 40, 60, 80, 100 and 200 nm, and constant thickness H of 30 nm) were individually deposited on a 100% pre-strained elastomeric (polydimethylsiloxane, PDMS) substrate. Since the as-fabricated Si nanoribbons consist of native oxide layer

of ~5 nm, the core-sheath structure had to be accounted for the property measurement where the effective modulus was being considered. Upon relaxing the 100% pre-strain on the pristine substrate, Si nanoribbons showed increased buckling wavelength as a function of aspect ratio, owing to the greater effective Young's modulus in larger ribbons. On the other hand, the standard deviation of the measured buckling wavelength was considerably high ~20%, possibly resulted from the increased of area moment of inertia as the ribbons were not placed perfectly flat on the substrate surface during the transfer process.

In terms of buckling mode, three forms of buckling mode were observed in this work, in general. In-plane buckling mode was observed on ribbons having aspect ratio $B/H < 1.20$, whilst ribbons with aspect ratio greater than 1.20 exhibited out-of-plane buckling mode. The findings was in good agreement with the adopted analytical solution which suggested that $B/H \approx 1.14$ is transition point of the buckling mode. Meanwhile, out-of-plane buckling mode observed in this work can be divided into two variants, *i.e.* incline-to-plane and normal-to-plane. Ribbons with $1.68 \leq B/H \leq 2.70$ buckled incline-to-plane with excessive incline angle with respect to the normal direction of substrate surface, in which the asymmetrical feature of the ribbons and application of 100% pre-strain were accounted for this observation. In contrast, normal-to-plane buckling mode was predominant in ribbons having larger aspect ratio *i.e.* $B/H = 5.12$, not forgetting that half of the widest ribbons failed to buckle.

In the existing models, perfect bonding is assumed between the two constituents of the buckled system. However, in practical, the adhesion between nanostructures and substrate is ambiguous. Thus, ultra-violet/ozone (UVO) surface treatment was employed to improve the interfacial adhesion and its effect on the ribbon buckling profile was investigated. UVO treatment increased hydrophilicity of the substrate

surface, which helped to enhance chemical bonding at the interface between ribbon and substrate. Though so, the treatment had insignificant effect on the buckling profile since UVO treatment only altered the surface modulus of substrate within tens of nanometer. Whilst the overall bulk modulus of the substrate remained unaffected, no substantial variations in the buckling wavelength was observed as compared to that of untreated system. Nevertheless, the treatment seemed to improve the interfacial adhesion marginally for ribbons having aspect ratios 2.70 and 5.12. Besides, it was also evidenced from the AFM topographic images that substrate surface suffered from depression at regions where peaks or valleys of the buckled ribbons formed, in the event of treatment duration lasted 150 s. This further affirmed that UVO treatment is an effective technique to enhance ribbon-substrate interfacial properties. Additionally, transition of buckling mode as a function of treatment duration was not observed in this work owing to the unequal area moment of inertia of the ribbon structure.

ACKNOWLEDGEMENTS

I would like to express my heartfelt gratitude to my advisor Dr. Terry T. Xu for her inspiration, guidance and continuous support throughout my journey as a doctoral student. She demonstrates what a professional scholar should be, with her sharp insight, diligence, competency and patience, and I am indeed inspired to be someone like her. I am also truly indebted to her for guiding me into this very fascinating yet challenging field of nanomaterials, and giving me abundant opportunity to acquire knowledge and skills on cutting-edge characterization tools and techniques. Those precious experiences would definitely be beneficial to me in the future as an independent researcher.

I would also like to thank my former groupmates, Dr. Youfei Jiang and Dr. Zhiguang Cui for their patience, time and selfless support to equip me with valuable techniques and practical skills on handling those sophisticated research equipment in our laboratories. They have been wonderful colleagues to work with, and for without them, my research would have been more challenging than it has already been. Special appreciation goes to our collaborator Dr. Deyu Li's group in the Vanderbilt University for providing samples for my work.

Besides, I also owe thanks to Dr. Jimmie Miller for his endless help on the use of Atomic Force Microscope, Dr. Robert Hudgins and Dr. Lou Deguzman for their valuable support on the use of Laser Scanning Confocal Microscope, Dr. Stuart Smith for sharing his personal lab space and facilities, Franklin Green and Philip Davis for their kind assistance on designing and fabricating the home-built stretching device which served as an important tool in my experimental work. Not forgetting, Dr. Howie Fang and his students for their timely feedback and insightful advice on the simulation work.

I am also wholeheartedly thankful to my friends from the William States Lee College of Engineering, especially to Xiaoxue Chen, Dr. Yuanyuan Lu, Hossein Shahinian, Vahid Hemmati, Shank Kulkarni, James Haig, and Dr. Jason Marmon for their generous help and great companion. Thank to them for the laughter and tears that we shared together along the journey.

I would also like to extend my appreciation to my committee members, Drs. Howie Fang, Haitao Zhang, Thomas Schmedake, and Xinghua Shi for their valuable time and advice for making my dissertation a better one. The financial support from the National Science Foundation (NSF award no. 1308509) and the UNC Charlotte throughout my entire doctoral study are also gratefully acknowledged. Not forgetting, the administrative support from the Universiti Teknikal Malaysia Melaka for allowing me to pursue my doctoral study in the United States.

Most importantly, this dissertation work may not have been possible without the unconditional love and encouragement from my loving family and special one, Soon Han Kee back in Malaysia. Even though we are thousand miles apart, my dearest ones are always there whenever I needed them, to share all the bittersweet and more importantly, to give me strength to move forward. No words can ever thank them enough for their faith and support in me throughout this four-and-a-half year journey.

Finally, this section would not be complete without a special mention about my “second” family in Charlotte - Harvey & Shirley Lyerly and Yuan-Chuin Teng. They have provided me a home away from home, and those days in Charlotte have never been blue with their presence. I indeed cherish all the moment we shared together and those memories will always be my lifetime reminiscence.

TABLE OF CONTENTS

LIST OF TABLES	x
LIST OF FIGURES	xi
LIST OF ABBREVIATIONS.....	xvi
LIST OF SYMBOLS	xviii
CHAPTER 1: INTRODUCTION	1
1.1 Buckling.....	3
1.2 Mechanical buckling as metrology	10
1.3 Mechanical buckling of 1D nanostructures	12
1.4 Core-sheath structure	16
1.5 Buckling mode.....	19
1.5.1 Least energy principle	19
1.5.2 Effect of geometrical parameters	20
1.5.3 Effect of interfacial adhesion	23
1.5.4 Hydrophobic recovery of oxidized substrate	30
1.6 Objectives	31
CHAPTER 2: MATERIALS AND METHODS	33
2.1 Fabrication of silicon nanoribbons	33
2.2 Dimensional study of the silicon nanoribbons.....	35
2.3 Preparation of compliant substrate from polydimethylsiloxane (PDMS) .	36
2.4 Fabrication of stretching device.....	37
2.5 Mechanical buckling.....	38
2.6 Surface treatment of the PDMS substrate.....	39
2.7 Measurement and analysis of ribbon buckled profile.....	40
CHAPTER 3: EXPERIMENTAL RESULTS AND DISCUSSION	42
3.1 Dimensional study of silicon nanoribbons.....	42
3.1.1 Effect of core-sheath structure on the ribbon bending stiffness.....	46
3.2 Buckling of Si nanoribbons as a function of ribbon aspect ratio.....	47
3.2.1 Measurement techniques of buckling wavelength	48
3.2.2 Buckling wavelength as a function of ribbon aspect ratio	51
3.2.3 Buckling mode as a function of ribbon aspect ratio.....	54
3.3 Effect of surface treatment on buckling of Si nanoribbons	62

3.3.1	Effect of aging on wettability of treated substrate	62
3.3.2	Buckling wavelength as a function of surface treatment	65
3.3.3	Buckling mode as a function of surface treatment	67
CHAPTER 4: MECHANICS OF BUCKLED NANORIBBON ON A COMPLIANT SUBSTRATE.....		73
4.1	In-plane buckling mechanism	73
4.1.1	Nanoribbon	73
4.1.2	Substrate	75
4.1.3	Potential energy	77
4.1.4	Approximation of in-plane buckling strain	78
4.2	Out-of-plane buckling mechanism.....	79
4.2.1	Nanoribbon.....	79
4.2.2	Substrate	79
4.2.3	Potential energy	81
4.2.4	Approximation of out-of-plane buckling strain	82
4.3	Competition on buckling mode.....	83
CHAPTER 5: FINITE ELEMENT MODELING OF MECHANICAL BUCKLING		86
5.1	Modeling pre-straining of PDMS substrate	86
5.1.1	Determining the substrate strain energy potential.....	86
5.1.2	Mesh convergence analysis on the substrate pre-straining	91
5.1.3	Simplification of substrate pre-straining model	92
5.2	Modeling mechanical buckling of Si nanoribbons	95
CHAPTER 6: CONCLUSIONS & FUTURE WORK		96
6.1	Conclusions.....	96
6.2	Future work.....	97
REFERENCES		100

LIST OF TABLES

Table 1.1: Existing literature on the buckling mechanics of 1D micro/nanostructures on a compliant substrate (N – not reported).....	17
Table 3.1: Targeted dimensions of as-fabricated silicon nanoribbons.	43
Table 3.2: Average dimensions of as-fabricated Si nanoribbons.	45
Table 3.3: Comparison of wavelength and amplitude measurements of an in-plane-buckled Si nanoribbon using optical and atomic force microscope.....	49
Table 3.4: Comparison of wavelength and amplitude measurements of an out-of-plane-buckled Si nanoribbon using optical and laser scanning confocal microscope.	50
Table 3.5: Height measurements of Si nanoribbons laid flat on the PDMS substrate surface acquired through tapping mode AFM.	56
Table 3.6: Effect of treatment duration on the buckling mode of Si nanoribbons of various aspect ratios under 100% pre-strain.	69
Table 5.1: Dimensions and reaction force of 100% elongated substrate captured during the transition of tension-compression process, as a function of mesh size.	92
Table 5.2: Mesh convergence analysis of compressed substrate based on its width and thickness dimensions.	94

LIST OF FIGURES

Figure 1.1: Schematic diagram of thermally-driven buckling of a bilayer system of Au-coated polydimethylsiloxane (PDMS) substrate. ¹⁹	4
Figure 1.2: Buckling of a 50 nm gold film on a thick elastomer (PDMS) substrate. The unpatterned left region of the substrate displayed the herringbone pattern while the right region which has been patterned with alternating flat depressions exhibited ordered wavy pattern. ²⁵	5
Figure 1.3: Schematic diagram of swelling-driven buckling process. ²³	6
Figure 1.4: Schematic representations of reversible wrinkle channels in a microfluidic system. The wrinkle channels are opened and closed reversibly in response to the introduction of ethanol. Green food dye and red one were used to distinguish water and ethanol, respectively. ²¹	7
Figure 1.5: Two sets of sequential optical microscope images of two equally stretched PDMS samples (20% strain, from 25 to 30 mm on both edges) subjected to two different releasing processes, (a–j) sequentially and (m–r) simultaneously, respectively, and their corresponding illustrative sketches (k–l) and (s), accordingly. Scale bar in (a) is applicable to all images. ²⁷	8
Figure 1.6: Three sequential configurations for the thin film/substrate buckling process under mechanical force. The top figure shows the undeformed substrate with the original length L_0 . The middle figure shows the substrate deformed by the pre-strain ϵ_{pre} and the integrated film. The bottom figure shows the deformed (buckled) configuration. ²⁸	9
Figure 1.7: (a) Optical microscopy image of a PS gradient film showing the increase in buckling wavelength with film thickness. (b) Measured buckling wavelength (open circles) and calculated Young's modulus (closed circles) for the PS gradient film as a function of film thickness. The Young's modulus computed from Eq. 1.1 remains constant with thickness over this range, varying little from its average value of $3.4 \text{ GPa} \pm 0.1 \text{ GPa}$. ⁹	11
Figure 1.8: (a) Transfer of aligned arrays of SWNTs grown on quartz to a uniaxially strained substrate of PDMS followed by release of the pre-strain (ϵ_{pre}) causes nonlinear buckling instabilities in the SWNT that lead to wavy configurations. (b) Large-area ($12 \mu\text{m} \times 12 \mu\text{m}$) angled-view atomic force microscope (AFM) image of wavy SWNTs on a PDMS substrate. (c) Plane-view AFM image of an individual wavy SWNT and line-cut showing the profile of relief. The red, black, and blue curves represent measured data, a piecewise sinusoidal fit, and a global sinusoidal fit, respectively. The dashed ovals indicate regions that represent abrupt shifts in the phase. The wavelength determined by the piecewise fit is $160 \pm 20 \text{ nm}$. ¹⁴	13
Figure 1.9: (a) Energy difference between normal and in-surface buckling ¹² , and (b) comparison between the energy difference and adhesion energy between SiNWs and PDMS ¹³ , as a function of SiNW radius.	20

- Figure 1.10: (a) Schematic diagram of the electrospinning process for micro/nanofiber fabrication. (b), (c) Straight fibers deposited on the pre-strained PDMS substrate and their cross-sections when the nozzle-to-substrate distance (d in (a)) is 2 mm (b) and 8 mm (c). (d), (e) Straight fibers in (b) and (c) buckle out-of-plane (d) and in-plane (e) respectively when releasing the pre-strain of the PDMS substrate. The right columns of (d) and (e) are the 3D views of the left 2D graphs.³⁵21
- Figure 1.11: (a) The critical buckling strains for both in-plane and out-of-plane buckling when $Ib_1 = Ib_2$. (b) The critical buckling strains when $Ib_1 = Ib_2$ and $ES / Eb = 1.9 \times 10^{-5}$. The right columns of (b) are FEA results of stiff layers with square, circular and regular hexagon cross sections buckle in-plane on elastomer. (c) The critical out-of-/in-plane buckling strains of rectangular cross-section. (d) The critical out-of-/in-plane buckling strains of rectangular cross-section when $\bar{E}S / Eb = 1.9 \times 10^{-5}$. The right columns of (b) are FEA results when $H / W = 0.87$ and $H / W = 1$, out-of-plane buckling and in-plane buckling occurs, respectively.³⁵22
- Figure 1.12: Illustration of the surface chemistry of PDMS and reactions occurring at the interfaces between PDMS and semiconductor nanoribbons covered with thin SiO₂ layers.⁴⁵24
- Figure 1.13: (Left) water contact angle as a function of UVO treatment and post-treatment time and (right) images showing water contact angles at different treatment times (0, 20, 30, 50, and 90 min, immediately after UVO treatment).⁵²26
- Figure 1.14: AFM images of deformed Si NWs on the PDMS substrate at different treatment times of (a) 0 min, (b) 3 min, (c) 5 min, (d) 8 min, and (e) 20 min. The pre-strains were all set to be 20%. Scale bar is 1 μm .⁴⁴28
- Figure 1.15: The buckling modes of the SiNW partially bonded to a PDMS substrate. The dots represent the constraints (bonded sites) between the SiNW and the PDMS substrate. Color contour of the maximum principal strain in the buckled configuration is given.⁵⁸29
- Figure 1.16: A schematic showing different zones that are produced on a PDMS as a result of exposure to partial electrical discharge. The uppermost surface is affected mostly, which converts to a silica-like layer. Beneath the silica-like layer, it is envisaged that the scission of polymer chain occurs. The silica-like layer is probably porous or cracked, through which the *in situ* produced low molecular weight species migrate and adsorb at the air-polymer interface. If free fluid is present in the network, it also contributes to the recovery process.⁵⁹31
- Figure 2.1: (a) An SEM micrograph of the as-fabricated silicon nanoribbon array. (b) An HRTEM micrograph of an individual silicon nanoribbon. The inset in (b) shows a SAED pattern of the nanoribbon taken along the $[\bar{1}10]$ zone axis.⁶¹35
- Figure 2.2: An TEM micrograph of a bent silicon nanoribbon laid on a lacey carbon-coated grid for thickness measurement.36

Figure 2.3: Dimensions of compliant substrate following ASTM D412 with 40% reduction in size.	37
Figure 2.4: Home-built stretching device installed in an Instron uniaxial tensile machine.	38
Figure 3.1: Release of silicon nanostructure from a SOI wafer by etching vertically through the top silicon layer to expose the underlying SiO ₂ layer which is later removed by etching in hydrofluoric acid. ⁶⁴	43
Figure 3.2: Crystal orientation of (100) Si wafer used in lithographic patterning.....	44
Figure 3.3: TEM micrographs of Si nanoribbon being (a) laid flat for (b) width measurement, and (c) tilted for (d) thickness measurement. The insets in (b) and (d) show the respective SAED pattern of the nanoribbon taken along the [100] and $[\bar{1}10]$ zone axis.....	44
Figure 3.4: Schematic illustration of a cross-section of our as-fabricated Si nanoribbon having core-sheath structure. Shaded region refers to the Si core, which is surrounded by a thin layer of SiO ₂ sheath.	46
Figure 3.6: Optical microscope imaging of buckling profile of an in-plane-buckled Si nanoribbon on a PDMS substrate (a) prior to and (b) upon release of the pre-strain; (c) atomic force microscope scanning of the buckled ribbon in (b). The arrow in (a) shows the direction of pre-strain application.	49
Figure 3.7: Optical microscope imaging of buckling profile of a Si nanoribbon buckling out-of-plane on a PDMS substrate (a) prior to and (b) upon release of the pre-strain; (c) laser scanning confocal microscope scanning of the buckled ribbon in (b). The arrow in (a) shows the direction of pre-strain application.....	50
Figure 3.8: Buckling wavelength of Si nanoribbons as a function of ribbon width. All ribbons have a constant thickness of ~ 30 nm (exclusive of an oxide sheath layer of ~5 nm thick).....	52
Figure 3.8: Schematic illustration of a ribbon having a rectangular cross-section being tilted at a specified angle α from the substrate surface.	53
Figure 3.9: Optical images of buckled Si nanoribbons of varying aspect ratio (a) 1.19, (b) 1.68, (c) 2.18, (d) 2.70 and (e) 5.12 under 100% pre-strain. Scale bar in (a) is applicable to all images.....	54
Figure 3.10: Plane-view AFM images of wavy Si nanoribbons with aspect ratio of (a) 1.19, (b) 1.68, (c) 2.18 and (d) 2.70. The right panel illustrates the respective topographical scan across the line cut of the buckled ribbon.	57
Figure 3.11: Height and width measurements at the buckle of wavy Si nanoribbons with aspect ratio (a) 1.19, (b) 1.68, (c) 2.18 and (d) 2.70.	58
Figure 3.12: Two forms of out-of-plane buckling mode, (a) incline-to-plane buckling with an inclined bend at the buckle, (b) normal-to-plane buckling.	59

Figure 3.13: Water contact angle as a function of UVO treatment aging time at (a) 90 s and (b) 150 s treatment duration. The red dotted line indicates that water contact angle of pristine PDMS surface.....	63
Figure 3.14: Influence of UVO treatment duration on the buckling wavelength of Si nanoribbons having various aspect ratios. The ribbons are denoted as (B, H) where B is the width and H is the thickness.....	66
Figure 3.15: Influence of UVO treatment duration on the buckling wavelength of Si nanoribbons of constant thickness of 30 nm but different width of (a) 40 nm, (b) 60 nm, (c) 80 nm and (d) 100 nm.	66
Figure 3.16: Buckling mode of Si nanoribbons of different aspect ratio (B/H) as a function of UVO treatment duration t_{uvo} . While all ribbons demonstrated a single buckling mode for the specified treatment duration, ribbons of $B/H = 2.70$ buckled in two modes, (l) in-plane as well as (m) out-of-plane at $t_{uvo} = 150$ s. Scale bar in (a) is applicable to all images.....	71
Figure 3.17: Plane-view AFM images of wavy Si nanoribbons with aspect ratio of (a) 1.19, (b) 1.68, (c) 2.18 and (d) 2.70 on 150 s-treated PDMS substrate. The right panel illustrates the respective 3D surface plot of the buckled ribbon.	72
Figure 4.2: The critical in-plane-/out-of-plane buckling strain of a rectangular cross-section as a function of aspect ratio (B/H) and properties ratio (E_s/E_b)	83
Figure 4.3: Critical in-plane-/out-of-plane buckling strain when $E_s/E_b = 2.65 \times 10^{-5}$ ($E_s = 2$ MPa for PDMS substrate, and $E_b = 101$ GPa for effective Young's modulus of (40, 30) Si nanoribbon with core-sheath structure). Transition point occurs at $B/H \approx 1.138$	84
Figure 4.4: Critical in-plane-/out-of-plane buckling strain when $E_s/E_b = 2.47 \times 10^{-5}$ ($E_s = 2$ MPa for PDMS substrate, and $E_b = 108$ GPa for effective Young's modulus of (200, 30) Si nanoribbon with core-sheath structure). Transition point occurs at $B/H \approx 1.137$	84
Figure 5.1: Comparison of nonlinear fitting results of PDMS sample using various material models available in Abaqus.	88
Figure 5.2: Comparison of computational time between various strain energy potentials associated with the simulation of PDMS substrate hyperelastic behavior.....	89
Figure 5.3: Boundary conditions applied in the finite element modeling of pre-strain of gauge length region of the PDMS substrate (<i>a.k.a.</i> simplified substrate).	90
Figure 5.4: Force-displacement curve of pre-straining simplified substrate model agrees well to that of measured value.	91
Figure 5.5: Boundary conditions applied in the finite element modeling of compression of an elongated gauge length region of the PDMS substrate.....	93

Figure 5.6: Comparison of force-displacement curve of substrate under compression
between actual and simulation.93

LIST OF ABBREVIATIONS

1D	one-dimensional
2D	two-dimensional
3D	three-dimensional
AFM	atomic force microscope
ASTM	American Standard of Test Method
ATR-FTIR	attenuated total reflective Fourier transform infrared spectroscopy
AVE	advanced video extensometer
BOE	buffered oxide etch
BOX	buried oxide
CCD	charged-coupled device
CNT	carbon nanotube
EBID	electron-beam-induced deposition
EBL	electron-beam lithography
FEA	finite element analysis
FEM	finite element modeling
HRTEM	high-resolution transmission electron microscopy
HSQ	hydrogen silsesquioxane
IM	interference microscopy
JKR	Johnson-Kendall-Roberts theory
LSCM	laser scanning confocal microscope
LMW	low molecular weight
MEMS	micro-electromechanical systems
NEMS	nano-electromechanical systems
NIST	National Institute of Standards and Technology

OLEDs	organic light emitting diodes
OM	optical microscope
PDMS	poly(dimethylsiloxane)
PS	polystyrene
PVDF	polyvinylidene fluoride
Poly(HEMA)	poly(2-hydroxyethyl methacrylate)
RIE	reactive ion-plasma etching
SAED	selected area electron diffraction
SEM	scanning electron microscope
SIEBIMM	strain-induced elastic buckling instability for mechanical measurements
SiNR	Silicon nanoribbon
SiNW	Silicon nanowire
SOI	silicon-on-insulator
SWNT	single-wall carbon nanotube
TEM	transmission electron microscope
UV	ultra-violet
UVO	ultra-violet/ozone
XPS	X-ray photoelectron spectroscopy

LIST OF SYMBOLS

a	buckling amplitude
A	cross-sectional area
b	inner width of a beam or ribbon
B	outer width of a beam or ribbon
D	distance between the adjacent constraint points
D	diameter
ε_m	membrane strain in a beam
ε_{pre}	pre-strain applied to a substrate
E	Young's modulus
\bar{E}	plane-strain modulus
F	axial force
h	inner height of a beam or ribbon
H	outer height of a beam or ribbon
I	area moment of inertia
k	wavevector
K	modified Bessel function of the second kind
L_0	original length
R	radius
t	film thickness
T	normal force
u	axial displacement
U_b	bending energy of a nanoribbon
U_m	membrane energy of a nanoribbon
U_s	strain energy of a substrate

U_{tot}	total potential energy
W	width
v	lateral deflection
ν	Poisson's ratio
x	axial direction
λ	buckling wavelength
γ	Euler's constant

CHAPTER 1: INTRODUCTION

Over the last few decades, the synthesis and characterization of one-dimensional (1D) nanostructures have attracted enormous attention as these materials hold great promise as building blocks for a broad range of applications including nanoelectronics, nanosensors, nanocomposites, energy harvesting/storage devices, and nano-electromechanical systems (NEMS).^{1,2} Whilst the synthesis of materials with reduced dimensions is a burgeoning field of research, determining their mechanical properties is of paramount for their effective utilization yet remains challenging. To date, a number of techniques are available to measure the mechanical properties of these materials, which can generally be grouped into two categories based on the instruments involved, namely atomic force microscope (AFM)/nanoindentation testing and *in-situ* electron microscopy testing.^{2,3} Notable test methods include but not limited to, tensile, bending, buckling, fatigue, nanoindentation and resonance vibration test. AFM/nanoindentation testing utilizes commercially available instruments to accurately apply forces in the nano- and pico Newton range and measure deformation in the range of Angstroms. Alternatively, electron microscopy testing requires a separate mechanical testing tool to be installed in the electron microscope such that a real-time imaging of deformation mechanisms is possible.^{2,4} Although a vast amount of research on the mechanical characterization of 1D nanostructures has been reported based on these techniques, there are limitations associated with these tests.

It is well-understood that manipulating and positioning nano-sized specimens is the largest challenge in nanomechanical testing.³⁻⁵ The experimental hurdles become greater when the specimens must be freestanding, aligned with the loading direction and firmly clamped at both ends.^{2,4} Extra effort has to be taken to prevent misalignment between specimen axis and loading direction as this may lead to unwanted bending moment and consequently premature sample failure.⁴ On the other hand, common approaches for specimen gripping include local deposition of hydrocarbon or local injection of precursor gas to form fixation using focused e-beam (EBID). This fixation method has been employed extensively and proven to be sufficiently strong; however, recent studies showed that the EBID-based clamps could introduce significant error in the measured mechanical properties.^{2,6-8}

In response to the experimental issues and challenges pertaining to the AFM/nanoindentation- and electron microscopy-based testing of 1D nanostructures, the buckling-based technique appears to be a promising alternative. About a decade ago, a group of researchers at the Polymers Division of National Institute of Standards and Technology (NIST) was the first to demonstrate buckling of polymeric thin films on a compliant substrate as a means of metrology in identifying the mechanical moduli of the film materials.^{9,10} The technique is coined “strain-induced elastic buckling instability for mechanical measurements”, or SIEBIMM which aims to rapidly measure the elastic modulus of coatings and films. The success of this buckling-based metrology has stimulated substantial interest in applying similar measurement methodology to the soft elastic substrate¹¹ and other nanostructures such as nanowires^{12,13}, nanotubes¹³⁻¹⁵, and nanoribbons¹⁶ as an easy, quick, inexpensive and efficient way to yield their elastic moduli. Additionally, the application of buckled nanostructures on elastomeric substrate has also led to the realization of stretchable electronics^{12,14-18}, micro- and

nanoelectromechanical systems (MEMS and NEMS), tunable diffraction and phase grating^{19,20}, and microfluidic devices²¹.

1.1 Buckling

Buckling (wrinkling) is an inevitable phenomenon in our daily life, for instances, wrinkling of human skin due to aging, paint wrinkling, surface of dried fruits, to name a few. From the viewpoint of engineering, buckling is described as a form of mechanical instability experienced by the materials to release internal strain when an external compressive force is applied. Under certain circumstances, buckling is highly undesired and often perceived as a mode of catastrophic structural failure. For example, the rail accidents which are taking toll in the U.S. transportation could be a fatal consequence of track buckling in extreme heat and cold under the changing climate.²² Conversely, some forms of buckling are elastic in nature such that they can disappear or reappear by the application of an external force.²³ Researchers have recently exploited such elastic instabilities to advantage in diverse fields, including micro/nanofabrication, optics, bioengineering, and metrology as well as fundamental mechanics studies.^{18,23}

A great interest on buckling aroused within the scientific community when Whitesides and coworkers¹⁹ first reported on the spontaneous generation of complex, ordered structures induced by the buckling of thin metal films owing to thermal contraction of an underlying substrate. In their pioneering work, a thermally expanded elastomeric substrate of polydimethylsiloxane (PDMS) was coated with a thin layer of metallic film (such as Au, Ni, or Al with 5 nm adhesion interlayer of Ti or Cr) by electron beam evaporation. The heat introduced before and during the deposition process caused the polymer to expand, and the subsequent cooling of the polymer to

room temperature induced shrinkage, rendering a compressive stress on the metallic film. The presence of equi-biaxial compressive stress state on the metallic film was due to the large thermal expansion mismatch between the polymer and the metal. To relieve the stress, the metallic film buckled in a sinusoidal form with a wavelength ranged between 20 – 50 μm . Figure 1.1 illustrates the process. Disordered wavy structures were created on a flat, unconfined PDMS substrate surface while uniformly oriented buckling patterns can be developed by employing PDMS substrate having a bas-relief pattern on its surface.^{19,24} The film thickness and intrinsic mechanical properties of the materials involved in the system are the parameters governing the buckling wavelength.

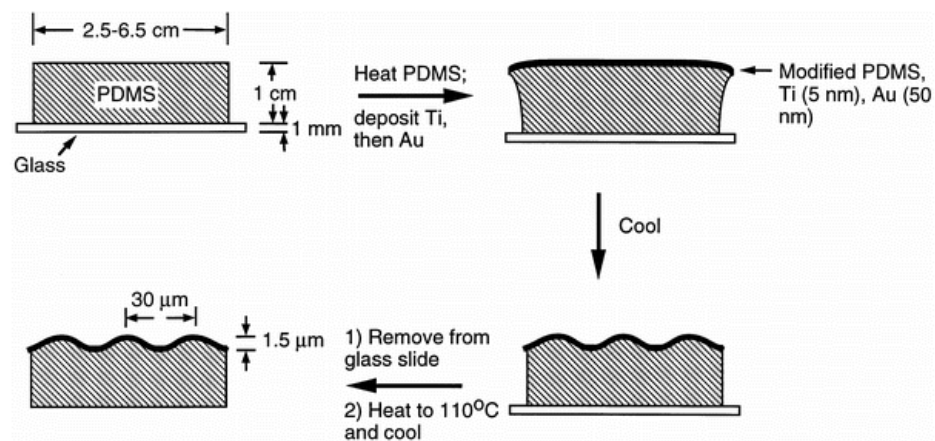


Figure 1.1: Schematic diagram of thermally-driven buckling of a bilayer system of Au-coated polydimethylsiloxane (PDMS) substrate.¹⁹

In theory, the buckling instability is a result of the balance between the energy required to bend the stiff upper film and the energy required to deform the soft underlying substrate.⁹ Following the pioneering work of Whitesides, Chen and Hutchinson theoretically demonstrated that the herringbone pattern (left region of Figure 1.2) formed under these conditions constitutes a minimum energy configuration of the system.²⁵ The elastic energy of the film/substrate system consists of three

components, *i.e.* the uniform resultant in-plane stresses in the film, bending contribution from the film and elastic energy in the substrate. The study has apparently laid a fundamental understanding of the buckling mechanics based on the principle of minimum energy. Since then, a significant amount of work has been carried out to embrace this form mechanical instability in various applications such as organic light emitting diodes (OLEDs), surface-enhanced Raman scattering, optical diffraction gratings^{19,20} and thin-film metrology⁹⁻¹¹.

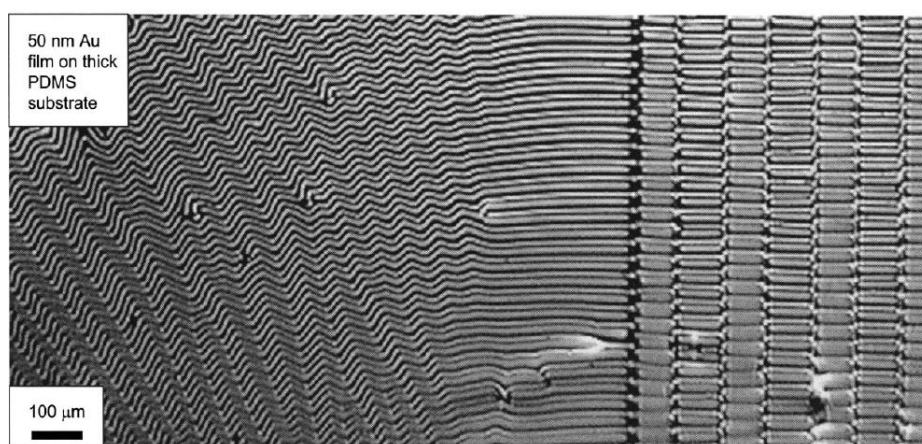


Figure 1.2: Buckling of a 50 nm gold film on a thick elastomer (PDMS) substrate. The unpatterned left region of the substrate displayed the herringbone pattern while the right region which has been patterned with alternating flat depressions exhibited ordered wavy pattern.²⁵

In addition to thermal-induced buckling, swelling (with solvent or monomer solution) offers an alternative to generate surface buckling patterns in a bilayer thin film^{20,23} by controlling the solvent diffusion kinetics and quality, engineering the film crosslinking density and using microfluidic channels²⁰. As featured in Figure 1.3, the application of solvent on the top surface of the elastoplastic film causes it to swell and experience significant volumetric change, whereas the bottom surface of the film remains unaffected as it is confined to the rigid substrate underneath it. As a result, this

generates an anisotropic osmosis pressure along the film thickness, which further leads to a biaxial compressive stress on the film surface when the osmosis pressure becomes greater than a critical value, resulting in surface buckling.

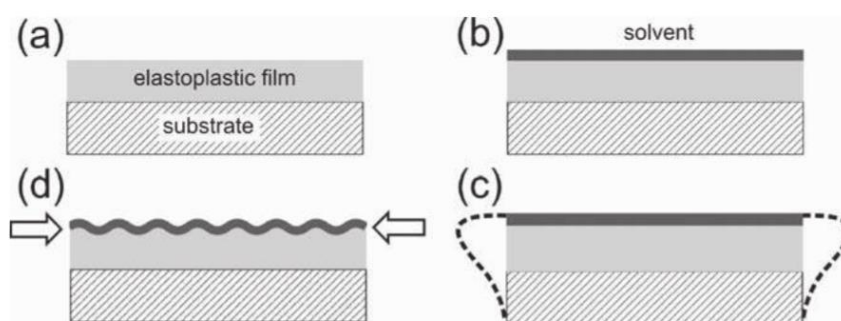


Figure 1.3: Schematic diagram of swelling-driven buckling process.²³

Swelling can occur in either liquid or vapor phase, and the resulting wrinkle patterns which are transient and reversible in nature, is controlled by the kinetics of the diffusion process.²⁰ One successful application of this osmosis-driven buckling mechanism is demonstrated by Kim and Crosby²¹ in fabricating a solvent-responsive microfluidic system, as depicted in Figure 1.4. Wrinkles were generated within the selectively oxidized area between two microfluidic channels when ethanol was introduced into one microchannel, and the smooth surface was later recovered upon removal of the ethanol. The potential of swelling-induced buckling mechanism has been exploited over the years to fabricate functional devices such as responsive microfluidic channels²¹, tunable microlens arrays²⁶ and facile printing of nanoparticle assemblies.

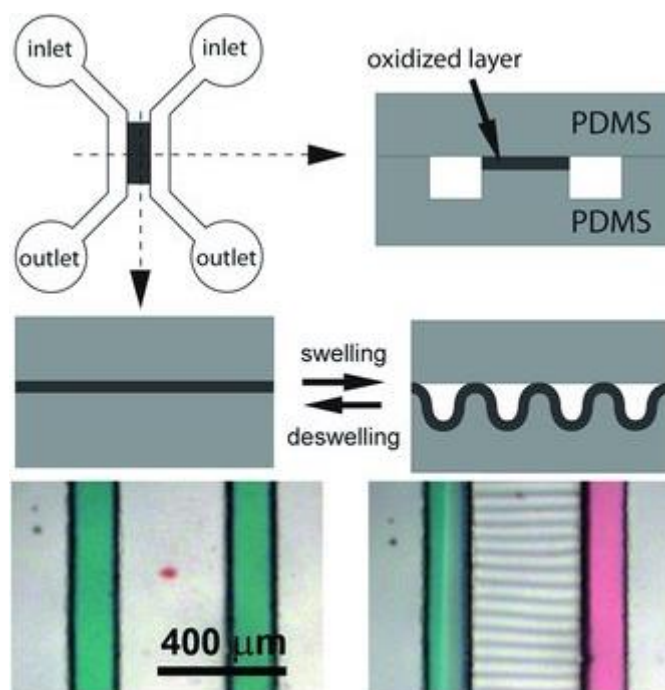


Figure 1.4: Schematic representations of reversible wrinkle channels in a microfluidic system. The wrinkle channels are opened and closed reversibly in response to the introduction of ethanol. Green food dye and red one were used to distinguish water and ethanol, respectively.²¹

As we have discussed above, the compressive strain in the top layer of the bilayer buckling system can be imposed either by shrinking (expanding) its present state beyond its equilibrium stress-free state through temperature control or application of a solvent. These two classes of buckling methods require physical confinement to induce and regulate the buckling profile. On the contrary, the use of mechanical force to render surface buckling allows one to independently control the amount, direction and duration of strain applied to the films in order to maneuver the pattern formation, transition and orientation in real time.^{20,23,27} The precise control of strain applied can be achieved with the use of a stretching device. Lin and Yang²⁷ successfully tailored highly ordered zigzag herringbone structure (as shown in Figure 1.5) with the means of mechanical buckling, using the strategy of sequential release of applied stress to provide a well-controlled energy release path. This mechanical approach provides added

controllability on the buckling patterns which would be beneficial for a broad spectrum of applications.

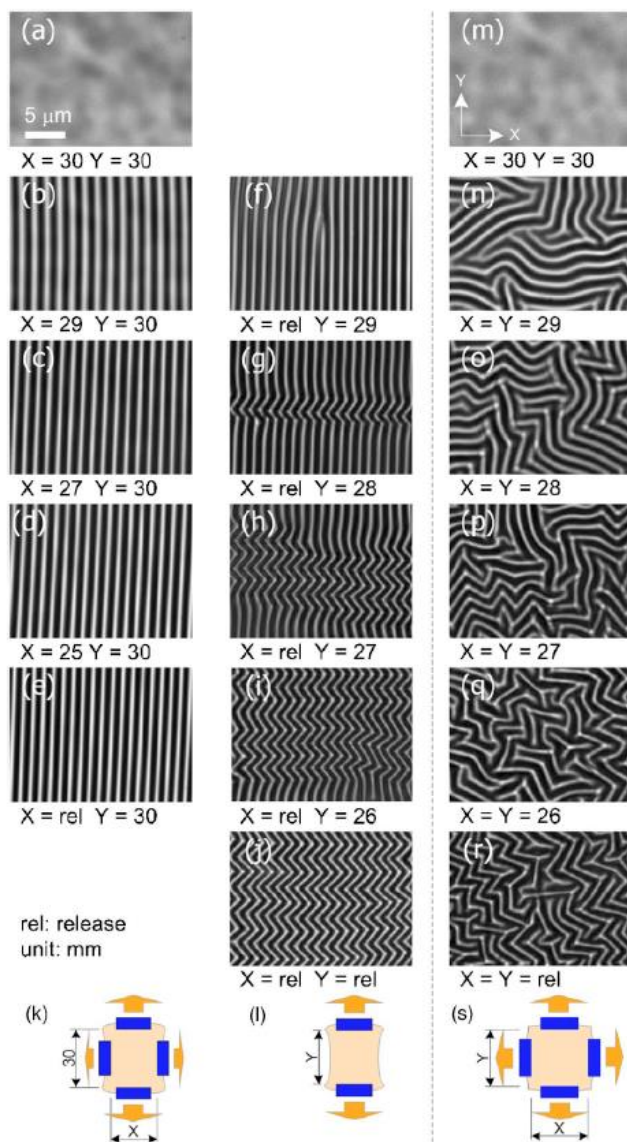


Figure 1.5: Two sets of sequential optical microscope images of two equally stretched PDMS samples (20% strain, from 25 to 30 mm on both edges) subjected to two different releasing processes, (a–j) sequentially and (m–r) simultaneously, respectively, and their corresponding illustrative sketches (k–l) and (s), accordingly. Scale bar in (a) is applicable to all images.²⁷

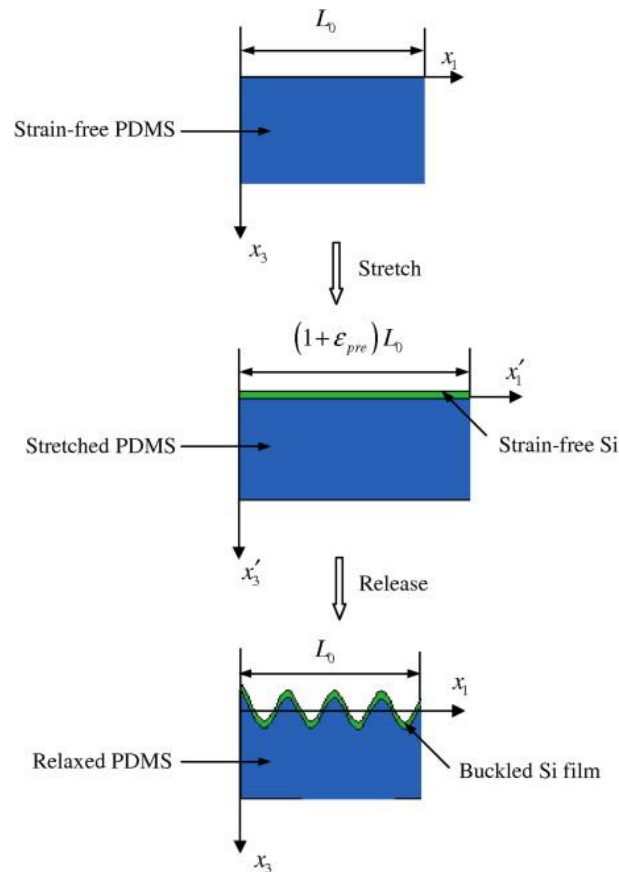


Figure 1.6: Three sequential configurations for the thin film/substrate buckling process under mechanical force. The top figure shows the undeformed substrate with the original length L_0 . The middle figure shows the substrate deformed by the pre-strain ϵ_{pre} and the integrated film. The bottom figure shows the deformed (buckled) configuration.²⁸

Figure 1.6 schematically elucidates the strategy applied in the mechanical buckling, which consists of three steps: i) applying pre-strain ϵ_{pre} to the compliant substrate, ii) depositing or transferring thin film materials (or any other thin, stiff materials) onto the surface of the pre-strained compliant substrate, and iii) releasing the pre-strain of the compliant substrate so as to allow it to return to its original dimensions. The release of the pre-strain on the compliant substrate induces a compressive stress on the strain-free film which later buckles spontaneously into sinusoidal shape in order to relieve the compressive stress. In general, a stiff film favors long wavelength when buckled because it costs lesser energy than buckling into a rather short wavelength.

Conversely, the soft substrate tends to buckle into shorter wavelength due to its lower energy cost. When integrated into a bilayer system, the buckling yields a value somewhere between these large and small wavelengths.¹⁸

1.2 Mechanical buckling as metrology

In 2004, Stafford and coworkers⁹⁻¹¹ demonstrated that mechanical buckling can be exploited as a form of metrology for measuring the elastic moduli of polymeric thin films. Under this metrology technique, the characteristic length scale of the buckling pattern (viz. the buckling wavelength and amplitude) is used to characterize the material properties; thus, a thorough understanding of the self-organization process is important in translating the geometric measurements of the buckling profile into material property values.²⁹ In fact, the underlying mechanics governing the buckling of a stiff film attached to a compliant substrate have been elaborated by several researchers using either a force balance³⁰ or an energy balance²⁵ approach.

In their pioneering work, Stafford and coworkers prepared a bilayer sample comprised of a thin film of polystyrene (PS) with gradient thickness, ranging from 140 to 280 nm, on top of a PDMS substrate. Subjecting the bilayer sample to uniaxial compressive force induced surface buckling with a wavelength linearly proportional to the film thickness, as shown in Figure 1.7. Using the governing equation of the associated buckling instability derived by other researchers³⁰, they observed that the computed Young's modulus of the PS film is constant over the range of film thicknesses and in excellent agreement with the measured bulk modulus of PS. In the same article, it is pointed out that similar measurement methodology was also performed on PS films with varying amount of plasticizer and organosilicate films with different porosity level. The modulus values thus determined agreed well with the values obtained by

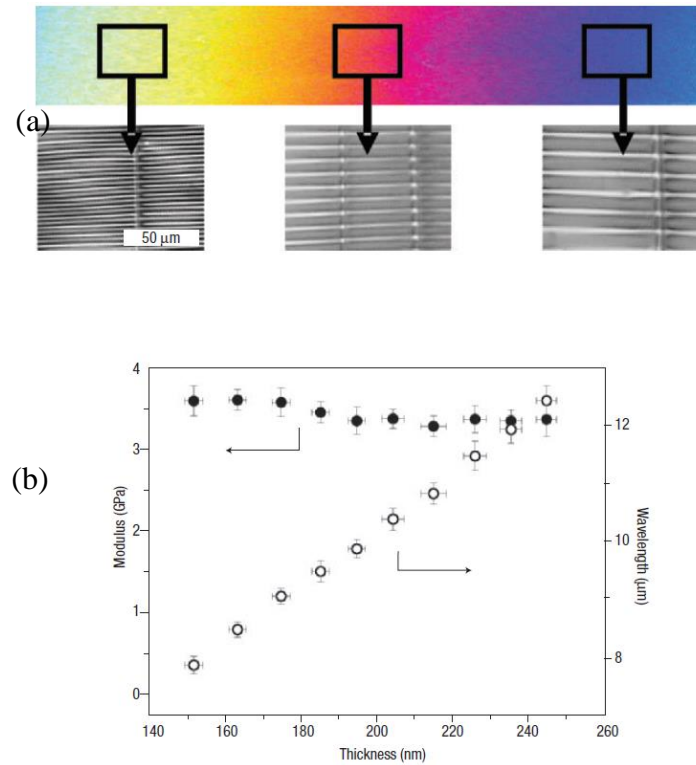


Figure 1.7: (a) Optical microscopy image of a PS gradient film showing the increase in buckling wavelength with film thickness. (b) Measured buckling wavelength (open circles) and calculated Young's modulus (closed circles) for the PS gradient film as a function of film thickness. The Young's modulus computed from Eq. 1.1 remains constant with thickness over this range, varying little from its average value of 3.4 GPa \pm 0.1 GPa.⁹

nanoindentation, confirming the accuracy and reliability of this form of metrology technique. Following the applicability of this metrology, Stafford and coworkers suggested that the governing equation can be rearranged as follows to yield the modulus of the film material.

$$E_f = \frac{3E_s(1 - \nu_f^2)}{(1 - \nu_s^2)} \left(\frac{\lambda}{2\pi h} \right)^3. \quad (1.1)$$

Here, the film thickness (h), buckling wavelength (λ), substrate modulus (E_s), substrate Poisson's ratio (ν_s) and film Poisson's ratio (ν_f) represent the important parameters to enable the film modulus characterization. The solution assumes elastic deformation of the materials and only valid in the limit of: (a) low strain ($\ll 10\%$), (b) $E_f/E_s \gg 1$, (c)

substrate being much thicker than the film, and (d) amplitude of the buckles is much smaller than their wavelength.⁹ The subscripts f and s denote film and substrate, respectively.

To extend the applicability of the buckling-based metrology as well as demonstrate its versatility, Stafford and coworkers later “reversed” this metrology to measure the moduli of the soft substrate¹¹. In the study, a sensor film of known modulus and thickness was mounted on top of a soft gradient substrate (PDMS and poly(HEMA) hydrogel gradient sample with varying cross-linker composition) and similar metrology was conducted to evaluate the substrate moduli. The near-equivalence between the substrate moduli as calculated from the buckling metrology and tensile test further verified that the buckling-based metrology can be successfully implemented to a broad range of film materials, as long as there exists a modulus mismatch between the film and the substrate. These few experiments illustrate that the buckling-based metrology is a very useful tool for rapid, high-throughput and spatial screening of the mechanical properties of both soft and film materials^{9-11,16,31-34}.

1.3 Mechanical buckling of 1D nanostructures

Interestingly, in addition to probing the mechanical properties of soft and thin film type materials, the buckling-based metrology has been implemented with equal success to one-dimensional (1D) structures like micro/nanowires^{12,13,35} and nanotubes¹³⁻¹⁵ which possess relatively high stiffness. The first demonstration of such application was succeeded by Rogers and coworkers^{14,15} with the use of single-wall carbon nanotubes (SWNTs) having diameter between ~ 1 and ~ 4 nm. Their work revealed that this metrology can be applied to materials with molecular scale (*i.e.* ~ 1

nm) dimensions and the underlying physics can be accurately described using the Newtonian mechanics models.

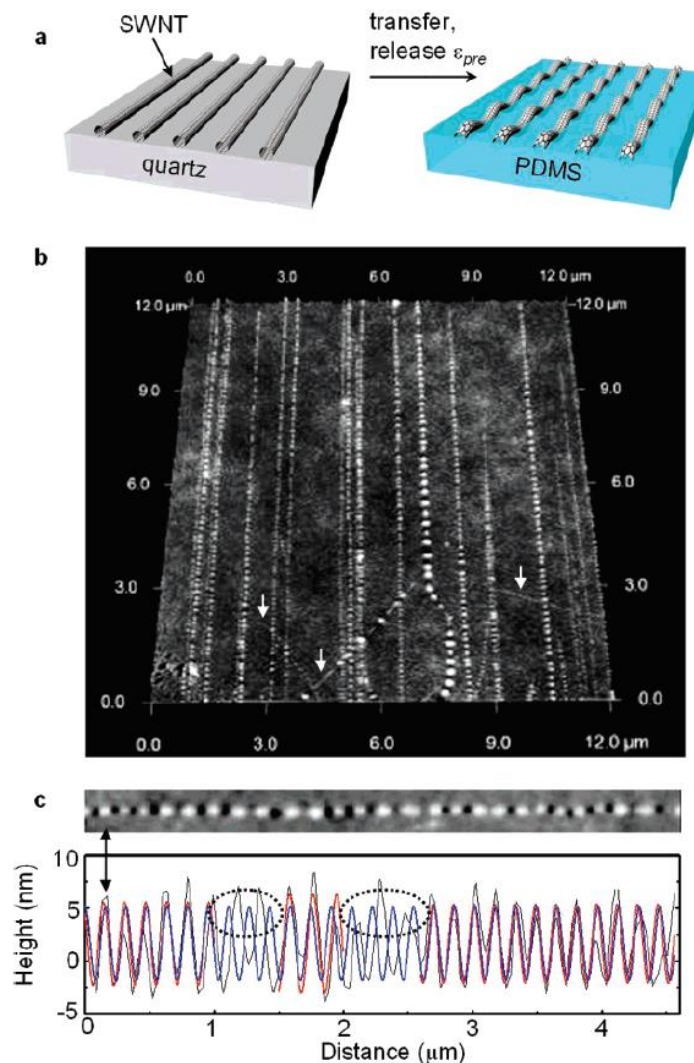


Figure 1.8: (a) Transfer of aligned arrays of SWNTs grown on quartz to a uniaxially strained substrate of PDMS followed by release of the pre-strain (ϵ_{pre}) causes nonlinear buckling instabilities in the SWNT that lead to wavy configurations. (b) Large-area (12 $\mu\text{m} \times 12 \mu\text{m}$) angled-view atomic force microscope (AFM) image of wavy SWNTs on a PDMS substrate. (c) Plane-view AFM image of an individual wavy SWNT and line-cut showing the profile of relief. The red, black, and blue curves represent measured data, a piecewise sinusoidal fit, and a global sinusoidal fit, respectively. The dashed ovals indicate regions that represent abrupt shifts in the phase. The wavelength determined by the piecewise fit is $160 \pm 20 \text{ nm}$.¹⁴

In their innovative work, an array of well-aligned long SWNTs were transferred from the growth substrate (quartz) to a mechanically pre-strained (approximately 3 – 5%) PDMS substrate with the length axis of the SWNTs parallel to the uniaxial tensile direction, as shown in Figure 1.8 (a). Releasing the pre-strain in the PDMS substrate yielded buckling in the SWNTs with wavelengths ranging from 100 to 300 nm and amplitudes of several nanometers. Diameter dependence of wavelength observed in the experiment was attributed to the effect of coupling of individual SWNTs into bundles during the transfer process. Using the buckling mechanics developed from the linear elasticity theory¹⁵, the Young's modulus of an individual SWNT was calculated as 1.3 ± 0.2 TPa, which was found to be consistent with the results obtained from atomic force measurements and first-principles calculations.

Based on the analytical solution, Rogers and coworkers predicted that the expressions for the wavevector k and amplitude A take the following forms through the minimization of the total system energy.

$$k \left(\frac{E_{CNT}I}{\bar{E}_s} \right) = \left[\frac{2\pi(1 - \gamma - \ln kR)}{(3 - 2\gamma - 2 \ln kR)^2} \right]^{1/4} \quad (1.2)$$

$$A = \frac{2}{k} \left[\varepsilon_{pre} - \frac{E_{CNT}I}{E_{CNT}S} k^2 - \frac{\bar{E}_s \pi}{E_{CNT}S k^2 (3 - 2\gamma - 2 \ln kR)} \right]^{1/2} . \quad (1.3)$$

Here, $\gamma = 0.577$ is Euler's constant, R is the radius of the SWNT, and $E_{CNT}I$ and $E_{CNT}S$ are the bending stiffness and tension stiffness of the SWNT, respectively. Eq. (1.2) can be approximated (to an error within ~5%) to the following solution when $R > 0.5$ nm and $E_{CNT}/\bar{E}_s > 25000$

$$k = \frac{3}{4} \left(\frac{\bar{E}_s}{E_{CNT}I} \right)^{1/4} . \quad (1.4)$$

Knowing the wavelength is related to the wavevector by $\lambda = 2\pi/k$, it is proposed that the Young's modulus of SWNT can be calculated using the following expression as follows

$$E_{CNT} = 2.03 \times 10^{-4} \frac{\lambda^4 \bar{E}_s}{I}. \quad (1.5)$$

The wavelength information is used in evaluating the modulus of the nanostructure because it is less dependent on the pre-strain amount and relatively insensitive to the residual surface roughness of the PDMS than the amplitude.

They attributed the success of the Newtonian mechanics model in describing the experimental observations to three important factors:

- (i) Substrate modulus - Based on the Eq. (1.5), the value of the calculated Young's modulus of a SWNT is linearly sensitive to the modulus of the PDMS. More precisely, an increase or decrease of 10% in the substrate will result in the similar effect on the computed Young's modulus of the nanostructure. Hence, it is important to ensure the accuracy of the substrate modulus value used in the measurement.
- (ii) Condition and alignment of the tubes - It is highlighted that the relatively long dimensions, high levels of structural perfection of the tubes and the small deformation involved in the experiments is critical in explaining the success of the model. In addition, deviation from the model may occur when the tubes are misaligned with the pre-strain direction and therefore not forming wavy structure.
- (iii) Amount of pre-strain applied - The theory suggests that the mechanical forces, as a result of applied pre-strain, ought not to exceed van der Waals attractions at the SWNT/PDMS interface, in such way that most SWNT buckle rather than delaminate or slip during the release of the pre-strain.

Their work showed that the buckling-based metrology technique is a complement to existing testing protocol which helps to address cutting-edge challenges

in nanoscale characterization. Its ease of implementation and no need for any complex or expensive instruments has rendered it an invaluable addition to the conventional nanomechanical testing. In fact, the advantage of this metrology lies in the ability to use straightforward theory of Newtonian mechanic model to relate the modulus of the 1D nanostructure to otherwise easy-to-measure parameters (*i.e.* buckling amplitude and wavelength).

With the interest in this newly developed metrology technique, several researchers have exploited it to characterize other materials of similar dimensions. Table 1.1 lists the available literatures, though not an exhaustive one, on the application of buckling-based metrology technique in determining the Young's modulus of 1D nanostructures.

1.4 Core-sheath structure

A close review of the literatures discloses that only a limited number of material systems have been investigated using the buckling-based metrology technique and the results were reported based on a single material structure. However, most studies acknowledged the existence of an amorphous oxide layer surrounding the nanostructures, resulting in a core-sheath-like structure. Amorphous oxide layer usually forms as a result of reaction with residual oxygen in the apparatus³⁶ during the synthesis or post-fabrication process. Transmission electron microscopy (TEM) imaging shows that thickness of the amorphous oxide sheath typically ranges within 1 to 14 nm.³⁷⁻⁴² It is important to note that the elastic behavior of the amorphous oxide sheath differs considerably from that of its core material. For instances, Liu *et al.* reported an amorphous boron oxide (B_2O_3) layer with a thickness of 1-2 nm exists on the single crystalline boron nanowire, with the bulk B_2O_3 modulus of nearly 10 times lower than

Table 1.1: Existing literature on the buckling mechanics of 1D micro/nanostructures on a compliant substrate (N – not reported).

Reference			Nanostructure					Substrate			Buckling test		
Authors	Year	Journal	Material	Type	Cross-section	Length (um)	Dimension	Material	Stiffness (MPa)	Surface treatment	Pre-strain method	Pre-strain amount	Buckling mode
Khang <i>et al.</i>	2008	Nano Letters, 8 (1), 124-130	SWCNT	Nanotube	Circular	Long	Dia 1, 4 nm	PDMS	1.95	N	Mech.	3-5 %	Out-of-plane
Ryu <i>et al.</i>	2009	Nano Letters, 9 (9), 3214-3219	Si	Nanowire	Hexagonal	>> 40	R 20-85 nm	PDMS	2	N	Mech.	27 %	In-plane
Xue <i>et al.</i>	2011	ACS Nano, 5 (4), 3326-3332	PZT	Nanoribbon	Rectangular	1000	H 400 nm, B 80 um	PDMS	2	N	Therm.	5 %	Out-of-plane
Qi <i>et al.</i>	2011	Nano Letters, 11, 1331-1336	PZT	Nanoribbon	Rectangular	Long	H 250-500 nm, B 5-10 um	PDMS	N	N	Mech.	1-10 %	Out-of-plane
Xu <i>et al.</i>	2011	ACS Nano, 5 (1), 672-678	Si	Nanowire	Hexagonal	>> 30	R 12-18 nm	PDMS	Variable	UVO	Mech.	20%	In-/out-of-plane
Zhu <i>et al.</i>	2012	Adv. Mater., 24, 1073-1077	MWCNT	Nanotube	Circular	Long	R 15-25 nm	PDMS	2	N	Mech.	No	In-plane
Xu <i>et al.</i>	2012	Adv. Funct. Mater., 22, 1279-1283	MWCNT	Nanotube	Circular	Long	R 15-25 nm	PDMS	2	N	Mech.	100 %	Out-of-plane
Duan <i>et al.</i>	2014	Nanoscale, 6, 3289-3295	PVDF	Microribbon	Rectangular	Long	H 1 um, B 2-3 um	PDMS	0.5	N	Mech.	20-80 %	In-/out-of-plane
				Microwire	Circular	Long	R 1 um	PDMS	0.5	N	Mech.	20-80 %	In-plane

that of the bulk boron.³⁹ The presence of 1-2 nm thick native oxide layer on the boron nanowire with diameter of ~40 nm resulted in 6.8 and 7.5% error in the measurement of elastic modulus and fracture strength of the boron nanowires, respectively.

Ultimately, one must not ignore the effect of amorphous oxide layer on the measurement of the true elastic properties of the nanostructures.

In order to consider the effect of core-sheath structure on the elastic properties of the nanostructures, several researchers have modified the relevant equations to yield the effective elastic properties by taking into account of the proportion of the cross-sectional area composed of the core and sheath components. Based on the classical mechanics theory of compound materials, Wang proposed that the bending modulus of a circular nanowire having core-sheath structure takes the following form⁴²

$$E_{eff} = \alpha E_{core} + (1 - \alpha) E_{sheath} \quad (1.6)$$

where

$$\alpha = \left(\frac{D_{core}}{D_{sheath}} \right)^4. \quad (1.7)$$

Meanwhile, the tensile modulus of a circular nanowire with core-sheath structure was recommended by Liu *et al.* as follows³⁹

$$E_{eff} = \beta E_{core} + (1 - \beta) E_{sheath} \quad (1.8)$$

where

$$\beta = \left(\frac{D_{core}}{D_{sheath}} \right)^2. \quad (1.9)$$

Recognizing the influence of core-sheath structure on the moduli measurement is important in deriving the total potential energy of the buckling system, which would subsequently impact the buckling mode of the nanostructures. While the above equations are only valid for nanostructures having a circular cross-section, effort needs

to be made to develop ones which would account for a rectangular cross-section structure, so that the equations are applicable to our silicon nanoribbons.

1.5 Buckling mode

While revisiting the literature review, two different buckling modes of 1D nanostructures on elastomeric substrate are observed, *i.e.* out-of-plane and in-plane buckling. In the pioneering work, Rogers and coworkers reported out-of-plane buckling of the SWNTs on the PDMS substrate after an array of long, well-aligned SWNTs was transferred to a pre-strained PDMS substrate surface and followed by the release of the pre-strain. Conversely, the succeeding work utilizing silicon nanowires (SiNWs) exhibited predominantly an in-plane buckling mode instead. This phenomenon has attracted several researchers to investigate the competition between out-of-plane and in-plane buckling through an energy method.

1.5.1 Least energy principle

Regardless of the buckling mode, the total potential energy of the buckled 1D nanostructures (also termed as a stiff beam due to its large length-to-height ratio) on a compliant substrate consists of three components, namely the bending energy of the stiff beam due to buckling U_b , the membrane energy of the stiff beam U_m and the strain energy of the compliant substrate U_s due to the compressive stress induced by the release of applied pre-strain. The mechanics of the buckling system is detailed in Chapter 3. Based on the least energy principle, the buckling mode having the lower total system energy is energetically favorable and thus exists.^{12,13,25,43}

In the work of mechanical buckling of SiNWs, Ryu *et al.* compared the total system energy for both out-of-plane and in-plane buckling mode. It is noted that in-plane buckling constitutes slightly lower energy (Figure 1.9 (a)) and is therefore energetically favorable than out-of-plane buckling. Figure 1.9 (b) also indicates that the energy difference for one-dimensional SiNWs is greater than the adhesion energy between SiNWs and PDMS (50.6 mJ/m^2), particularly at larger wire radius. This justly explains the observation of in-plane buckling of SiNWs. Question arose as to why would SWNTs buckled out-of-plane; this is explained in the following section.

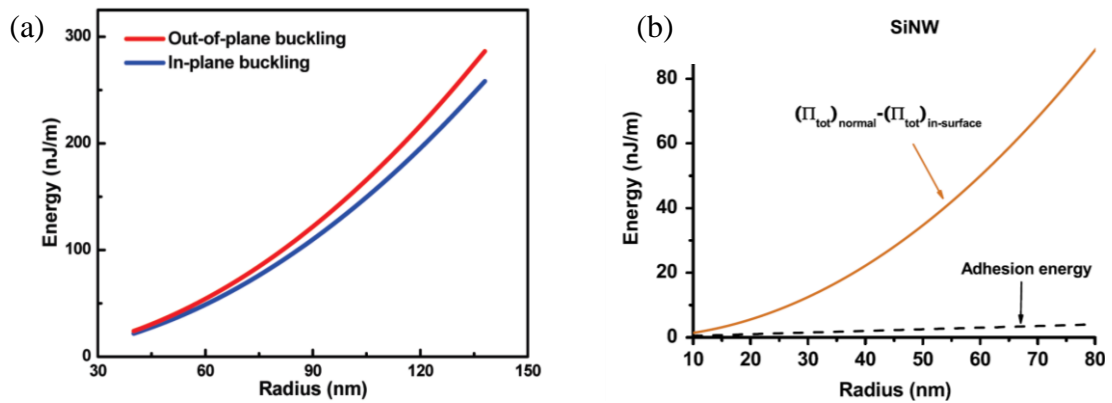


Figure 1.9: (a) Energy difference between normal and in-surface buckling¹², and (b) comparison between the energy difference and adhesion energy between SiNWs and PDMS¹³, as a function of SiNW radius.

1.5.2 Effect of geometrical parameters

The buckling mode competition behavior has also intrigued Duan *et al.* to scrutinize other possible parameters that govern the competition between the two buckling modes of the 1D-nanostructure-on-substrate system. Noting that silicon nanoribbons (SiNRs) and nanowires (SiNWs) bonded on pre-strained substrate buckled out-of-plane and in-plane, respectively, Duan *et al.* speculated that geometrical parameters could be the reason for the buckling mode competition. To answer this

speculation, a combinatory approach of experimental-analytical-simulation was conducted using a single type of material with different cross-sections. In their work, polyvinylidene fluoride (PVDF) microwires and microribbons were directly deposited on pre-strained PDMS substrate through electrospinning (Figure 1.10 (a)). Similar to prior studies, the PVDF microwires buckled in-plane while the microribbons exhibited out-of-plane buckling, as depicted in Figure 1.10 (d-e).

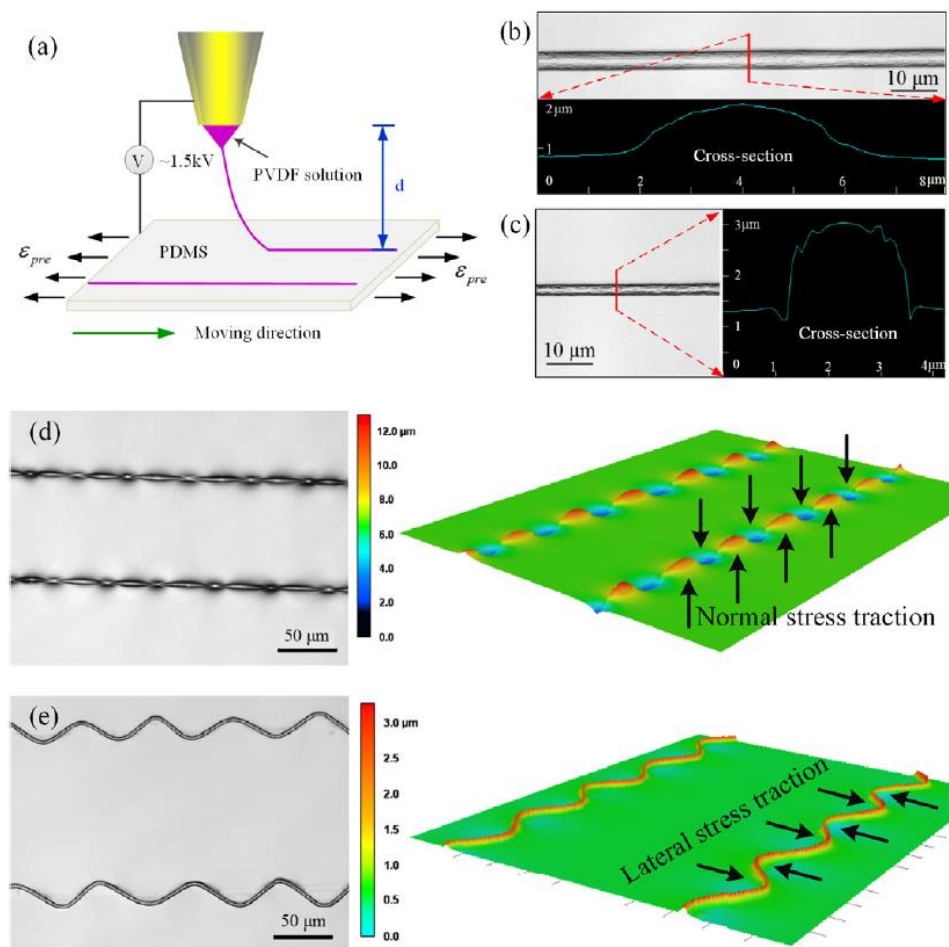


Figure 1.10: (a) Schematic diagram of the electrospinning process for micro/nanofiber fabrication. (b), (c) Straight fibers deposited on the pre-strained PDMS substrate and their cross-sections when the nozzle-to-substrate distance (d in (a)) is 2 mm (b) and 8 mm (c). (d), (e) Straight fibers in (b) and (c) buckle out-of-plane (d) and in-plane (e) respectively when releasing the pre-strain of the PDMS substrate. The right columns of (d) and (e) are the 3D views of the left 2D graphs.³⁵

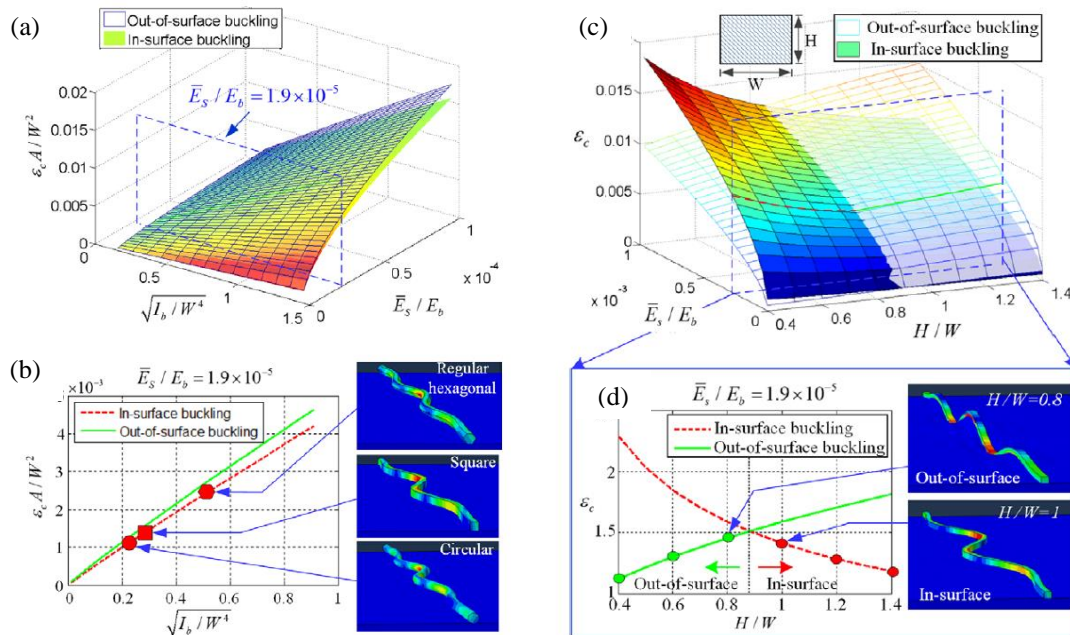


Figure 1.11: (a) The critical buckling strains for both in-plane and out-of-plane buckling when $I_{b1} = I_{b2}$. (b) The critical buckling strains when $I_{b1} = I_{b2}$ and $E_s / E_b = 1.9 \times 10^{-5}$. The right columns of (b) are FEA results of stiff layers with square, circular and regular hexagon cross sections buckle in-plane on elastomer. (c) The critical out-of-/in-plane buckling strains of rectangular cross-section. (d) The critical out-of-/in-plane buckling strains of rectangular cross-section when $\bar{E}_s / E_b = 1.9 \times 10^{-5}$. The right columns of (b) are FEA results when $H / W = 0.87$ and $H / W = 1$, out-of-plane buckling and in-plane buckling occurs, respectively.³⁵

Theoretical analysis using the least energy principle validates that the buckling mode is determined by cross-sections of the microstructures.³⁵ As illustrated in Figure 1.11 (a), for cross-sections having equal second moment of inertia in both out-of-plane and in-plane directions, e.g. circular, square and regular hexagonal, in-plane buckling is always favorable; this is in good agreement with prior studies on the mechanical buckling of SiNWs^{12,13} and CNTs¹³. For cross-sections having unequal second moment of inertia in out-of-/in-plane directions, e.g. rectangular and elliptical, there exists a critical value of aspect ratio (defines as the ratio of height to width, H / W in their work³⁵), below (above) which out-of-plane (in-plane) buckling is favorable for having smaller critical buckling strain. Figure 1.11 (b) shows that the critical aspect ratio for a rectangular cross-section occurs at 0.88 when $\bar{E}_s / E_b = 1.9 \times 10^{-5}$.

While the existing studies suggested that in-plane buckling mode is energetically favorable for cross-sections having equal second moment of inertia in out-of-/in-plane directions such as a circular one, Rogers and co-workers rectified that the out-of-plane buckling of SWNT in their pioneering work is an exception due to the extremely small radius of the SWNTs (~1 nm). Rather than in-plane buckling, the SWNTs buckled out-of-plane owing to the lateral constraints provided by the surface roughness of the PDMS which is comparable to or even larger than the SWNT radius. It is speculated that the surface roughness of the PDMS have prevented in-plane buckling of the SWNTs. Otherwise, the out-of-plane buckling of SWNTs would have been energetically unfavorable.^{12,13} On the other hand, a question is raised as to how would SiNRs having core-sheath structure behave under mechanical buckling and when would the buckling mode transition occur.

1.5.3 Effect of interfacial adhesion

Another interesting buckling phenomenon was reported by Zhu and coworkers, highlighting that the buckling mode of the SiNWs can differ from in-plane mode to three-dimensional helical coil form, depending on the adhesion strength between the SiNWs and the PDMS substrate.⁴⁴ The interfacial adhesion strength can be modulated by manipulating the surface chemistry of the nanostructures and PDMS substrate.

PDMS represents unique polymeric materials comprising an inorganic siloxane ($-\text{Si}-\text{O}-\text{Si}-$) backbone with two methyl ($-\text{CH}_3$) functional groups attached to each silicon (Si) atom. Figure 1.12 (top left) shows the molecular configuration of PDMS. The presence of two stable methyl groups on each repeating unit renders PDMS hydrophobicity, high chemical inertness and low surface energy. These properties of PDMS combined with its low Young's modulus enables the formation of conformal

contact between a flat piece of PDMS with almost any material of relative smoothness, through the action of weak van der Waals force.⁴⁵ To obtain favorable bonding interactions, it is demanded that PDMS surface becomes hydrophilic or functionalized with various chemical moieties.

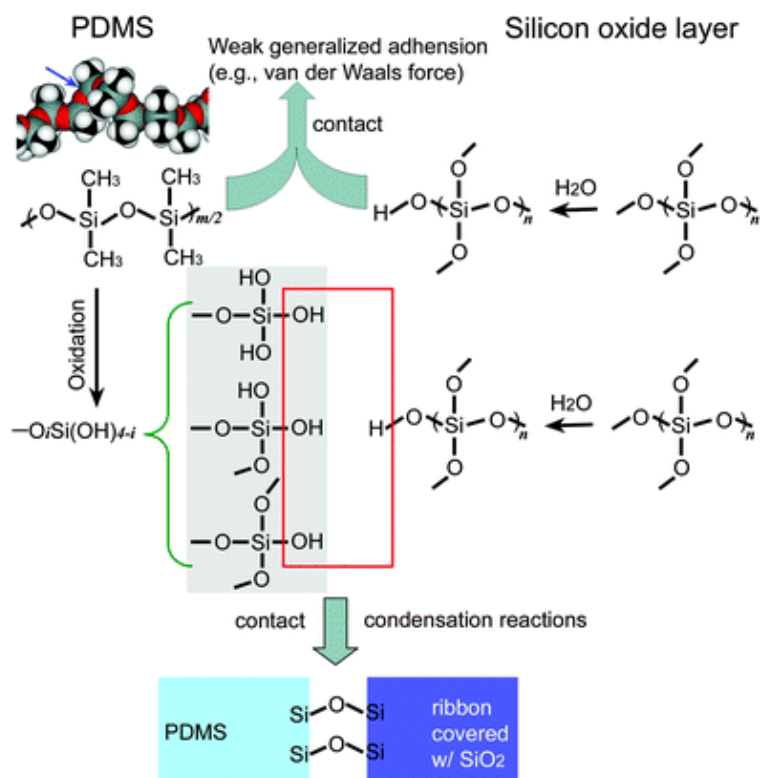


Figure 1.12: Illustration of the surface chemistry of PDMS and reactions occurring at the interfaces between PDMS and semiconductor nanoribbons covered with thin SiO₂ layers.⁴⁵

Over the years, numerous physical⁴⁶⁻⁵¹ and chemical⁴⁸ routes have been developed to tailor the surface properties of PDMS. Surface modification by chemical means involves the use of strong base or acid which usually leads to an uncontrollable and non-uniform outcome. Alternatively, physical surface modification techniques, such as plasma, corona and ultra-violet/ozone (UVO) treatment, has proven to provide well-controlled chemical modification and in-plane uniformity of the surface.⁵⁰ These

physical approaches aim to introduce hydroxyl functional group on the PDMS surface needed for subsequent reactions, by means of oxidation. Among all, UVO treatment represents the most explored approach to oxidize PDMS due to its milder modification effect, high efficiency in generating highly active oxygen species⁴⁶, as well as ease of operation and control.

UVO treatment is a photosensitized oxidation process in which the molecules of treated material are excited and/or dissociated by the absorption of short-wavelength UV radiation; and later reacts with atomic oxygen to form simpler, volatile molecules which desorb from the surface.⁴⁶ When the UVO treatment is carried out on the PDMS surface, the atomic oxygen attacks the Si atom on the PDMS surface chains to remove the methyl groups, resulting in the formation of polar silanol ($-\text{Si}-\text{OH}$) groups, as indicated in Figure 1.12 (middle left). The chemical alteration has been reported in previous surface analysis studies using attenuated total reflective Fourier transform infrared spectroscopy (ATR-FTIR)^{46,50} and X-ray photoelectron spectroscopy (XPS)⁴⁷, confirming the consumption of $-\text{CH}_3$ and generation of $-\text{Si}-\text{OH}$ during the UVO treatment. This renders PDMS surface highly hydrophilic as evidenced by corresponding changes in water contact angle from 107 to 45° depending on the treatment duration⁵², as shown in Figure 1.13. However, prolonged UVO treatment duration may also leads to the formation of a silica (SiO_x , $1 \leq x \leq 2$) network-like structure which hardens and increases the modulus of near-surface layer of the PDMS considerably, in a manner that can interrupt conformal contact.⁴⁵ In fact, several researchers have underlined that this form of oxidation could result in surface roughening⁴⁶⁻⁵⁰ and even crack formation due to the difference in thermal expansion coefficient between the bulk PDMS and silica-like layer⁵³. The thickness of the silica-like layers has been estimated to be about 5 – 160 nm.^{47,50,54} It is therefore, necessary

to precisely control the treatment parameters such as environmental condition, exposure distance, duration, *etc.*

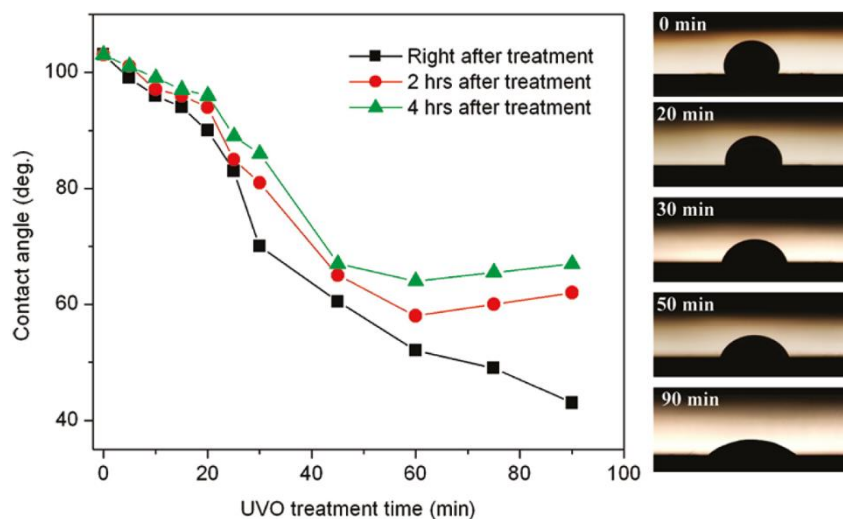


Figure 1.13: (Left) water contact angle as a function of UVO treatment and post-treatment time and (right) images showing water contact angles at different treatment times (0, 20, 30, 50, and 90 min, immediately after UVO treatment).⁵²

With the presence of highly polar and reactive surface terminated with silanol groups, the PDMS surface can react with various inorganic surfaces to form strong chemical bonds, simply upon physical contact at room temperature⁵⁵ or slightly elevated temperatures⁵⁶. Meanwhile, our as-fabricated SiNRs consist of a thin sheath layer of native oxide (as explained in section 1.4), and its contact with moisture in the ambient atmosphere might lead to formation of silanol groups (as illustrated in the right part of Figure 1.12) due to the diffusion of water molecules into the native oxide layer to interact with the lattice vacancies.⁵⁷ When both the oxidized PDMS and SiNRs are brought into contact, a strong covalent bond, *i.e.* siloxane (—Si—O—Si—) form between them through condensation reactions (as indicated in the red box in Figure 1.12), which may occur either at room temperature or as accelerated during baking at elevated temperatures (50-150°C).^{45,55,56} These chemical bonds are so strong that any attempt to

remove the ribbons from the oxidized PDMS surface causes cohesive failure or fracture of the ribbons.

In order to understand the implication of UVO treatment on the buckling mode of the nanostructures on the pre-strained substrate, it is important to shed light on the surface interaction between the two constituents. The surface interaction between the oxidized PDMS and SiNWs has been quantified by Qin and Zhu through the measurements of static friction force and interfacial shear strength based on “the most-bent state” of the wires, using AFM and micromanipulator. The shear strength was found to be 0.3 MPa for the unmodified system, while a maximum 10.57 MPa was reached when a 60-min UVO treatment was employed on the PDMS substrate.⁵² The changes in shear strength is likely to contribute to the variation of buckling modes in the buckled system.

In their prior work, Zhu and coworkers demonstrated that the buckling mode of the SiNWs having similar diameters (within 30 ± 5 nm) can be tailored from two-dimensional (2D) in-plane wavy to three-dimensional (3D) coiled shape in a controlled manner by tuning the UVO treatment duration of the pre-strained PDMS substrates.⁴⁴ The buckling profile captured by AFM reveals that the SiNWs adopted an in-plane wavy mode when no treatment was applied (Figure 1.14 (a)); and later gradually transformed into out-of-plane deformation mode (Figure 1.14 (c)) when UVO treatment duration increased to 5 min. Nevertheless, further increase of UVO treatment duration beyond 5 min resulted in disordering of the out-of-plane buckling mode and eventually a reversion to in-plane wavy structure, as illustrated in Figure 1.14 (d-e).

The underlying mechanism of the buckling mode transition is later attested by finite element method (FEM) simulation studies. Chen *et al.* modeled the buckling behavior of circular SiNWs on the PDMS substrate with different bonding conditions.⁵⁸

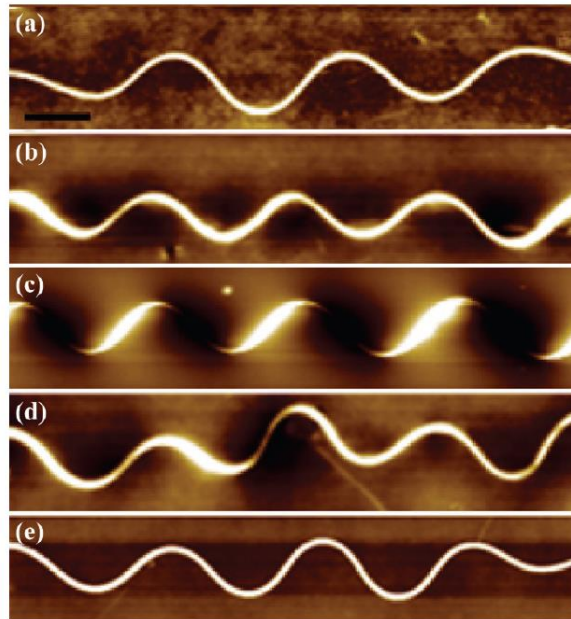


Figure 1.14: AFM images of deformed Si NWs on the PDMS substrate at different treatment times of (a) 0 min, (b) 3 min, (c) 5 min, (d) 8 min, and (e) 20 min. The pre-strains were all set to be 20%. Scale bar is $1\ \mu\text{m}$.⁴⁴

The bonding condition is varied by the amount of constraint points defined along the length of the wires. Higher density of constraint points, or in other words a shorter distance between the adjacent constraint points d , infers better adhesion between the wires and PDMS substrate. From the FEM results, the buckling modes of the wires as a function of d spacing can be divided into three regimes, as shown in Figure 1.15. When the d spacing is large with $d = 2.5$ and $1\ \mu\text{m}$, the SiNWs buckles in-plane in a sinusoidal form with a wavelength of $2d$. Out-of-plane buckling begins to exist when the d spacing becomes lesser than $1\ \mu\text{m}$. At $d = 0.8$ and $0.5\ \mu\text{m}$, the out-of-plane buckling pattern appears to be disorder but progressively transforms into helical coil form as the constraint density increases to a point where $d = 0.3$ and $0.1\ \mu\text{m}$. These observations further elucidate the claim from Zhu and coworkers who attributed the 2D in-plane buckling mode to the in-plane sliding of the SiNWs due to poor interfacial adhesion when no treatment is being applied, whereas perfect bonding between the

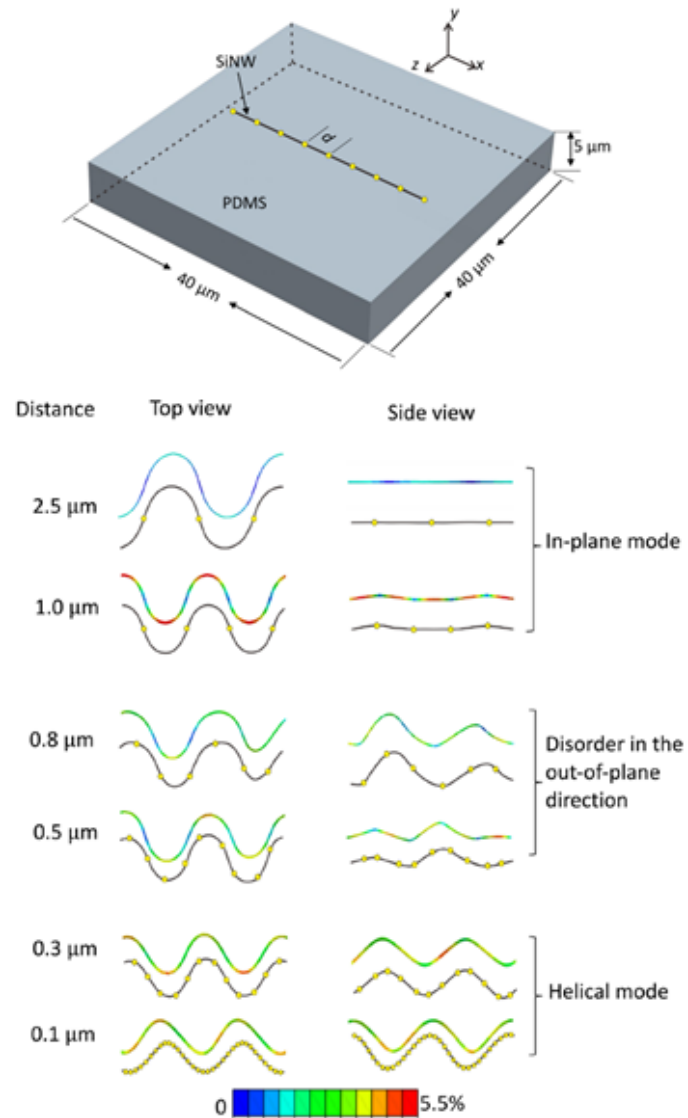


Figure 1.15: The buckling modes of the SiNW partially bonded to a PDMS substrate. The dots represent the constraints (bonded sites) between the SiNW and the PDMS substrate. Color contour of the maximum principal strain in the buckled configuration is given.⁵⁸

SiNWs and PDMS substrate enables the formation of 3D helical coil buckled architecture. Meanwhile, degeneration of the out-of-plane buckling mode observed by Xu *et al.* when the UVO treatment duration increased beyond 8 min is most probably due to the weakening of compliance of PDMS near the surface leading to debonding.

1.5.4 Hydrophobic recovery of oxidized substrate

While UVO treatment has facilitated the adhesion between the PDMS substrate and nanostructures through surface hydrophilicity modification of the PDMS, it must be noted that the PDMS tends to gradually regain its hydrophobicity after a certain relaxation time, and this phenomenon is termed as hydrophobic recovery. The driving force of hydrophobic recovery is associated to the surface free energy reduction. During the treatment, the introduction of polar silanol group concentration gradient in the surface or near-surface region of the PDMS results in the deviation from its thermodynamic equilibrium. After the treatment, the modified substrate surface reconstructs in order to minimize its surface energy and return to an equilibrium state.⁴⁹

A number of studies proposed that the mechanism of hydrophobic recovery involves migration of free non-modified low molecular weight (LMW) siloxanes from the bulk to the near surface region through a porous, or cracked silica-like layer. These free siloxanes are intrinsically present in the polymer network, as well as formed by UV-induced chain scission reactions during the treatment^{47,54,59,60}, as depicted in Figure 1.16. Kim *et al.* highlighted that LMW species are abundantly available when the humidity is $\geq 20\%$, resulting in a more pronounced hydrophobic recovery on the modified substrate surface.⁵⁹ Besides, the recovery effect is also attributed to the reorientation of chemical groups, especially those that near the surface and even the relaxation of surface roughness.^{47,49,54}

The hydrophobic recovery has been assessed on both the continuum scale with increasing water contact angle^{47-49,52,59,60} as well as on the micrometer scale with decreasing work of adhesion according to the JKR theory⁴⁷. Qin *et al.* reported that the recovery effect is likely the major mechanism for the decrease in static friction force between the oxidized PDMS and SiNWs after a prolonged relaxation time.⁵² It must,

therefore, be stressed that after the application of UVO treatment, the substrate surface hydrophobic recovery effect must not be neglected while gauging the treatment effectiveness on the enhancement of the interfacial adhesion between the substrate and the nanostructures.

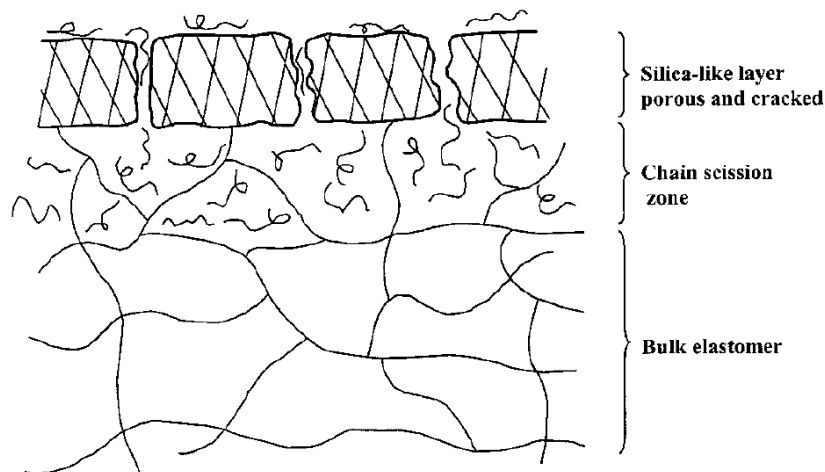


Figure 1.16: A schematic showing different zones that are produced on a PDMS as a result of exposure to partial electrical discharge. The uppermost surface is affected mostly, which converts to a silica-like layer. Beneath the silica-like layer, it is envisaged that the scission of polymer chain occurs. The silica-like layer is probably porous or cracked, through which the *in situ* produced low molecular weight species migrate and adsorb at the air–polymer interface. If free fluid is present in the network, it also contributes to the recovery process.⁵⁹

1.6 Objectives

With continuing interest in this buckling-based metrology technique to rapidly screen the mechanical property of nano-scaled materials, there lies an interest on implementing this technique on boron-based 1D nanostructures, as part of our long-term goals. Nevertheless, at this stage, the control of the order and morphology of the buckled nanostructures still remain elusive. As an explorative step, we aimed to employ a combined experimental- simulation approach (with the aid of analytical solution

available in the literature) to understand the buckling behavior of individual Si nanoribbons with the emphasis on the effect of aspect ratio along with its core-sheath structure and UVO surface treatment duration. Silicon nanoribbons were used in this dissertation work simply because of the more well-defined and consistent geometrical parameters, owing to its top-down fabrication technique, *i.e.* lithography patterning. Meanwhile, UVO surface treatment on the substrate was employed, having known that the interfacial adhesion between ribbons and substrate is ambiguous in practice; hence, its effect on the buckling profile was also investigated.

In this dissertation, Chapter 2 describes the materials and experimental methods employed in this work. In Chapter 3, the experimental results are presented along with the discussion on the buckling profile of the individual Si nanoribbons as a function of aspect ratio (inclusive of the core-sheath effect) and UVO surface treatment duration. The mechanics underlying the buckling behavior of the 1D nanostructure on a compliant substrate is elucidated in Chapter 4, based upon the work done by other researchers, to shed light on the buckling mode of the ribbons. Chapter 5 explains the approach employed to perform finite element modeling of the buckled ribbon on the elastomeric substrate. Lastly, conclusions of the dissertation work are outlined together with the proposed future work in Chapter 6.

CHAPTER 2: MATERIALS AND METHODS

This chapter describes the materials, test apparatus and characterization techniques employed in the dissertation work.

2.1 Fabrication of silicon nanoribbons

The silicon nanoribbons used in this work was provided by our collaborator, Dr. Deyu Li from the Vanderbilt University. The ribbons were fabricated using a top-down approach, *i.e.* lithographic patterning technique on a silicon-on-insulator (SOI) wafer⁶¹. The SOI wafer used (p-type boron doped Si (100) with a dopant density of $0.7-1.5 \times 10^{15} \text{ cm}^{-3}$, Simgui Technology Co., Ltd.) has a diameter of 6 inch (150 mm) with a 140 nm thick silicon device layer and a 500 nm buried oxide (BOX) layer. The fabrication process began with thinning down the silicon device layer to a specified thickness which later the ribbons would take. This was done by first subjecting the SOI wafer to a timed dry oxidation process to oxidize a targeted thickness of the silicon device layer, after which the resulted silicon oxide layer was removed with buffered oxide etch (BOE 6:1). The thickness of the remaining silicon device layer was measured using an ellipsometer.

After cutting the 6" SOI wafer into 30×30 mm pieces, the ~28 μm long Si nanoribbons of various aspect ratios were then defined using e-beam lithography (EBL) and reactive ion-plasma etching (RIE). The photoresist used in the EBL process was hydrogen silsesquioxane (HSQ) e-beam resist (XR-1541, 6%) which is a negative resist

and also a flowable oxide with good etching resistance and present high resolution. The HSQ-coated SOI chip was later patterned into ribbons of various aspect ratios under the e-beam exposure (JEOL 6300). Upon developing the exposed HSQ e-beam resist, the uncoated silicon device layer was etched away through plasma etching (PlasmaTherm 770). In order to form freestanding structures, the underneath BOX layer, together with the HSQ e-beam resist, were removed using wet hydrofluoric acid (HF) etching (10:1) and critical point drying to release the Si nanoribbons. The resulting structure features the ribbons anchored by two separate islands, as illustrated in Figure 2.1 (a). A high-resolution transmission electron microscopy (HRTEM) micrograph of an individual Si nanoribbon is presented in Figure 2.1 (b), featuring an amorphous sheath around the single crystalline core. As evident in the selected area electron diffraction (SAED) image in the inset of Figure 2.1 (b), the ribbon was patterned along the $\langle 110 \rangle$ direction.

After the fabrication process, a soft substrate such as polydimethylsiloxane (PDMS) was used as a receiver substrate to transfer the silicon nanoribbons from the SOI chip (donor substrate) via a simple stamping process. Later, the individual nanoribbons were detached from the anchors using a sharp probe mounted on a micromanipulator. The detached individual nanoribbons were later employed in the subsequent mechanical buckling process.

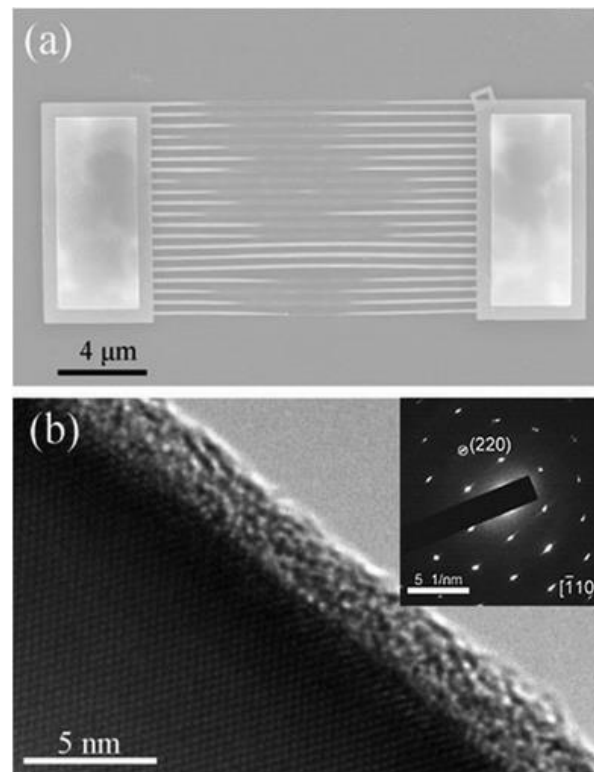


Figure 2.1: (a) An SEM micrograph of the as-fabricated silicon nanoribbon array. (b) An HRTEM micrograph of an individual silicon nanoribbon. The inset in (b) shows a SAED pattern of the nanoribbon taken along the $[\bar{1}10]$ zone axis.⁶¹

2.2 Dimensional study of the silicon nanoribbons

The dimension of the as-fabricated Si nanoribbons were measured using the HRTEM. As we were aware that the as-fabricated Si nanoribbons in this study are of composite coaxial structures, *i.e.* an Si nanoribbon surrounded by an SiO₂ sheath of native oxide, the use of HRTEM would allow us to determine the dimension of the Si core and the thickness of the surface oxide layer precisely. This is important as the presence of the surface oxide layer imposes great impact on the effective properties of the nanostructure^{39,40,42}. The ribbons were picked up from the receiver substrate using a sharp probe mounted on the micromanipulator and laid on a lacey carbon-coated TEM copper grid. For the ribbon width measurement, the ribbons were laid flat on the support

film of the TEM grid, while the height measurement required the ribbons to be bent so that the edges of the ribbons were curved up to allow height measurement.

The dimensional study of the Si nanoribbon was conducted using a JEOL JEM-2100 LaB₆ TEM operating at an accelerating voltage of 200 kV, with the use of a JEOL double-tilt holder (allowable tilting angle of $\pm 30^\circ$ in both x and y -directions). TEM images and diffraction patterns of the ribbons were captured by the CCD camera (SC1000 ORIUS TEM CCD camera from Gatan) and the DigitalMicrograph software. A minimum of three ribbons were used to determine the measurement of each dimension.

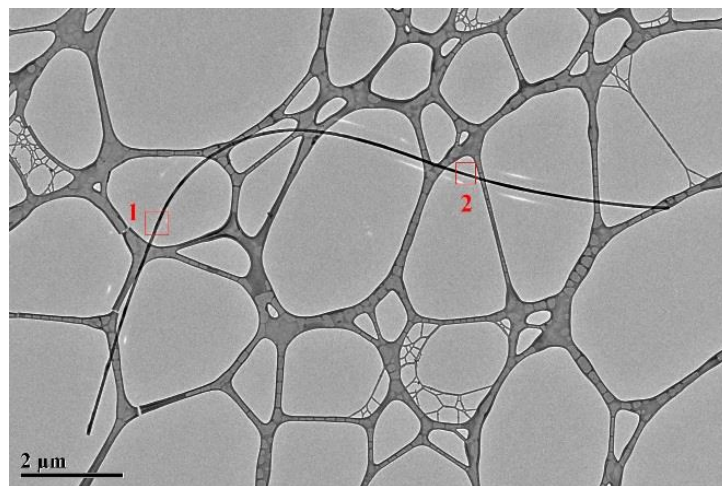


Figure 2.2: An TEM micrograph of a bent silicon nanoribbon laid on a lacey carbon-coated grid for thickness measurement.

2.3 Preparation of compliant substrate from polydimethylsiloxane (PDMS)

The compliant substrate used in this study was Sylgard 184 silicone elastomer manufactured by Dow Corning. It is supplied as a two-part liquid component kit, a pre-polymer (base) and a cross-linker (curing agent), that when mixed together is curable at both room temperature and elevated temperature ($\leq 200^\circ\text{C}$). The mechanical

properties of the PDMS polymer can be manipulated by varying the mixing ratios. In this study, the PDMS substrate was prepared in accordance with the manufacturer's recommendations, *i.e.* 10 parts base to 1 part curing agent (by weight). The mixture were then stirred thoroughly for 5 min and followed by degassing in a vacuum chamber for 30 min to remove entrapped air bubbles. Subsequently, the degassed mixture was poured into the casting mold (3D-printed ABS in this work) and allowed to cure at room temperature for 48 h. While pouring the mixture into the mold, care should be taken to minimize air entrapment. The ABS mold was designed according to ASTM D412 in a minimized version (Figure 2.3).

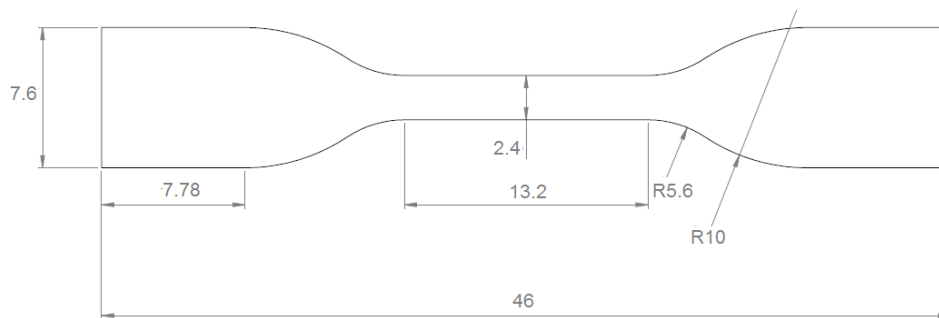


Figure 2.3: Dimensions of compliant substrate following ASTM D412 with 40% reduction in size.

2.4 Fabrication of stretching device

To demonstrate the mechanical buckling of Si nanoribbon on the compliant substrate, a stretching device is required to uniaxially stretch the PDMS substrate to a specific strain value prior to the deposition of Si nanoribbon. As such, a portable stretching device which can be fitted in a commercial uniaxial tensile machine and optical microscope (for the purpose of transferring Si nanoribbons with the aid of micromanipulator) was custom-built. The stretching device made of aluminum

comprises a Newport linear translation stage, a pair of sample clamps covered with polishing paper and a stoppage mechanism. Figure 2.4 depicts the home-built stretching device. The ability to integrate the home-built stretching device on the commercial Instron uniaxial tensile machine enables a precise strain rate control while applying and releasing pre-strain in the PDMS substrate. This is crucial as the Young's modulus of the PDMS substrate is a function of strain rate.⁶²

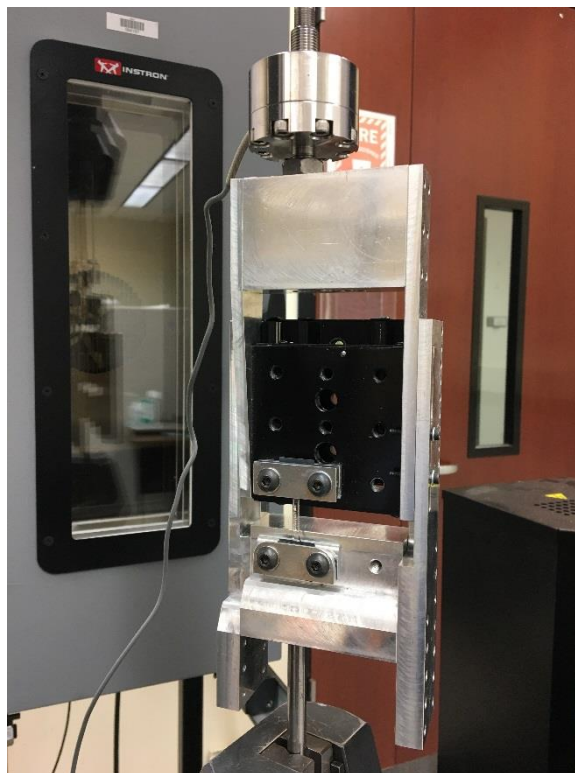


Figure 2.4: Home-built stretching device installed in an Instron uniaxial tensile machine.

2.5 Mechanical buckling

In this work, the PDMS substrate was positioned perpendicular to the longitudinal axes of the clamps. Clamping the PDMS substrate with the aid of polishing paper is crucial to prevent slippage of PDMS substrate during the uniaxial stretching

up to a pre-strain value of 100%. The as-prepared PDMS in this work has a fracture strain of 127%. To apply pre-strain on the PDMS substrate, the stretching device with the PDMS being tightly gripped was installed in the Instron tensile machine, as illustrated in Figure 2.4. A strain rate of 10 mm/min was applied and the amount of strain was measured by an advanced video extensometer (AVE) based on the displacement of two dots marked on the PDMS substrate surface. The video extensometer has a resolution of 0.5 μm at 35 mm focal length. Once the pre-strain of 100% was achieved, two nuts along the sliding rail at the stretching device, which act as the stoppage mechanism, was tightened to maintain the PDMS substrate in an elongated condition for the subsequent processes. The stretching device was then removed from the tensile machine.

2.6 Surface treatment of the PDMS substrate

In order to enhance the adhesion between the Si nanoribbon and the PDMS substrate during the mechanical buckling process, it is necessary to modify the surface properties of the substrate. One common route to the modification of the PDMS surface is the ultraviolet/ozone (UVO) treatment, which simultaneously utilizes UV light and ozone produced *in situ* to photochemically modify the polymer surface.⁶³ Oxidizing the PDMS surface by ultraviolet-induced ozone (O_3) produces a surface capable of forming strong chemical bonds with a wide range of materials that come in contact with it, simply upon physical contact at room or slightly elevated temperatures.⁴⁵

In this work, the pre-strained PDMS substrate was radiated under a UV lamp (low-pressure mercury lamp, min intensity of 30 $\mu\text{W}/\text{cm}^2$ for 254 nm primary wavelength and 16 $\mu\text{W}/\text{cm}^2$ for 185 nm wavelength at the distance of 20 cm from the lamp, BHK) at the distance of 7 mm, with treatment duration varied at 0, 90 and 150 s.

This was followed by the transfer of the nanoribbon onto the substrate surface. A sharp probe mounted on the micromanipulator was used to transfer the ribbon from the receiver substrate onto the pre-strained PDMS substrate surface. For the UVO-treated PDMS substrate, the transfer process duration must not exceed 15 min as the hydrophobic recovery effect becomes pronounced.⁵² The effect of treatment duration and relaxation time on the surface properties of the substrate is elaborated in detail in section 3.2.

In order to promote intimate contact between the ribbon and the substrate after the transfer process, a tiny piece of Si wafer (5×5 mm) was used as a weight block to apply slight pressure of onto the PDMS surface containing the ribbon. Caution must be taken to ensure that the surface of Si wafer, which was in contact with the PDMS substrate, was thoroughly cleaned (with chemical solutions and oxygen plasma) to avoid contaminating the ribbons. The contact time between the PDMS substrate and the weight block was limited to ~1 min in order to prevent unwanted bonding between the two substrate surfaces. Upon removal of the weight block, the bonding between the ribbon and PDMS substrate was allowed to run to completion (>10 min at room temperature) before releasing the pre-strain.^{16,31} As the pre-strain in the PDMS substrate was released under the compression mode in the tensile machine at a rate of 10 mm/min, the Si nanoribbon became buckled.

2.7 Measurement and analysis of ribbon buckled profile

As the ribbons buckled in distinct modes under varying test parameters, different characterization tools were needed. An optical microscope was used initially to identify the buckling mode of the ribbons, whether an in-plane or out-of-plane buckling had occurred. For ribbons that buckled on the same plane as the substrate

surface, the optical microscope was also employed to determine both the buckle wavelength and amplitude. The wavelength is determined by measuring the distance between two fixed points in the image and dividing it by the number of waves in between; whilst the half distance between the peaks and valleys defines the amplitude. This measurement leads to a more accurate value than that from a single wave measurement, because averaging of many waves that have different wavelength values.¹⁸ However, knowing that optical microscope has limited resolutions, measurements were also carried out using tapping mode atomic force microscope (DimensionTM 3100, Veeco) to verify the buckling behavior observed using optical microscope. Meanwhile, a laser scanning confocal microscope (LEXT OLS 4000, Olympus) was used to study the buckling profile of ribbons demonstrating out-of-plane deformation. The use of LSCM allows high resolution three-dimensional (3D) imaging as well as fast 3D measurements of the ribbon buckling profile. LSCM images presented in this work are in two-dimensional (2D) intensity projection or 3D topographic profile and they are representative of a series of overlapping optical slices (a stack of z-scan images) with each z-step measuring 0.06 μm . Each frame consisted of 1024×1024 pixels and $32 \times 32 \mu\text{m}$ in size. The laser wavelength used was 405 nm.

CHAPTER 3: EXPERIMENTAL RESULTS AND DISCUSSION

This chapter discusses the experimental outcomes of the dissertation work, which is divided into three sections: (i) dimensional study of the silicon nanoribbons, (ii) buckling of ribbons as a function of aspect ratio, and (iii) effect of UVO surface treatment on the buckling profiles of the ribbons on the compliant substrate.

3.1 Dimensional study of silicon nanoribbons

The silicon nanoribbons employed in this work were fabricated via e-beam lithographic patterning on a SOI wafer, as described in section 2.1. One unique aspect of this fabrication method is that lithography defines the lateral dimensions of the nanoribbons and their spatial position across the wafer; while oxidation and etching diminish the thickness of the nanoribbons uniformly and release the top silicon layer to form freestanding structures, as illustrated in Figure 3.1.⁶⁴ Based on the prior measurements provided by Dr. Li's group members, the thickness of the top Si layer was thinned down to 30 nm before lithographic patterning and RIE etching were employed to produce Si nanoribbons with dimensions as listed in Table 3.1.

To ensure that the structures designed using lithographic patterning technique exhibits high controllability and repeatability, dimensions of the as-fabricated Si nanoribbons were precisely measured using HRTEM. As the Si nanoribbons were transferred onto the lacey carbon-coated TEM grid using a sharp probe mounted on the micromanipulator, it is highly possible that the Si nanoribbons were oriented differently from one mesh to another. Therefore, it is important to warrant that the Si nanoribbons

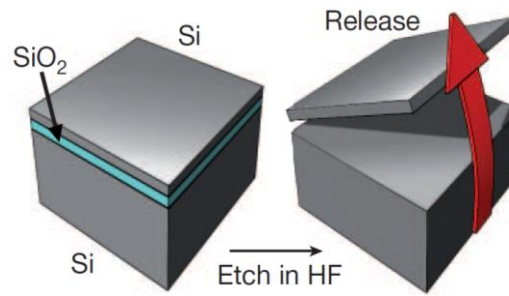


Figure 3.1: Release of silicon nanostructure from a SOI wafer by etching vertically through the top silicon layer to expose the underlying SiO₂ layer which is later removed by etching in hydrofluoric acid.⁶⁴

Table 3.1: Targeted dimensions of as-fabricated silicon nanoribbons.

Nanoribbon convention (b, h)	Width, b (nm)	Height, h (nm)	Length (μm)
(40, 30)	40	30	18
(60, 30)	60	30	28
(80, 30)	80	30	28
(100, 30)	100	30	28
(200, 30)	200	30	28

were imaged at a definite zone axis because tilting of the sample could lead to undesirable measurement errors.

Knowing the patterning orientation of the nanostructures, one could identify the crystallographic information (*i.e.* crystallographic direction and plane) of different faces of the ribbon. Figure 3.2 illustrates the crystal orientation of the SOI wafer used in the lithographic patterning. Based on the manufacturer's specification, the SOI wafer used is composed of single crystalline Si grown along the $\langle 100 \rangle$ direction; therefore, the top surface of the SOI wafer is oriented on (100) plane. This implies that the zone axis should be oriented at $\langle 100 \rangle$ direction while imaging the width of the ribbons, so that the true width value can be measured (Figure 3.3 a-b). Meanwhile, as the ribbons were patterned either parallel or perpendicular to the flat edges of the wafer, the height

of the ribbons should be imaged along the $\langle 110 \rangle$ zone axis to retrieve the true height value (Figure 3.3 c-d).

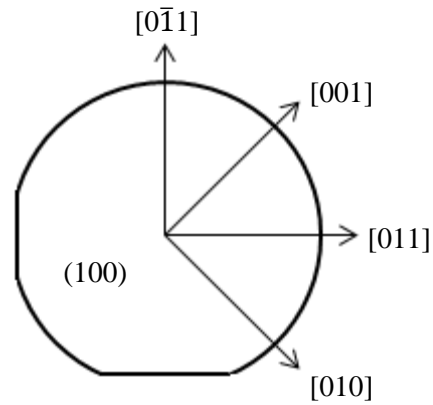


Figure 3.2: Crystal orientation of (100) Si wafer used in lithographic patterning.

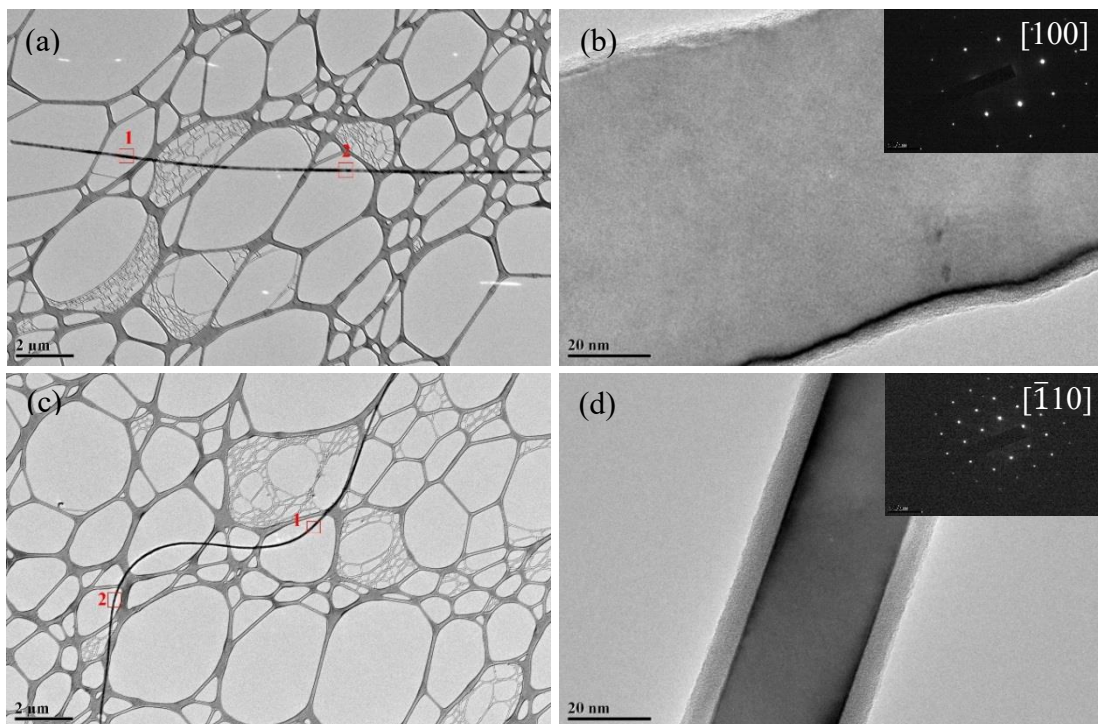


Figure 3.3: TEM micrographs of Si nanoribbon being (a) laid flat for (b) width measurement, and (c) tilted for (d) thickness measurement. The insets in (b) and (d) show the respective SAED pattern of the nanoribbon taken along the $[100]$ and $[\bar{1}10]$ zone axis.

As revealed earlier, our early studies indicated that as-fabricated nanoribbons consist of single crystalline silicon core and thin amorphous oxide sheath.^{61,65} Figure 3.4 shows the schematic illustration of a cross-sectional view of the ribbon having core-sheath structure. In this dimensional study, three ribbons were measured for each size to obtain respective average ribbon outer width B while a total of 7 measurements was acquired to determine the average ribbon outer height H . Meanwhile, the average thickness of the oxide sheath was retrieved from all imaged samples, regardless of the ribbon faces. Table 3.2 tabulated the average measurements of ribbon width and height as well as native oxide sheath thickness. It is noted that the average ribbon width and height values reported here are inclusive of the sheath thickness. A close review on the measurement results reflects that the broadening of the ribbon width and height was a consequence of the presence of approximately 5 nm-thick amorphous oxide layer surrounding the Si core.

Table 3.2: Average dimensions of as-fabricated Si nanoribbons.

Nanoribbon convention (b, h)	Average outer width, B (nm)	Average outer height, H (nm)	Aspect ratio (B/H)	Average thickness of oxide layer (nm)
(40, 30)	48.1 ± 0.8	40.6 ± 0.3	1.19	5.1 ± 0.3
(60, 30)	68.2 ± 1.4		1.68	
(80, 30)	88.46 ± 1.5		2.18	
(100, 30)	109.6 ± 1.0		2.70	
(200, 30)	208.0 ± 1.9		5.12	

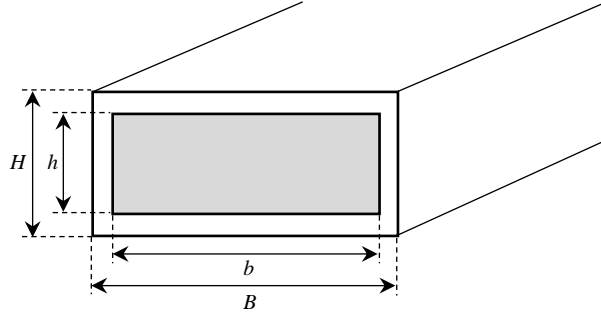


Figure 3.4: Schematic illustration of a cross-section of our as-fabricated Si nanoribbon having core-sheath structure. Shaded region refers to the Si core, which is surrounded by a thin layer of SiO₂ sheath.

3.1.1 Effect of core-sheath structure on the ribbon bending stiffness

Since cross-sectional examination of the as-fabricated Si nanoribbons revealed a composite coaxial structure, the buckling properties of the ribbon should be accounted for the presence of the amorphous oxide layer surrounding the ribbon core. The classical mechanics theory of compound materials^{38,40,42} outlines the effective modulus of the ribbon as follows

$$E_{eff}I = E_c I_c + E_s I_s \quad (3.1)$$

where E denotes the Young's modulus, I is the area moment of inertia and subscript c and s refers to the Si core and SiO₂ sheath, respectively. For a rectangular cross-section, the area moment of inertia with respect to the y -axis is given as $I = B^3 H / 12$, I_c and I_s therefore take the following forms

$$I_c = \frac{b^3 h}{12}, \quad (3.2)$$

$$I_s = \frac{B^3 H - b^3 h}{12}. \quad (3.3)$$

Re-arranging Eq. (3.1) gives

$$E_{eff} = \alpha_1 E_c + (1 - \alpha_1) E_s \quad (3.4)$$

where

$$\alpha_1 = \frac{b^3 h}{B^3 H}. \quad (3.5)$$

Therefore, for an in-plane buckling, effective modulus of the ribbons would take form depicted in Eq. 3.4. Meanwhile, ribbons buckled in a 3D coiled-like structure have effective modulus as denoted in Eq. (3.6) for the area moment of inertia with respect to the x -axis is given as $I = BH^3/12$.

$$E_{eff} = \alpha_2 E_c + (1 - \alpha_2) E_s \quad (3.6)$$

where

$$\alpha_2 = \frac{bh^3}{BH^3}. \quad (3.7)$$

In the following sections, effective modulus are being used instead, to assess the buckling behavior of the Si nanoribbons having core-sheath structure.

3.2 Buckling of Si nanoribbons as a function of ribbon aspect ratio

Mechanical buckling of Si nanoribbons was evaluated based on the resulting buckling profile, *i.e.* buckling mode, wavelength and amplitude. As reviewed in section 1.5, the ribbons could possibly buckled into in-plane or out-of-plane mode, depending on the geometrical parameters and adhesion properties. In that sense, the selected measurement method should be capable of acquiring all buckling outcomes. While optical microscope (OM) served as the primary measurement method, comparison was also made with atomic force microscope (AFM) and laser scanning confocal microscope (LSCM) to study the buckling profile of in-plane- and out-of-plane-buckled ribbons, respectively. It is noted that, between buckling wavelength and amplitude, the wavelength information is considered as a more important output than the amplitude because the wavelength depends less strongly on the pre-strain amount and residual

surface roughness of the PDMS substrate, and can therefore be measured with greater accuracy.¹⁴ With that thought in mind, emphasis of the following sections is concentrated on the results of buckling mode and wavelength only.

3.2.1 Measurement techniques of buckling wavelength

As the ribbons buckled upon the release of pre-strain, the buckling profile was first observed using optical microscope to determine the buckling mode and wavelength. Meanwhile, in order to verify the accuracy of the wavelength measurements using OM, AFM or LSCM was used subsequently. The fact is that, the accuracy of the measurements depends on the spatial resolution of instrument used. It is known AFM has better spatial resolution than that of OM owing to its nano-sized dimension of the stylus tip, whilst LSCM has a lateral resolution of at least 3.5 times better than that of OM; both AFM and LSCM are therefore capable of providing the most accurate wavelength measurement. However, while the measurement accuracy is indisputable, these two techniques are complicated and laborious, making OM measurement a favorable one if the measurement error becomes negligible.

A comparison of wavelength and amplitude measurements between OM and AFM techniques on an in-plane-buckled Si nanoribbon (as illustrated in Figure 3.6) is tabulated in Table 3.3. With a measurement error observed at below 1%, it appears that the measurements performed using OM is acceptable in this context. With this regard, all measurements on in-plane buckled ribbons reported in the subsequent sections are based on OM technique.

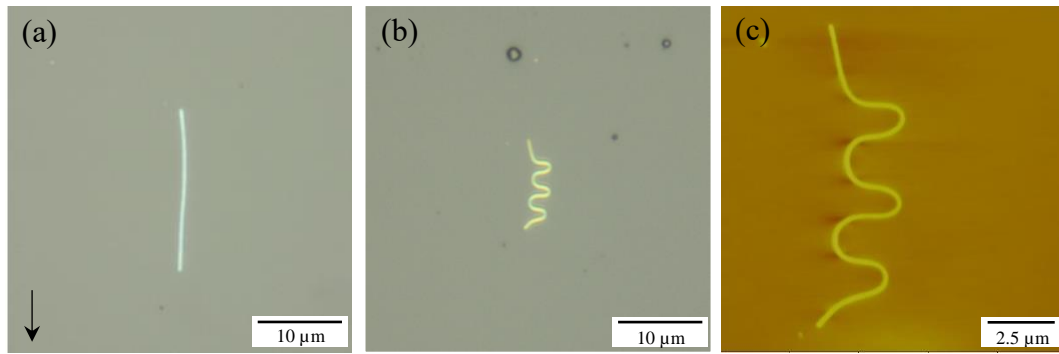


Figure 3.6: Optical microscope imaging of buckling profile of an in-plane-buckled Si nanoribbon on a PDMS substrate (a) prior to and (b) upon release of the pre-strain; (c) atomic force microscope scanning of the buckled ribbon in (b). The arrow in (a) shows the direction of pre-strain application.

Table 3.3: Comparison of wavelength and amplitude measurements of an in-plane-buckled Si nanoribbon using optical and atomic force microscope.

Measurements	AFM (μm)	OM (μm)	Difference (μm)	Error (%)
Wavelength, λ	2.881	2.86	0.021	0.73
Amplitude, a	1.001	1.01	0.009	0.90

As for out-of-plane-buckled ribbons, measurement using AFM is not feasible as the contact between stylus and specimen may result in the collapse of the free-standing ribbons. Thus, a non-destructive alternative of characterizing the buckling profile of an out-of-plane-buckled ribbon is to employ a laser scanning confocal microscope (LSCM). Not only can LSCM resolves smaller detail than a conventional OM, it also allows one to acquire a 3D image for visualization, manipulation and measurement purposes. Figure 3.7 shows a ribbon buckling out-of-plane observed using OM and LSCM. A comparison of wavelength and amplitude measurements between these two techniques is depicted in Table 3.4. Similar to the previous finding, the measurement error found between OM and LSCM technique is so trivial that OM measurement fits our purpose. Meanwhile, it is noted that amplitude measurement is not reported using OM as it only produces a 2D image.

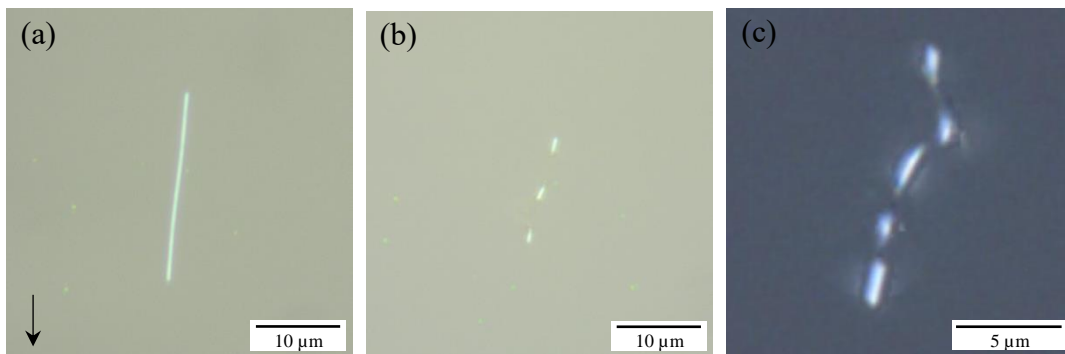


Figure 3.7: Optical microscope imaging of buckling profile of a Si nanoribbon buckling out-of-plane on a PDMS substrate (a) prior and (b) upon release of the pre-strain; (c) laser scanning confocal microscope scanning of the buckled ribbon in (b). The arrow in (a) shows the direction of pre-strain application.

Table 3.4: Comparison of wavelength and amplitude measurements of an out-of-plane-buckled Si nanoribbon using optical and laser scanning confocal microscope.

Measurements	CLSM (μm)	OM (μm)	Difference (μm)	Error (%)
Wavelength, λ	5.529	5.51	0.019	0.34
Amplitude, a	2.816	N.A.	N.A.	N.A.

Even though LSCM could provide amplitude measurement from the acquired 3D image, the accuracy of the measurement becomes questionable when an inhomogeneous structure (*i.e.* composed of materials with different refractive index, RI or η) is being examined. Refractive index differences between various material structures can cause the incident ray to deviate from its original path, producing defocusing errors.⁶⁶ According to the literatures, refractive index for PDMS and Si are 1.4220⁶⁷ and 5.4453 at 405 nm laser wavelength (*i.e.* the type of laser used in our LSCM), respectively. In this case, in order to establish that the amplitude measurement obtained from LSCM is accurate, one needs to deduce the actual value by taking into account of the change of ray reflection travelling through mediums of different refractive index. Such a pertinent expression was proposed by Sung *et al.* whereby the

film thickness of a thermoset coating on a silicon substrate could be precisely determined using LSCM and the results were in good agreement with measurements retrieved from SEM and interference microscopy (IM).⁶⁸ Nevertheless, since amplitude is not a significant buckling outcome in this work, it will not be discussed further in this dissertation.

3.2.2 Buckling wavelength as a function of ribbon aspect ratio

With the use of optical microscope, the buckling wavelength of the ribbons on the substrate upon the release of 100% pre-strain were observed. Based on Figure 3.8, the buckling wavelength of the ribbons on a pristine substrate increased with the width of the ribbons. All ribbons had similar thickness of 28.66 ± 0.24 nm with a sheath layer of 4.88 ± 0.38 nm-thick oxide surrounding them. Variations of Young's moduli and area moment of inertia of the ribbons with respect to the dimensions are accounted for the change in the buckling wavelength. The three-point bending test results reported by our collaborator pointed out that the Si nanoribbon Young's moduli increases ~6% from the 49 nm-wide ribbons to that of the 207 nm-wide one.⁶¹ Additionally, since our ribbons adopted a core-sheath morphology, the effective Young's moduli of the ribbons takes the form as expressed in Eq. (3.1). With the dimensional information provided in section 3.1, one could easily deduce that the area moment of inertia of the ribbon increases as the ribbon width becomes larger, so does the effective Young's moduli. Larger area moment of inertia implies greater resistance to buckling, resulting in greater

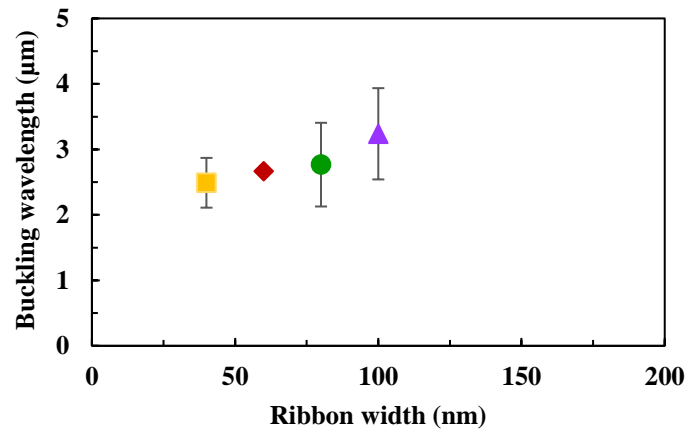


Figure 3.8: Buckling wavelength of Si nanoribbons as a function of ribbon width. All ribbons have a constant thickness of ~ 30 nm (exclusive of an oxide sheath layer of ~ 5 nm thick).

wavelength.⁶⁹ Hence, the wider ribbons having greater moduli and moment of inertia lead to the increase of the buckling wavelength. In fact, the governing equation of the beam-on-substrate buckling mechanics developed by the Rogers's group reflects that the buckling wavelength of the beam is proportional to its modulus and area moment of inertia^{12,14,15}, as expressed as follows

$$\lambda \propto 2\pi \left(\frac{E_b I_b}{E_s} \right)^{1/4}. \quad (3.8)$$

On the other hand, wavelength measurement of the 200 nm-wide ribbons was not possible because only one buckle was formed during the deformation (as shown in Figure 3.9e). Based on the theory of area moment of inertia⁷⁰, the wider ribbons having larger area moment of inertia possess greater resistance to buckling. This is true as half of the ribbons tested did not buckle upon the release of pre-strain during the experiment. According to the analytical solution proposed by other researchers^{12,14,15,18}, a rough estimation on the buckling wavelength shows a value of approximately $4 \mu\text{m}$, thus a minimum total length of $37 \mu\text{m}$ (inclusive of the edge-effect length due to the edge boundary condition⁷¹) is needed to observe the formation of two peaks during

deformation. With the existing length constrained at 28 μm , the buckling deformation of the 200 nm-wide ribbons appeared to be considerably demanding.

On the other hand, the standard deviation observed on the measured buckling wavelength is significant due to the ribbon transfer method employed in this work. Unlike the previous work where the nanostructures were mainly contact-printed onto the substrate surface^{12,14,44}, we used a sharp probe attached on the micromanipulator to transfer individual ribbons onto the pre-strained PDMS substrate surface. Even though we had taken several precautionary steps (*i.e.* used probe to roll along the ribbon surface and applied a weight block after the transfer) to ensure that the ribbons were laid flat on the substrate surface, it was possible that the ribbons could have been placed at an inclined angle from the substrate surface, resulting in the change of its area moment of inertia. Area moment of inertia of a ribbon tilted at an incline angle α takes the form below

$$I_x = \frac{BH}{12} (B^2 \cos^2 \alpha + H^2 \sin^2 \alpha). \quad (3.9)$$

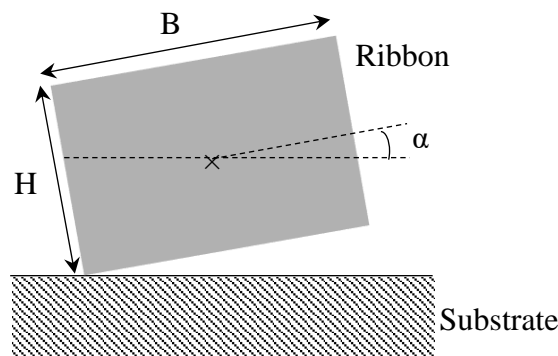


Figure 3.8: Schematic illustration of a ribbon having a rectangular cross-section being tilted at a specified angle α from the substrate surface.

According to Eq. 3.9, an increase in the incline angle α leads to an increase in the area moment of inertia of the ribbon, which ultimately causes the buckling wavelength to rise. For the same incline angle, its effect on ribbons with greater aspect

ratio is more prevalent. For instances, at an incline angle of 10° , the increase in the ribbon buckling wavelength is approximated at 5% and 20% for ribbons having width of 60 nm and 100 nm, respectively. It is noted that this phenomenon only occurs in structures having cross-section of unequal area moment of inertia, like rectangular.

3.2.3 Buckling mode as a function of ribbon aspect ratio

Two categories of buckling mode, in-plane and out-of-plane were observed in this work. Examination of the structure of the buckled ribbons was carried out using both optical microscope and atomic force microscope. Figure 3.9 displays the influence of aspect ratio (B/H) on the buckling mode of the ribbons at 100% pre-strain. Each result represents the observation of a minimum of five buckled ribbons.

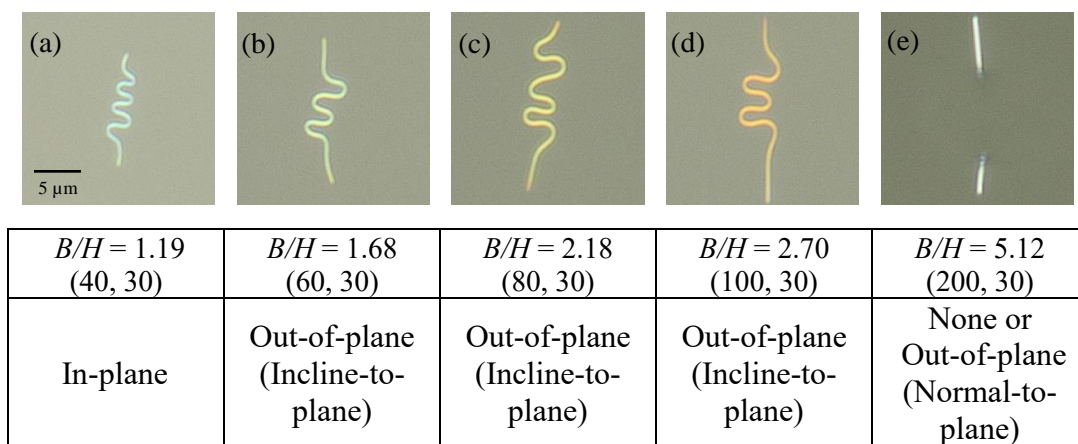


Figure 3.9: Optical images of buckled Si nanoribbons of varying aspect ratio (a) 1.19, (b) 1.68, (c) 2.18, (d) 2.70 and (e) 5.12 under 100% pre-strain. Scale bar in (a) is applicable to all images.

A quick glance on the optical images of buckled ribbons shown in Figure 3.9 indicates that in-plane buckling was prominent on all ribbons except the one with greatest aspect ratio of 5.12. However, it is noted that the resolution of the optical microscope (Olympus BX51) used is approximated at 250 nm in the lateral dimension

and approaching 1.25 μm in the axial dimension when using an objective lens of 100 \times magnification with a numerical aperture of 0.80. It is, therefore, unjustified to determine the buckling mode of the ribbons based upon the observation of the optical images. Instead, tapping mode atomic force microscopy technique was employed to trace the topography of the buckled ribbons on elastomeric substrate at near-contact.

Whilst the dimensional study of the ribbons using TEM revealed that all ribbon are of 40.6 ± 0.3 nm thick consistently (inclusive of the oxide sheath layer), the height measurement of the ribbons on the elastomeric substrate acquired through the tapping mode AFM shown varying average height measurements at different ribbon aspect ratios, as depicted in Table 3.5. Inconsistency in height measurement values across all ribbon sizes obtained using AFM could be a form of artifact due to the tip-sample interaction. On another note, we observed that the ribbon height measured on Si substrate is comparable to that of TEM measurement. Even though the AFM height measurements performed on the elastomeric substrate are not a true representation of the ribbon height, these measurements serves as an important information for comparison purpose in the subsequent discussion.

On a pristine compliant substrate, Si nanoribbons with aspect ratio 1.19 indeed exhibited in-plane buckling mode upon the release of 100% pre-strain, as observed in optical images. Figure 3.10 (a) provides plane-view AFM image and line cut profile along the wavy Si nanoribbons with aspect ratio 1.19. The line cut taken across the buckled ribbon shows a step height of magnitude less than 15 nm, which reflects the height of a ribbon being laid flat on the substrate surface, as mentioned in Table 3.5. It is, this a direct indication of the absence of out-of-plane displacement associated with the buckling. The magnified scan across the buckle, as presented in Figure 3.11 (a), further attested the presence of in-plane buckling mode associated with ribbons of

aspect ratio 1.19 where a line cue profile having a flat top surface is observed, with a width measuring about 49 nm, resembling the width of the 40 nm-wide ribbon with a 5 nm-thick oxide sheath layer.

Table 3.5: Height measurements of Si nanoribbons laid flat on the PDMS substrate surface acquired through tapping mode AFM.

Nanoribbon convention (b, h)	Aspect ratio (B/H)	Average height (nm)
(40, 30)	1.19	19.9 ± 0.8
(60, 30)	1.68	23.5 ± 1.3
(80, 30)	2.18	22.7 ± 1.4
(100, 30)	2.70	32.2 ± 2.8
(200, 30)	5.12	40.2 ± 3.0

As the aspect ratio increases to 1.68, the ribbons changed the buckling mode from in-plane to out-of-plane. Though the step height measured from the buckled ribbon (Figure 3.10 b) is similar to that of the flat one (Table 3.5), the line cut at the buckle shows an arch profile with a narrow peak width of 37.109 nm (Figure 3.11 b), approaching the intrinsic ribbon height. The arch profile is contrasting the trapezoid-like profile observed at the buckled ribbon with aspect ratio 1.19, where the top surface is relatively broad and level. This infers that the ribbons possibly buckled out-of-plane with the ribbons lifted off from the substrate surface at an incline angle, as illustrated in Figure 3.12 (a).

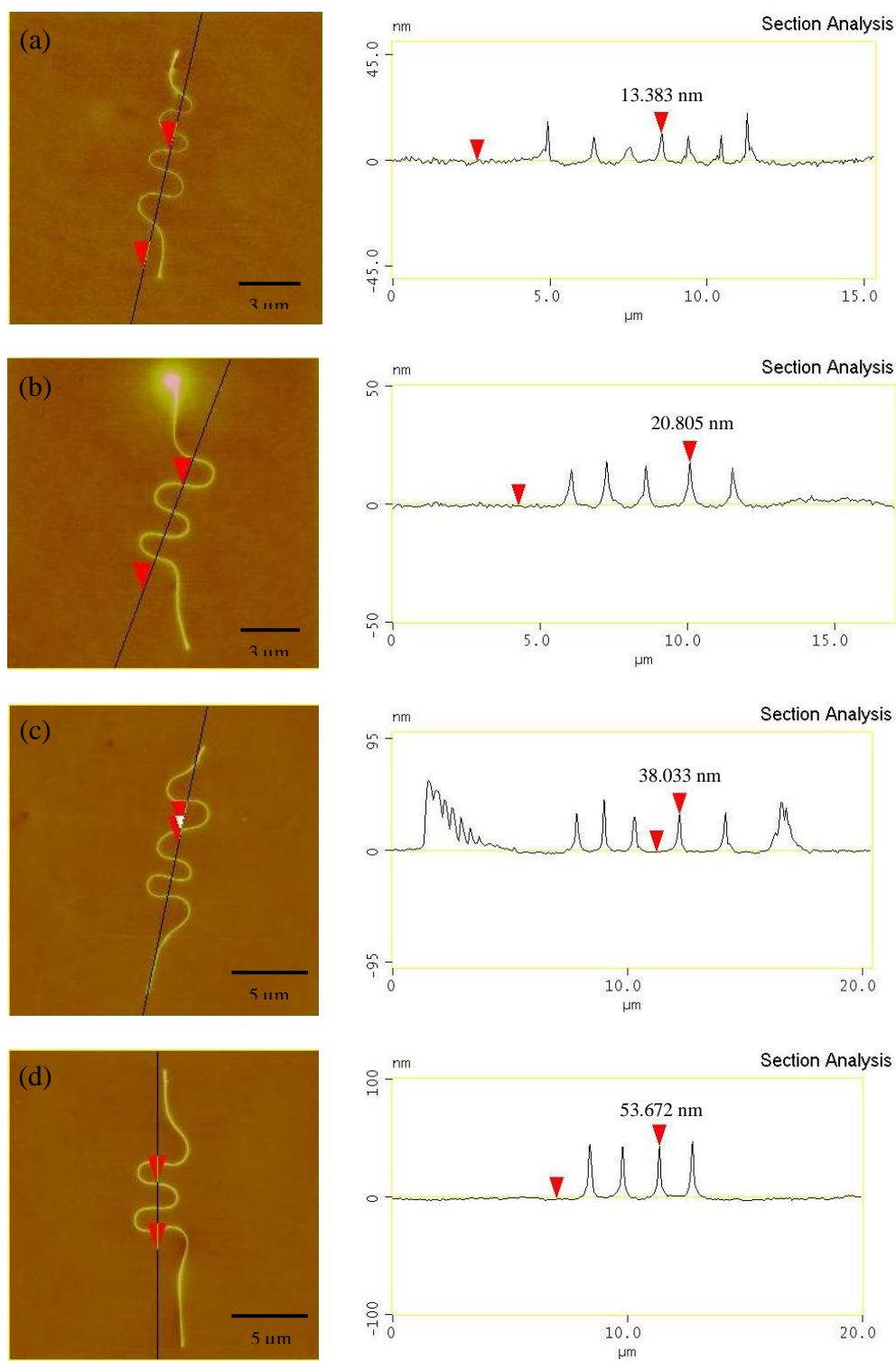


Figure 3.10: Plane-view AFM images of wavy Si nanoribbons with aspect ratio of (a) 1.19, (b) 1.68, (c) 2.18 and (d) 2.70. The right panel illustrates the respective topographical scan across the line cut of the buckled ribbon.

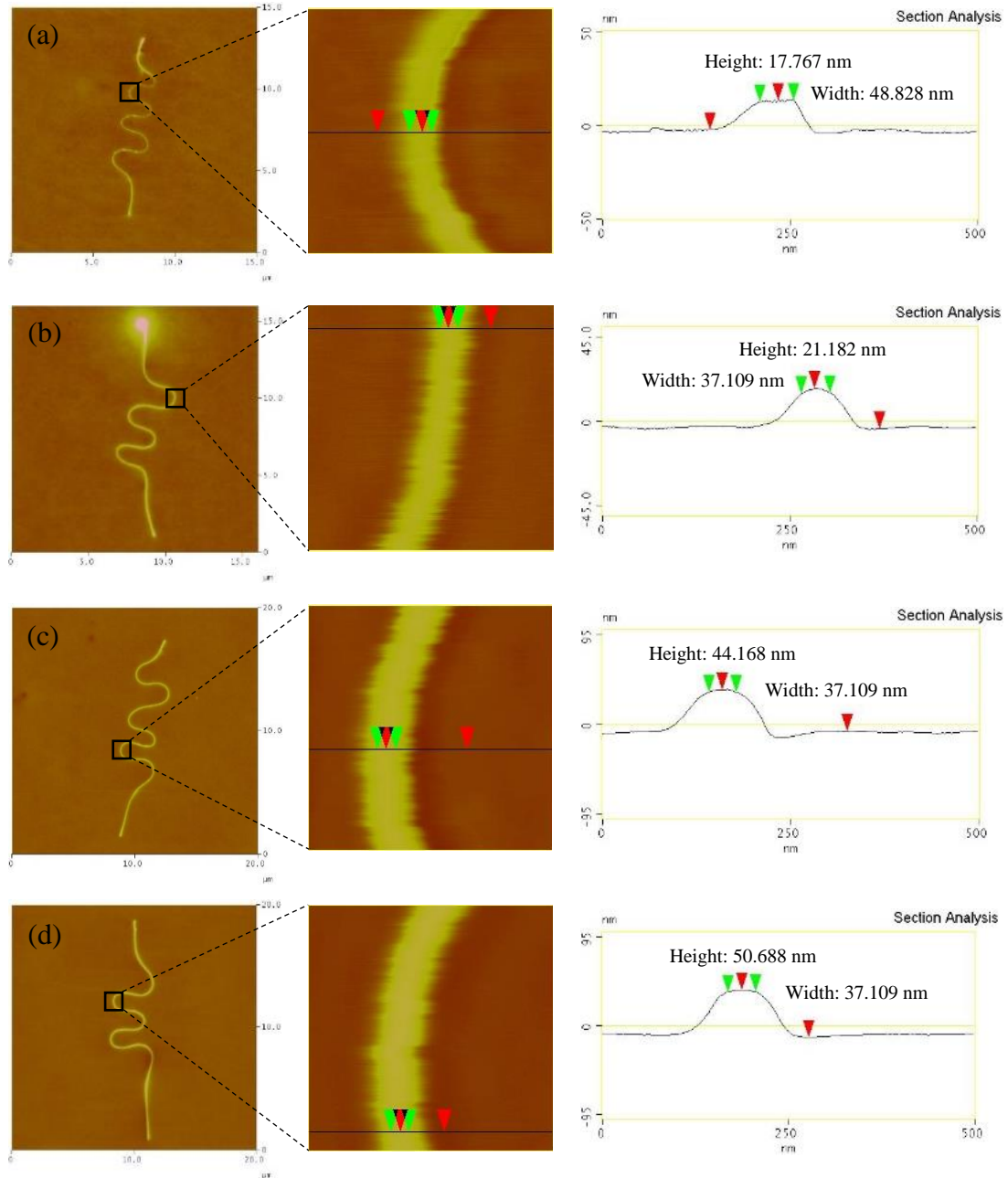


Figure 3.11: Height and width measurements at the buckle of wavy Si nanoribbons with aspect ratio (a) 1.19, (b) 1.68, (c) 2.18 and (d) 2.70.

Meanwhile, the AFM images of buckled Si nanoribbons with aspect ratio beyond 1.68 also reveal out-of-plane buckling mode due to the fact that the step height measured along the buckled ribbons approaches a value much greater than the height of the respective ribbon (of similar aspect ratio) laid flat on the PDMS substrate. Even though the line cuts on the right panel of Figure 3.10 (c-d) characterize a form of in-

surface topography profile, the step height measurements suggested that the ribbons essentially buckled out-of-plane with the ribbons being inclined from the substrate surface. Akin to the line cut profile across the buckle of ribbons with aspect ratio 1.68, the magnified scans at the buckle ribbons with aspect ratio of 2.18 and 2.70 (Figure 3.11 c-d) demonstrating a cross-section of an arch further affirmed this speculation. As for the ribbons with the largest aspect ratio of 5.12, the buckling mode is apparently out-of-plane in which a portion of the buckled ribbon becomes invisible in the optical image (Figure 3.9 e) as it is positioned away from the focus plane. This form of out-of-plane buckling is coined as normal-to-plane while the former one is considered as incline-to-plane. Figure 3.12 distinguishes the two forms of out-of-plane buckling mode discussed above.

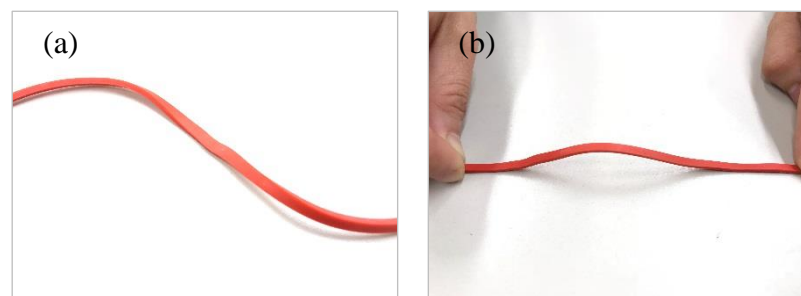


Figure 3.12: Two forms of out-of-plane buckling mode, (a) incline-to-plane buckling with an inclined bend at the buckle, (b) normal-to-plane buckling.

Noting that buckling would occur with respect to the direction having the least area moment of inertia¹⁷, for a structure having rectangular cross-section like ribbon, the area moment of inertia with respect to the lateral axis is lower than that of the horizontal axis. More specifically, the area moment of inertia for out-of-plane buckling mode is more favorable than its counterpart. Based on the results, it appears that a critical value of aspect ratio existed, below (above) which in-plane (out-of-plane)

buckling is favorable. In this work, the critical aspect ratio value is expected to range around $B/H \approx 1.19$, which is in close proximity to the value found in the literature. Duan *et al.* reported that both their analytical solution and FEA models exemplify that the transition of the buckling modes occurs at $B/H \approx 1.15$ for a stiff layer of rectangular cross-section when $\bar{E}_s/E_b = 1.9 \times 10^{-5}$ (*i.e.* $E_b = 140$ GPa, $E_s = 2$ MPa).^{35,43} Literature shows that in-plane buckling mode is favorable over its counterpart at $B/H < 1.15$ due to smaller critical buckling strain involved, and vice versa. A glimpse into the analytical solution for a rectangular structure having core-sheath morphology (detailed in Chapter 4) indicates that the critical buckling mode transition point for our materials system (in the range of $\bar{E}_s/E_b = 2.47$ to 2.65×10^{-5}) indeed follows $B/H \approx 1.14$. Thus, it is reasonable to expect ribbons with aspect ratio 1.119 buckle in-plane based on the close proximity to the analytical transition point 1.14.

On the other hand, the same group of researchers reported that incline-to-plane buckling is a transitional phase form in-plane to normal-to-plane buckling.⁴³ It is highlighted that structures having trapezoid cross-section with aspect ratio (B/H) between 1.54 and 2.38 are susceptible to incline-to-plane buckling upon the release of substrate pre-strain due to the asymmetrical characteristic of the structure. Additionally, the inclination of the buckled structure with respect to the normal direction of the substrate surface increases with the amount of pre-strain applied. It is reported that at $\bar{E}_s/E_b = 3.3 \times 10^{-4}$, structure with a trapezoid cross-section (having interior angles of 65° and 55°) buckles out-of-plane at an incline angle of approximately 27° from the normal direction of the substrate surface upon the relaxation of 4% pre-strain.⁴³ It appears that, in our work, ribbons with aspect ratio between 1.68 and 2.70 buckled incline-to-plane with an exceptionally large incline angle, most likely as a result of the application of 100% pre-strain and asymmetrical feature of the ribbons. The amount of pre-strain

reported in the literature (refer to Table 1.1) is typically limited to the linear elastic regime of the compliant substrate *i.e.* below 40%, as compared to 100% of pre-strain in this work. Moreover, though the lithography-patterned Si nanoribbons are reported to be of absolute rectangular cross-section⁷², the thickness of native oxide sheath layer surrounding Si core is not totally uniform, rendering the irregularity structure of the ribbons. These two factors are speculated to contribute to formation of incline-to-plane buckling mode of ribbons with aspect ratios ranging from 1.68 to 2.70. Additionally, within this regime $1.68 \leq B/H \leq 2.70$, we postulated that the following experimental conditions could frustrate the out-of-plane buckling mode, leading to the incline-to-plane buckling mode with an excessively large incline angle: (i) misalignment of ribbons from axial loading direction, and (ii) ribbons were not laid perfectly flat on substrate surface, which could result in poor interfacial adhesion and causes slippage. However, further investigation using FEA is warranted to understand the relation of aspect ratios on the ribbon buckling behavior under exceptionally large pre-strain.

Nonetheless, the buckling mode of ribbons with greatest aspect ratio 5.12 is absolutely normal-to-plane, regardless of the influence of symmetrical, pre-strain and alignment. Without any means of enhancing the interfacial properties, the buckling of these wide ribbons could be partially impossible and partially out-of-plane. Inability of the ribbon to buckle under the applied compressive strain implies that low friction force between the ribbons and substrate caused slippage. Therefore, the following section introduces the use of ultra-violet/ozone (UVO) surface treatment to improve the interfacial adhesion between the ribbons and substrate.

3.3 Effect of surface treatment on buckling of Si nanoribbons

As noted earlier, the surface treatment of the PDMS substrate by UVO prior to its contact with the Si nanoribbons is critical for the formation of a strong adhesive bond between the two constituents. With the increase of polar silanol groups ($-\text{Si}-\text{OH}$) at the expense of nonpolar methyl groups ($-\text{CH}_3$) during the UVO treatment, the treated PDMS surface becomes highly hydrophilic and capable of reacting with various inorganic surfaces to form strong siloxane ($\text{Si}-\text{O}-\text{Si}$) bonds through a condensation reaction.

3.3.1 Effect of aging on wettability of treated substrate

However, we found that the contact between the substrate and nanoribbons must be made promptly as the modifications induced by the UVO treatment are unstable due to hydrophobic recovery effect (as discussed in section 1.5.4), and their decay serves to limit the adhesive bond strength. As such, the water contact angle measurements was used to determine the surface treatment decay rate as the change of water contact angle is directly related to the concentration of surface hydrophilic functional groups. The contact angle measurement was performed immediately after 5 min of the intended treatment duration and followed by every subsequent 10 min. The measurement was not carried out immediately after the UVO treatment (*i.e.* at aging time of 0 min) due to experimental limitations. Figure 3.13 plotted the water contact angle as a function of UVO treatment aging time after 90 s and 150 s of treatment duration.

The contact angle of the pristine PDMS substrate (prepared from a mixture of base and curing agent at a ratio of 10:1 ratio and cured at RT for 48 hr) was measured at $120.56 \pm 1.57^\circ$, which is in accordance to the values reported in the literatures^{48,49,51}.

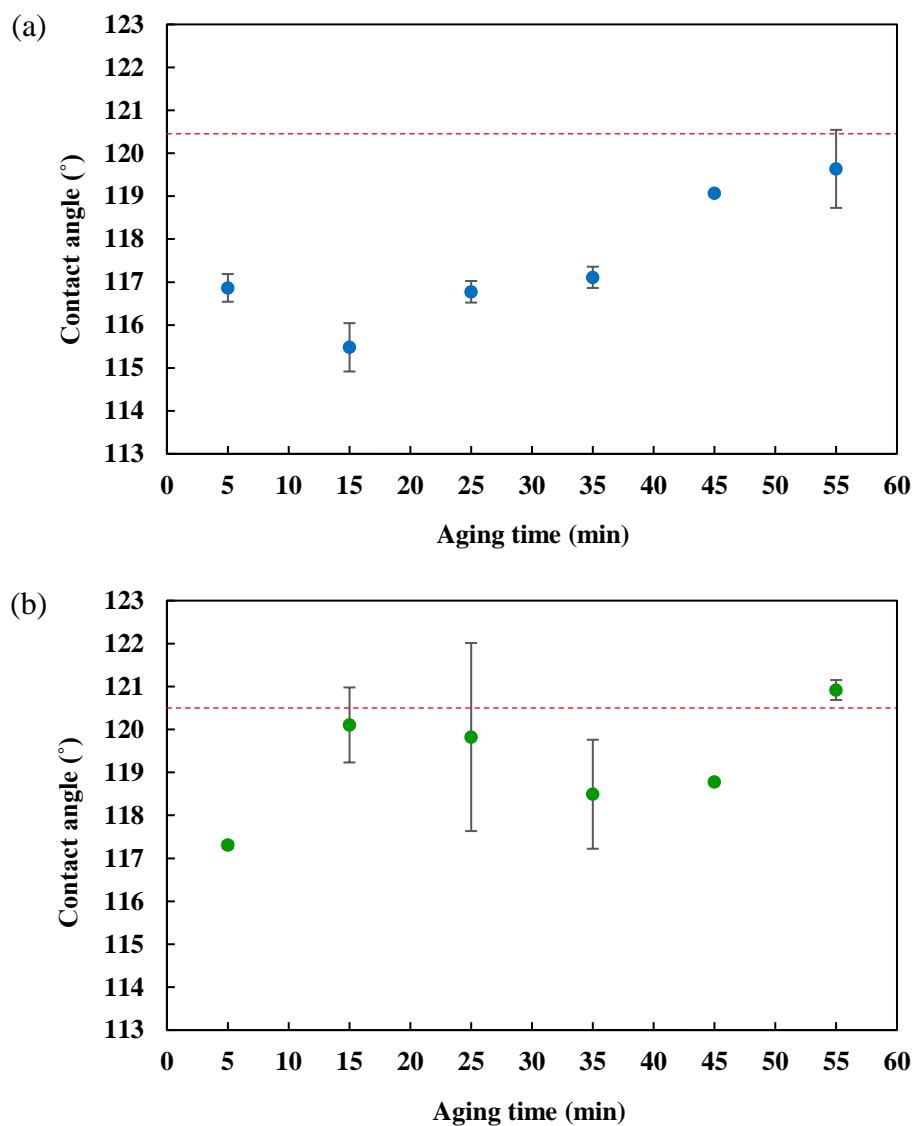


Figure 3.13: Water contact angle as a function of UVO treatment aging time at (a) 90 s and (b) 150 s treatment duration. The red dotted line indicates that water contact angle of pristine PDMS surface.

At the aging time of 5 min, the contact angle of the UVO-treated substrates was approximated at 117° for both 90 s and 150 s treatment duration. Decrease of contact angle implies an improvement on the surface wettability of the treated substrate due to the presence of surface hydrophilic functional groups, and thus the interfacial properties between the substrate and ribbon could be enhanced through the formation of chemical bonding (i.e. siloxane bonds), as explained in section 1.5.3. This observation also

confirms that UVO treatment is an aggressive one, such that the substrate surface could be modified within a short exposure time. However, it must be noted that this form of surface modification effect is only temporary and can be lost with time, in addition to limited occurrence at the surface and near-surface regions of the PDMS but not the bulk.^{46,48,49,73}

While the 90 s-treated substrate demonstrated contact angle of $115.5 \pm 0.56^\circ$ at 15 min of aging time following UVO exposure, a high $120.1 \pm 0.87^\circ$ was observed for that of 150 s-treated substrate and further aging caused deterioration of the surface hydrophilicity of the substrate. In fact, the water contact angle exhibited increasing trend as the post-treatment time elapsed gradually. Increased contact angle is indicative of reduction of surface hydrophilic groups on the substrate, and it was therefore evidenced that hydrophobic recovery took place on the UVO-treated substrates over time. It has been established that the hydrophobic recovery is due to the migration of lower molecular weight (LMW) species escaping from the bulk to the surface.^{47,48,59,60}

In order to warrant good adhesion at the interface, the transfer of Si nanoribbon onto the substrate surface must be accomplished within 15 min following the UVO exposure, regardless of the treatment duration. According to Figure 3.13, the contact angle of the treated substrate has nearly regained the wettability of the pristine PDMS at the aging duration of 15 min, suggesting that the surface hydrophobic recovery of the PDMS has become pronounced, and with that said the chemical bonding between the two constituents would be unlikely to take place beyond that point. Meanwhile, knowing that the formation of siloxane bonds is not immediate upon contact, ribbon alignment error could be corrected and the bonding was allowed to take place for approximately 10 min thereafter.

3.3.2 Buckling wavelength as a function of surface treatment

The effect of UVO surface treatment duration on the buckling wavelength is also elucidated in Figure 3.14. A better representation of the treatment effect on the wavelength for each group of ribbons is individually presented in Figure 3.15. Generally, there exists an overall trend of lower buckling wavelength for a longer treatment duration, and the decrease in the wavelength can be attributed to the change of the surface properties of the UVO-treated substrate.

UVO surface treatment is a form of photosensitized oxidation process and its treatment on PDMS has been widely studied, and thus the mechanism of surface modification is also well-established.^{45-47,50,54,56,63,73} Several literature have demonstrated that the UVO surface treatment resulted in the enhancement of the PDMS surface modulus due to the formation of a continuous thin silica-like layer (SiO_x) on the treated surface, as supported by X-ray photoelectron spectroscopy (XPS) studies^{46,54,74}. During the treatment, the UV irradiation at 185 nm converts the atmospheric molecular oxygen to ozone and the subsequent UV irradiation at 254 nm further transforms the ozone into atomic oxygen.^{46,63,73} Atomic oxygen later reacts with surface polymer chains to remove the methyl ($-\text{CH}_3$) groups with concurrent formation of silanol ($-\text{Si}-\text{OH}$) groups. Consequently, this leads to the surface properties of the polymer approaching that of the silicon oxide over time.^{45-47,50,54,56,63,73}

Owing to the increase of substrate surface modulus with the treatment duration^{54,63}, the buckling wavelength of a specified size group of the Si nanoribbons decreased in the similar fashion, as suggested by Eq. (3.8). While there existed a general trend of lower buckling wavelength for a longer treatment duration, the reduction seemed to be insignificant. This is because the change of substrate modulus was only limited to the surface regime within tens of nanometers^{47,50,54}, rendering the substrate

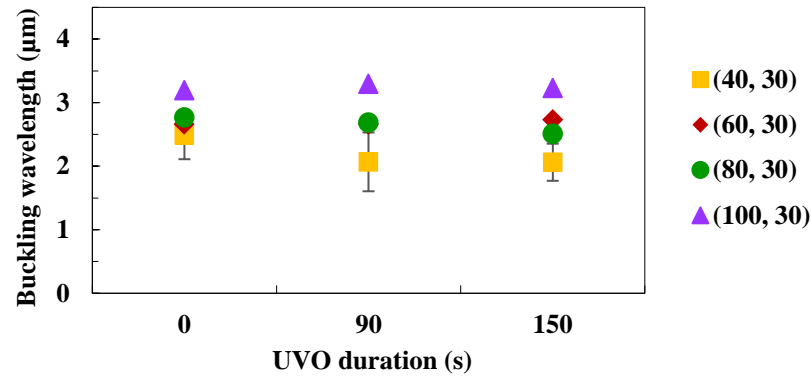


Figure 3.14: Influence of UVO treatment duration on the buckling wavelength of Si nanoribbons having various aspect ratios. The ribbons are denoted as (B, H) where B is the width and H is the thickness.

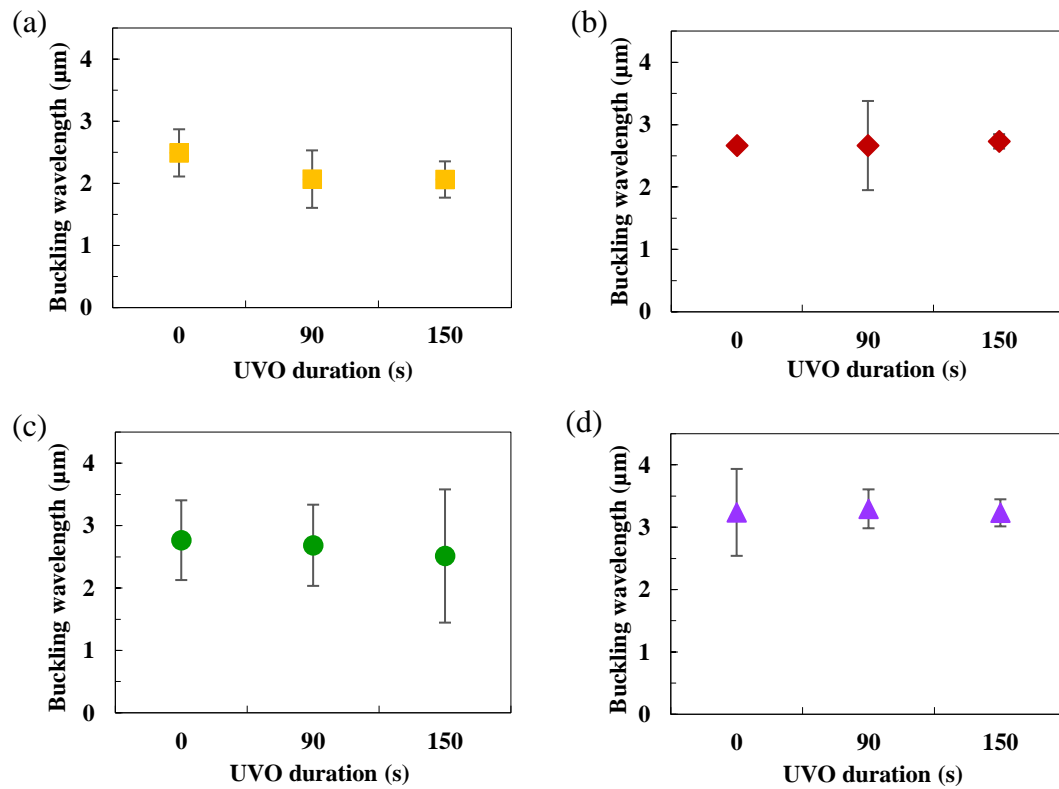


Figure 3.15: Influence of UVO treatment duration on the buckling wavelength of Si nanoribbons of constant thickness of 30 nm but different width of (a) 40 nm, (b) 60 nm, (c) 80 nm and (d) 100 nm.

bulk modulus unaffected. Xu *et al.* also reported the similar phenomenon such that the buckling wavelength of silicon nanowires remains almost unchanged with increase of the UVO treatment time, but buckling mode does vary.⁴⁴ As such, the effect of UVO treatment on the ribbon buckling wavelength was negligible in this context while its effect on buckling mode would be nontrivial.

3.3.3 Buckling mode as a function of surface treatment

As discussed in section 3.2.3, there are three variants of buckling mode observed in this work. While ribbons with aspect ratio 1.19 buckled in-plane, ribbons with greater aspect ratios buckled out-of-plane where incline- and normal-to-plane buckling were perceived on ribbons having aspect ratio $1.68 \leq B/H \leq 2.70$ and $B/H > 2.70$, respectively. Despite the geometrical effect, several literature suggested that the buckling mode is also a function of the interfacial adhesion between the two constituents.^{17,44,58} Adhesion at the ribbon/substrate interface can be controlled through the surface properties of the substrate. In this work, modification of the surface properties of the substrate was performed through ultra-violet/ozone (UVO) treatment with varying treatment duration. As discussed earlier, increase of substrate surface wettability following the treatment infers that the substrate surface was masked with highly polar chemical moieties, namely silanol ($-\text{Si}-\text{OH}$), which warrants enhanced interfacial adhesion between substrate and ribbon in contact.

Through condensation, silanol groups on the oxidized PDMS surface interacted with oxide sheath layer on the silicon nanoribbon to form strong covalent chemical bonds (*i.e.* siloxane bonds, $-\text{Si}-\text{O}-\text{Si}-$), on top of the existing weak van der Waals force upon contact at room temperature.^{45,55,56} These chemical bonds were so strong that any attempts to remove the ribbons from the oxidized PDMS surface resulted in

fracture of the ribbons during manipulation. Similar phenomenon has also been observed by Sun and Rogers whereby removal of Si ribbons from UVO-treated PDMS surface caused cohesive mechanical failure of the substrate instead of adhesive rupture at the interface.⁴⁵ In fact, Qin and Zhu characterized the static friction force between Si nanowires and PDMS substrate and found that the friction force rose approximately three-fold when the substrate was UVO-treated for a short 5 minutes.⁵²

Table 3.6 summarizes the effect of UVO surface treatment duration on the buckling mode of Si nanoribbons of variable aspect ratios and the respective optical images are supplemented in Figure 3.16. Broadly, the buckling mode of the ribbons have not considerably changed with respect to the effect of substrate surface treatment. For ribbons of ribbons with aspect ratio between 1.19 and 2.18, UVO treatment did not lead to any modification in the inherent buckling mode. However, the effect of substrate surface treatment was apparent on ribbons with greater aspect ratios of 2.70 and 5.12. When the UVO treatment duration increased to 150 s, both variants of out-of-plane buckling mode were observed on ribbons with aspect ratio 2.70, with majority still retained the incline-to-plane buckling mode. Meanwhile, it is interesting to note that ribbons with largest aspect ratio 5.12 were all able to buckle in the normal-to-plane mode when UVO treatment was applied to the substrate. These two phenomena imply that UVO treatment is indeed an effective method to enhance the interfacial adhesion, such that normal-to-plane buckling mode becomes more likely; however, it is also acknowledged that the interfacial contact area is another paramount factor in determining the adhesion properties.

Based on the literatures, transition of the buckling mode from 2D in-plane wavy buckling to 3D coil-like buckling have been observed by Xu *et al.* on a SiNW-PDMS system by means of regulating the UVO treatment duration of the pre-strained PDMS

Table 3.6: Effect of treatment duration on the buckling mode of Si nanoribbons of various aspect ratios under 100% pre-strain.

Treatment duration (s)	Ribbon aspect ratio (B/H) Nanoribbon convention (width B , height H)				
	$B/H = 1.19$ (40, 30)	$B/H = 1.68$ (60, 30)	$B/H = 2.18$ (80, 30)	$B/H = 2.70$ (100, 30)	$B/H = 5.12$ (200, 30)
0	In-plane	Incline-to-plane	Incline-to-plane	Incline-to-plane	None or Normal-to-plane
90	In-plane	Incline-to-plane	Incline-to-plane	Incline-to-plane	Normal-to-plane
150	In-plane	Incline-to-plane	Incline-to-plane	Incline-* or Normal-to-plane	Normal-to-plane

**Note: Buckling mode which is more dominant, with 61.5% probability based on thirteen sets of test.*

substrates.⁴⁴ Silicon nanowires having diameter of 30 ± 5 nm were found to transform from in-plane buckling to helical coil buckling as the UVO treatment time increased from 0 to 8 min. The later FEM studies suggested that partial debonding is the reason for the buckling mode transition.⁵⁸ It is also worth-noting that helical buckling is, in practice, most likely to appear on structures with equal moment of inertia in all directions, *e.g.* circular or hexagon cross-section.¹⁷ As such, this explains our condition whereby transformation of in-plane to out-of-plane buckling mode has not been encountered throughout the course of this work.

Nevertheless, it is interesting to note the effect of UVO treatment on the buckling profile of the ribbons observed using tapping mode AFM. We noticed that the surface condition of the substrate which was in contact with the ribbons changed as the UVO treatment duration increased to 150 s. Based on Figure 3.17, the substrate region underneath the ribbon peaks/valleys are found to appear darker than other regions. It is known that AFM images are typically color-coded by surface topographic features, with dark colors code for low-lying regions and bright colors represent higher elevation.

Thus, it is apparent that those dark regions corresponded to surface depression on the substrate, which is observed in the corresponding 3D surface plot images on the right panel of Figure 3.17. In addition, the peaks/valleys of the buckled ribbons are also seen to appear brighter in the plane-view images, suggesting that the particular regions were slightly rose to higher elevation than the rest. These findings signify improved contact between ribbon and substrate as a result of substrate surface treatment. It is noted that such features are only found in substrate treated for 150 s.

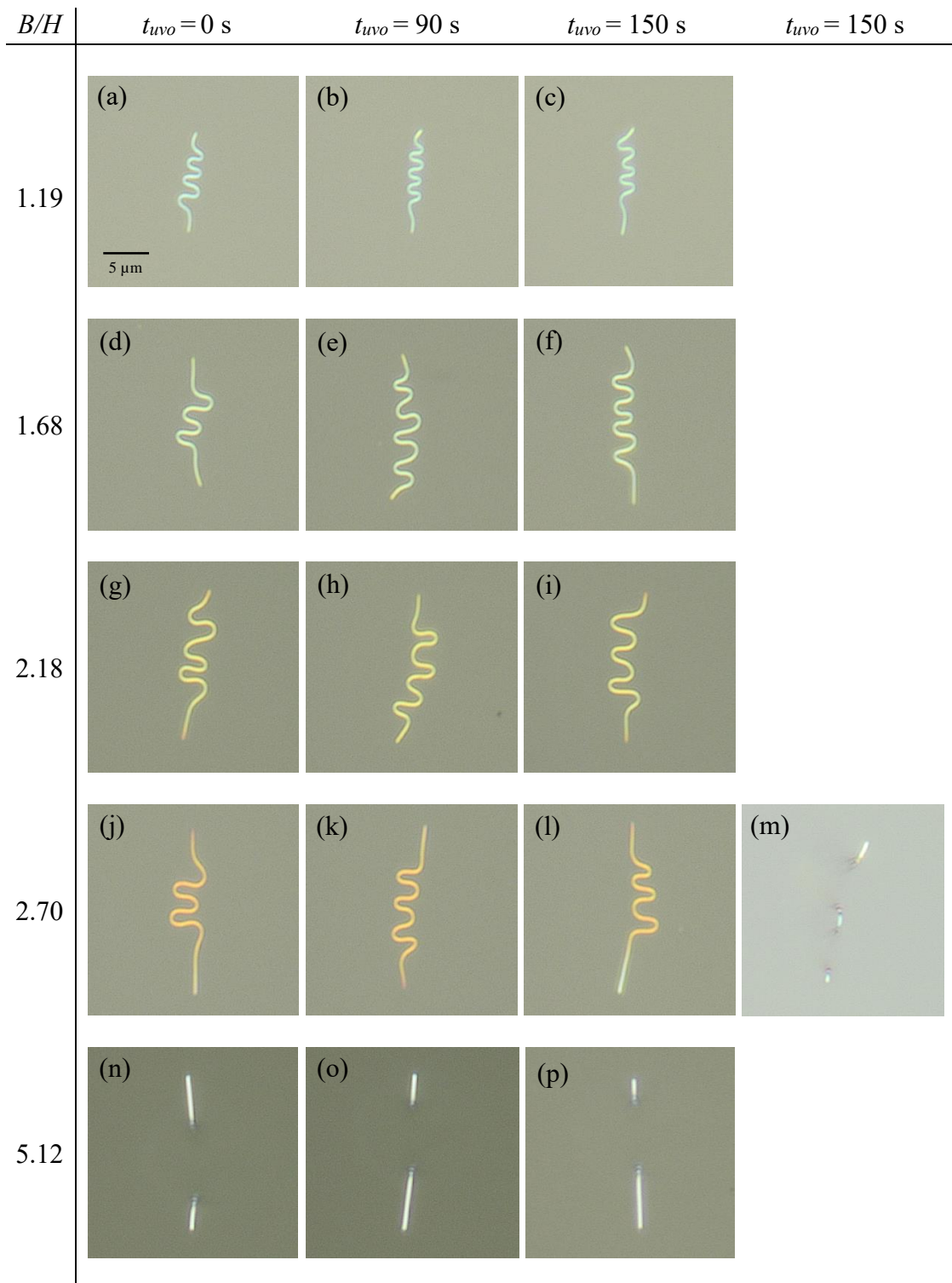


Figure 3.16: Buckling mode of Si nanoribbons of different aspect ratio (B/H) as a function of UVO treatment duration t_{uvo} . While all ribbons demonstrated a single buckling mode for the specified treatment duration, ribbons of $B/H = 2.70$ buckled in two modes, (l) in-plane as well as (m) out-of-plane at $t_{uvo} = 150$ s. Scale bar in (a) is applicable to all images.

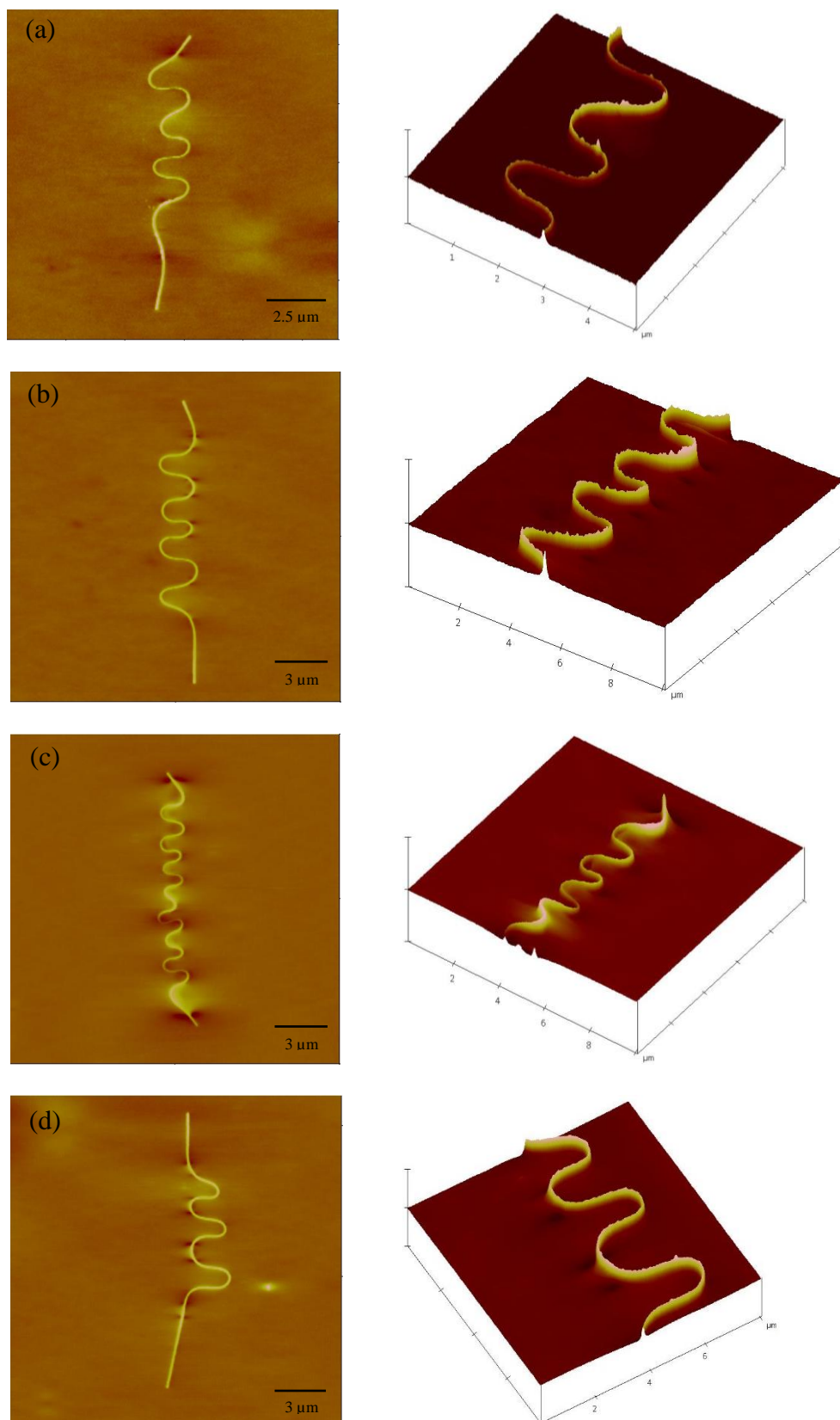


Figure 3.17: Plane-view AFM images of wavy Si nanoribbons with aspect ratio of (a) 1.19, (b) 1.68, (c) 2.18 and (d) 2.70 on 150 s-treated PDMS substrate. The right panel illustrates the respective 3D surface plot of the buckled ribbon.

CHAPTER 4: MECHANICS OF BUCKLED NANORIBBON ON A COMPLIANT SUBSTRATE

The buckling mechanics of a stiff nanostructure on a flexible substrate has been extensively studied by several research groups^{12-17,35,43,58} and the underlying physics is well-described using the least energy principle. Regardless of the buckling mode, the total energy of the buckling system consists of three main components, namely the bending energy of the nanoribbon due to buckling U_b , membrane energy of the nanoribbon U_m , and strain energy of the compliant substrate U_s . In order to distinguish the two buckling modes, subscript 1 and 2 are used to refer to the in-plane and out-of-plane deformation, respectively. In this chapter, the total system energies of the two variants are discussed thoroughly in the following sections in reference to the literature^{12-17,35,43,58}.

4.1 In-plane buckling mechanism

4.1.1 Nanoribbon

In the theoretical model, the nanoribbon is regarded as a stiff beam having a rectangular cross-sectional area A , Young's modulus E_b and moment of inertia I_b . The bending and tension stiffness of the beam on the surface of the compliant substrate are denoted by $E_b I_b$ and $E_b A$, respectively. Based on experimental observation, the Si nanoribbons (SiNR) buckle in a sinusoidal form and the lateral deflection can be described as $v = a \cos kx$ where the coordinate x refers to the axial direction of the

SiNR, a is the buckling amplitude and k is the wavevector. The wavevector k is related to the buckling wavelength λ by $k = 2\pi/\lambda$.

For in-plane buckling system with the in-plane (lateral) deflection denoted as $v_1 = a_1 \cos k_1 x$, the bending energy (per unit wavelength) in the beam is

$$U_{b1} = \frac{k_1}{2\pi} \int_0^{2\pi/k_1} \frac{1}{2} E_b I_{b1} (v_1'')^2 dx = \frac{E_b I_{b1}}{4} k_1^4 a_1^2. \quad (4.1)$$

Since the SiNR has a rectangular cross-section, area moment of inertia takes $I_{b1} = B^3 H/12$. The membrane strain in the beam is expressed in terms of axial displacement u and lateral deflection v by

$$\varepsilon_m = u' + (v')^2/2. \quad (4.2)$$

Due to the fact that the Young's modulus of the beam (*i.e.* ~ 170 GPa for SiNR) is much greater than that of the substrate (*i.e.* ~ 2 MPa for PDMS), the shear stress at the beam/substrate interface becomes negligible⁷⁵, leading to a constant membrane force (and therefore, constant membrane strain ε_m) in the buckled beam. Hence,

$$\frac{d\varepsilon_m}{dx} = \frac{d^2 u}{dx^2} + \frac{dv}{dx} \frac{d^2 v}{dx^2} = 0. \quad (4.3)$$

Substituting the in-plane deflection of the beam into the Eq. (4.3) gives the axial displacement

$$u_1 = \frac{k_1 a_1^2 \sin(2k_1 x)}{8} - \varepsilon_{pre} x, \quad (4.4)$$

where $-\varepsilon_{pre}$ is the compressive strain in the beam due to the relaxation of pre-strain applied to the substrate. The membrane strain for in-plane buckling system is, thus, expressed as

$$\varepsilon_{m1} = \frac{k_1^2 a_1^2}{4} - \varepsilon_{pre}. \quad (4.5)$$

The membrane energy (per unit wavelength) in the beam is

$$U_{m1} = \frac{k_1}{2\pi} \int_0^{2\pi/k_1} \frac{1}{2} E_b A \varepsilon_{m1}^2 dx = \frac{E_b A}{2} \left(\frac{k_1^2 a_1^2}{4} - \varepsilon_{pre} \right)^2. \quad (4.6)$$

The linear elastic constitutive models gives the axial force

$$F = E_b A \varepsilon_{m1}. \quad (4.7)$$

Based on the beam theory, the lateral force (per unit wavelength) on the beam due to buckling can be derived from the in-plane deflection v_1 and axial force F of the beam as

$$T_1 = E_b I_{b1} \frac{d^4 v_1}{dx^4} - F \frac{d^2 v_1}{dx^2} = -P_1 \cos k_1 x, \quad (4.8)$$

where

$$P_1 = -E_b I_{b1} a_1 k_1^4 - E_b A a_1 k_1^2 \left(\frac{k_1^2 a_1^2}{4} - \varepsilon_{pre} \right). \quad (4.9)$$

4.1.2 Substrate

The compliant substrate is modeled as a semi-infinite solid because its thickness (~ 2 mm) is several orders of magnitude larger than the buckling wavelength of the beam. Let E_s denote Young's modulus of the poly(dimethylsiloxane) (PDMS) substrate and ν_s as its Poisson's ratio ($\nu_s \approx 0.5$). While the substrate surface is traction-free, the region underneath the beam, with a width of B along the x direction, is subjected to lateral stress traction as a result of beam buckling. The lateral stress traction in this region is the average of the lateral force $P_1 \cos k_1 x$ over the width, namely $P_1 \cos k_1 x / B$. Using the Green's function method, for a point (x, y) on the substrate

surface, the lateral displacement (along the y direction) induced by a unit lateral point force (also along the y direction) at (ξ, ψ) on the substrate surface is given by

$$v_1 = \frac{(1 - \nu_s)(x - \xi)^2 + (y - \psi)^2}{\pi \bar{E}_s (1 - \nu_s) [(x - \xi)^2 + (y - \psi)^2]^{3/2}}, \quad (4.10)$$

where $\bar{E}_s = E_s / (1 - \nu_s^2)$ is the plane-strain modulus of the substrate. The lateral displacement (along the y direction) on the surface for the average lateral force $P_1 \cos k_1 x / B$ over the width B can be obtained by integrating the Eq. (4.10) as

$$v_{sub1} = \frac{P_1 \cos k_1 x}{\pi \bar{E}_s (B/2)} \int_{-\frac{B}{2}}^{\frac{B}{2}} \frac{(1 - \nu_s) K_0(k_1 |y - \psi|) + \nu_s k_1 |y - \psi| K_1(k_1 |y - \psi|)}{(1 - \nu_s)} d\psi \quad (4.11)$$

where K_0 and K_1 are modified Bessel functions of the second kind. For the buckling wavelength larger than the width ($kB/2 < 1$), the modified Bessel functions can be approximated by their asymptotic expansions, $K_0(k_1 |y - \psi|) \approx -\ln(k_1 |y - \psi|/2) - \gamma$ and $K_1(k_1 |y - \psi|) = 1/(k_1 |y - \psi|)$ where $\gamma = 0.577$ is Euler's constant. As such, the leading term in the Taylor series expansion in Eq. (4.11) is

$$v_{sub1} = \frac{P_1 \cos k_1 x}{\pi \bar{E}_s (B/2)} \left\{ B \left(\frac{1}{1 - \nu_s} - \gamma + \ln 2 \right) - \left(\frac{B}{2} + y \right) \ln \left(k_1 \left| \frac{B}{2} + y \right| \right) - \left(\frac{B}{2} - y \right) \ln \left(k_1 \left| \frac{B}{2} - y \right| \right) \right\}. \quad (4.12)$$

The strain energy (per unit wavelength) in the substrate can be obtained in terms of the lateral stress traction $P_1 \cos k_1 x / B$ and surface displacement in the Eq. (4.12) via the divergence theorem as

$$\begin{aligned} U_{s1} &= \frac{k_1}{2\pi} \int_V \frac{1}{2} \sigma_{ij} \varepsilon_{ij} dV \\ &= \frac{k_1}{2\pi} \int_0^{\frac{2\pi}{k_1}} \int_{-\frac{B}{2}}^{\frac{B}{2}} \frac{1}{2} \frac{P_1 \cos k_1 x}{B} v_{sub1} dy dx \end{aligned}$$

$$= \frac{P_1^2}{4\pi\bar{E}_s} \left\{ \frac{3 - \nu_s}{1 - \nu_s} - 2\gamma - 2 \ln \left(\frac{k_1 B}{2} \right) \right\}. \quad (4.13)$$

4.1.3 Potential energy

Therefore, the total potential energy (per unit wavelength) of the in-plane buckling system can be obtained as

$$\begin{aligned} U_{tot1} &= U_{b1} + U_{m1} + U_{s1} \\ &= -\frac{k_1}{2\pi} \int_0^{\frac{2\pi}{k_1}} \int_{-\frac{B}{2}}^{\frac{B}{2}} \frac{P_1 \cos k_1 x}{B} (v_{sub1} - a_1 \cos k_1 x) dy dx \\ &= -\frac{E_b I_{b1}}{4} k_1^4 a_1^2 + \frac{E_b A}{2} \left(\varepsilon_{pre} - \frac{k_1^2 a_1^2}{4} \right) \left(\varepsilon_{pre} + \frac{3 k_1^2 a_1^2}{4} \right) \\ &\quad - \frac{P_1^2}{4\pi\bar{E}_s} \left\{ \frac{3 - \nu_s}{1 - \nu_s} - 2\gamma - 2 \ln \left(\frac{k_1 B}{2} \right) \right\}, \end{aligned} \quad (4.14)$$

where the last integral term represents the work across the beam/substrate interface.

The minimization of U_{tot1} with respect to the in-plane buckling amplitude a_1 ,

$\partial U_{tot1} / \partial a_1 = 0$, gives

$$a_1 = \begin{cases} \frac{2}{k_1} \sqrt{\varepsilon_{pre} - \varepsilon_{c1}}, & \varepsilon_{pre} > \varepsilon_{c1}, \\ 0, & \varepsilon_{pre} \leq \varepsilon_{c1}, \end{cases} \quad (4.15)$$

where

$$\varepsilon_{c1} = \frac{1}{E_b A k_1^2} \left\{ E_b I_{b1} k_1^4 + \frac{\pi \bar{E}_s}{\frac{3 - \nu_s}{1 - \nu_s} - 2\gamma - 2 \ln \left(\frac{k_1 B}{2} \right)} \right\}. \quad (4.16)$$

Eq. (4.15) suggests that in-plane buckling occurs only when the pre-strain reaches a critical value given by Eq. (4.16) where ε_{c1} is termed as the in-plane critical buckling strain of a stiff beam on a compliant substrate. It is also noted that the buckling amplitude increases with the pre-strain.

Meanwhile, the minimization of potential energy with respect to the wavenumber k_1 , $\partial U_{tot1}/\partial k_1 = 0$, gives

$$\left(\frac{E_b I_{b1}}{\bar{E}_s}\right)^{1/4} k_1 = \left[\frac{2\pi \left(\frac{1}{1-\nu_s} - \gamma - \ln\left(\frac{k_1 B}{2}\right) \right)}{\left(\frac{3-\nu_s}{1-\nu_s} - 2\gamma - 2 \ln\left(\frac{k_1 B}{2}\right) \right)^2} \right]^{1/4}. \quad (4.17)$$

Substituting the Eq. (4.15) and (4.16) into Eq. (4.14), the total potential energy (per unit wavelength) of the in-plane buckling system can be simplified as

$$U_{tot1} = \frac{1}{2} E_b A \varepsilon_{c1} (2\varepsilon_{pre} - \varepsilon_{c1}). \quad (4.18)$$

Based on the principle of least energy, buckling mode of the system with lower total potential energy is energetically favorable. A close examination on Eq. (4.18) shows that the critical buckling strain ε_{c1} is the defining parameter of the total potential energy of a buckled system with constant material properties and amount of pre-strain.³⁵

4.1.4 Approximation of in-plane buckling strain

Based on the literature¹², the right side of Eq. (4.17) takes a constant of 5/7, the critical buckling strain for in-plane buckling mode ε_{c1} is then approximated to

$$\varepsilon_{c1} = \frac{B^2}{A} \sqrt{\frac{\bar{E}_s}{E_b}} \sqrt{\frac{I_{b1}}{B^4}} \left(\frac{1}{2} + \frac{2\pi}{5 - 2\gamma - 2 \ln \frac{5}{7} + 2 \ln 2 - \frac{1}{2} \ln \frac{\bar{E}_s}{E_b} + \frac{1}{2} \ln \frac{I_{b1}}{B^4}} \right) \quad (4.19)$$

Knowing that, for a beam with rectangular cross-section, the area moment of inertia with respect to y-axis is given as $I_{b1} = B^3 H / 12$, ε_{c1} can then be re-written as

$$\varepsilon_{c1} = \sqrt{\frac{1}{12}} \cdot \sqrt{\frac{\bar{E}_s}{E_b}} \cdot \sqrt{\frac{B}{H}} \left(\frac{1}{2} + \frac{2\pi}{5 - 2\gamma - 2 \ln \frac{3}{4} + \frac{1}{2} \ln \frac{4}{3} - \frac{1}{2} \ln \frac{\bar{E}_s}{E_b} - \frac{1}{2} \ln \frac{B}{H}} \right) \quad (4.20)$$

4.2 Out-of-plane buckling mechanism

4.2.1 Nanoribbon

For the out-of-plane buckling system, the derivation of both the bending and membrane energy of the nanoribbon remains similar to that of the in-plane buckling system. Hence, the bending energy (per unit wavelength) of the beam in the out-of-plane buckling system is

$$U_{b2} = \frac{k_2}{2\pi} \int_0^{2\pi/k_2} \frac{1}{2} E_b I_{b2} (v_2'')^2 dx = \frac{E_b I_{b2}}{4} k_2^4 a_2^2 \quad (4.21)$$

and the respective membrane energy (per unit wavelength) takes the following form

$$U_{m2} = \frac{k_2}{2\pi} \int_0^{2\pi/k_2} \frac{1}{2} E_b A \varepsilon_{m2}^2 dx = \frac{E_b A}{2} \left(\frac{k_2^2 a_2^2}{4} - \varepsilon_{pre} \right)^2. \quad (4.22)$$

It is noted that the area moment of inertia takes $I_{b2} = BH^3/12$ in out-of-plane direction.

4.2.2 Substrate

However, the strain energy in the substrate differs from that of the in-plane buckling system due to the presence of normal force in the out-of-plane buckling system instead of the lateral force. The normal force (per unit wavelength) takes the form of

$$T_2 = E_b I_{b2} \frac{d^4 v_2}{dx^4} - F \frac{d^2 v_2}{dx^2} = -P_2 \cos k_2 x, \quad (4.23)$$

where

$$P_2 = -E_b I_{b2} a_2 k_2^4 - E_b A a_2 k_2^2 \left(\frac{k_2^2 a_2^2}{4} - \varepsilon_{pre} \right). \quad (4.24)$$

Like the lateral stress traction in the in-plane buckling system, the normal stress traction is the average of normal force $P_2 \cos k_2 x$ over the width, *i.e.* $P_2 \cos k_2 x / B$. Owing to the presence of the normal force, the Green's function for a unit normal point force at (χ, φ) on the substrate surface gives the normal displacement at (x, y) on the surface as

$$v_2 = \frac{1}{\pi \bar{E}_s [(x - \chi)^2 + (y - \varphi)^2]^{1/2}}. \quad (4.25)$$

By integrating the Eq. (4.25), the normal displacement for the normal stress traction $P_2 \cos k_2 x / B$ over the width B can be obtained as

$$v_{sub2} = \frac{P_2 \cos k_2 x}{\pi \bar{E}_s (B/2)} \int_{-B/2}^{B/2} K_0(k_2 |y - \varphi|) d\varphi, \quad (4.26)$$

where $K_0(k_2 |y - \varphi|)$ is the modified Bessel function of the second kind. As $(kB/2 < 1)$, the leading term in the Taylor series expansion in Eq. (4.26) is

$$v_{sub2} = \frac{P_2 \cos k_2 x}{\pi \bar{E}_s (B/2)} \left\{ B(1 - \gamma + \ln 2) - \left(\frac{B}{2} + y \right) \ln \left(k_2 \left| \frac{B}{2} + y \right| \right) - \left(\frac{B}{2} - y \right) \ln \left(k_2 \left| \frac{B}{2} - y \right| \right) \right\}. \quad (4.27)$$

The strain energy (per unit wavelength) in the substrate can be obtained via the divergence theorem as

$$U_{s2} = \frac{P_2^2}{4\pi \bar{E}_s} \left\{ 3 - 2\gamma - 2 \ln \left(\frac{k_2 B}{2} \right) \right\}. \quad (4.28)$$

4.2.3 Potential energy

The total potential energy (per unit wavelength) of the out-of-plane buckling system can be obtained as

$$\begin{aligned}
 U_{tot2} &= U_{b2} + U_{m2} + U_{s2} \\
 &= -\frac{k_2}{2\pi} \int_0^{\frac{2\pi}{k_2}} \int_{-\frac{B}{2}}^{\frac{B}{2}} \frac{P_2 \cos k_2 x}{B} (u_{sub2} - a_2 \cos k_2 x) dy dx \\
 &= -\frac{E_b I_{b2}}{4} k_2^4 a_2^2 + \frac{E_b A}{2} \left(\varepsilon_{pre} - \frac{k_2^2 a_2^2}{4} \right) \left(\varepsilon_{pre} + \frac{3 k_2^2 a_2^2}{4} \right) \\
 &\quad - \frac{P_2^2}{4\pi \bar{E}_s} \left\{ 3 - 2\gamma - 2 \ln \left(\frac{k_2 B}{2} \right) \right\}, \tag{4.29}
 \end{aligned}$$

where the last integral term represents the work across the beam/substrate interface.

Minimizing U_{tot2} with respect to the in-plane buckling amplitude a_2 , $\partial U_{tot2} / \partial a_2 = 0$, gives

$$a_2 = \begin{cases} \frac{2}{k_2} \sqrt{\varepsilon_{pre} - \varepsilon_{c2}}, & \varepsilon_{pre} > \varepsilon_{c2}, \\ 0, & \varepsilon_{pre} \leq \varepsilon_{c2}, \end{cases} \tag{4.30}$$

where ε_{c2} is termed as the out-of-plane critical buckling strain

$$\varepsilon_{c2} = \frac{1}{E_b A k_2^2} \left\{ E_b I_{b2} k_2^4 + \frac{\pi \bar{E}_s}{3 - 2\gamma - 2 \ln \left(\frac{k_2 B}{2} \right)} \right\}. \tag{4.31}$$

Meanwhile, the minimization of potential energy with respect to the wavenumber k_2 ,

$\partial U_{tot2} / \partial k_2 = 0$, gives

$$\left(\frac{E_b I_{b2}}{\bar{E}_s} \right)^{1/4} k_2 = \left[\frac{2\pi \left(1 - \gamma - \ln \left(\frac{k_2 B}{2} \right) \right)}{\left(3 - 2\gamma - 2 \ln \left(\frac{k_2 B}{2} \right) \right)^2} \right]^{1/4}. \tag{4.32}$$

The total potential energy (per unit wavelength) of the out-of-plane buckling system can then be simplified as

$$U_{tot2} = \frac{1}{2} E_b A \varepsilon_{c2} (2\varepsilon_{pre} - \varepsilon_{c2}). \quad (4.33)$$

Similarly, the out-of-plane buckling system shows a dependency on the critical buckling strain ε_{c2} as the determining parameter of its total potential energy. Hence, this facilitates the comparison of the total system energies between both in-plane and out-of-plane buckling systems by considering only the respective critical buckling strain ε_c .

4.2.4 Approximation of out-of-plane buckling strain

Literature¹⁵ suggested that the right side of Eq. (4.32) takes a constant of 3/4 based on the out-of-plane buckling of SWCNT on the elastomeric substrate. It is because both logarithmic and one-fourth power functions change very slowly with $k_2 B/2$, and essentially approaches the constant value. From there, the critical buckling strain for out-of-plane buckling mode ε_{c2} can be approximated to

$$\varepsilon_{c2} = \frac{B^2}{A} \sqrt{\frac{\bar{E}_s}{E_b}} \sqrt{\frac{I_{b2}}{B^4}} \left(\frac{9}{16} + \frac{16}{9} \frac{\pi}{3 - 2\gamma - 2 \ln \frac{3}{4} + 2 \ln 2 - \frac{1}{2} \ln \frac{\bar{E}_s}{E_b} + \frac{1}{2} \ln \frac{I_{b2}}{B^4}} \right) \quad (4.34)$$

Knowing that area moment of inertia is $I_{b2} = BH^3/12$ in out-of-plane direction, ε_{c2} is thus expressed as

$$\varepsilon_{c2} = \sqrt{\frac{1}{12}} \cdot \sqrt{\frac{\bar{E}_s}{E_b}} \cdot \sqrt{\frac{H}{B}} \left(\frac{9}{16} + \frac{16}{9} \frac{\pi}{3 - 2\gamma - 2 \ln \frac{3}{4} + \frac{1}{2} \ln \frac{4}{3} - \frac{1}{2} \ln \frac{\bar{E}_s}{E_b} + \frac{3}{2} \ln \frac{H}{B}} \right) \quad (4.35)$$

4.3 Competition on buckling mode

While the principle of least energy entails that the buckling mode of the system with a lower total potential energy is energetically favorable, the total potential energy is directly proportional to its critical buckling strain. Therefore, a comparison of the critical buckling strains for both in-plane and out-of-plane buckling systems is necessary. Figure 4.2 illustrates the critical buckling strains for both buckling systems as a function of aspect ratio (B/H) and properties ratio (\bar{E}_s/E_b) in a form of 3D surface plot.

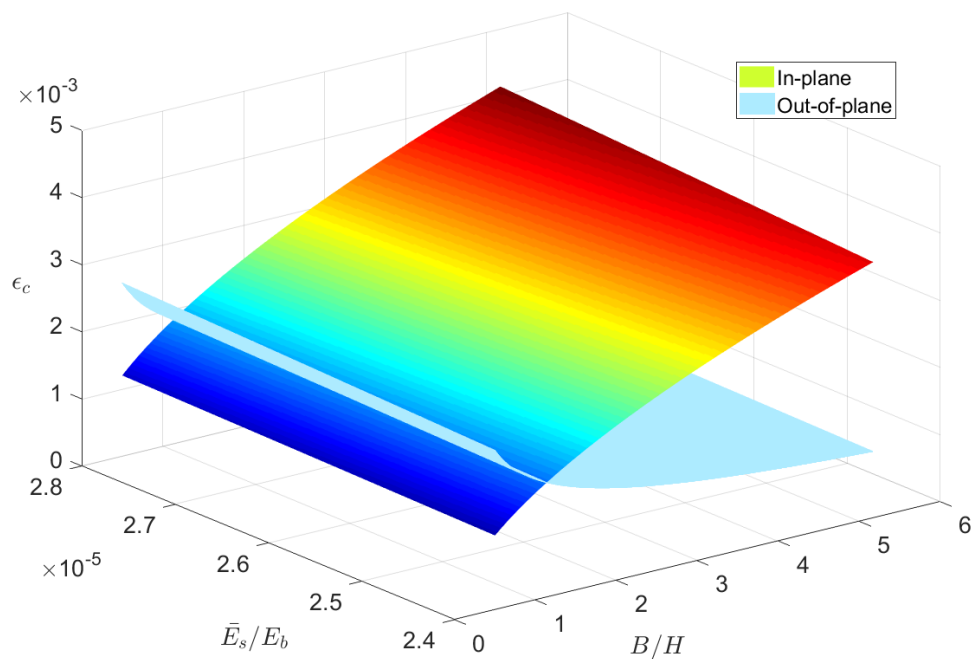


Figure 4.2: The critical in-plane-/out-of-plane buckling strain of a rectangular cross-section as a function of aspect ratio (B/H) and properties ratio (\bar{E}_s/E_b).

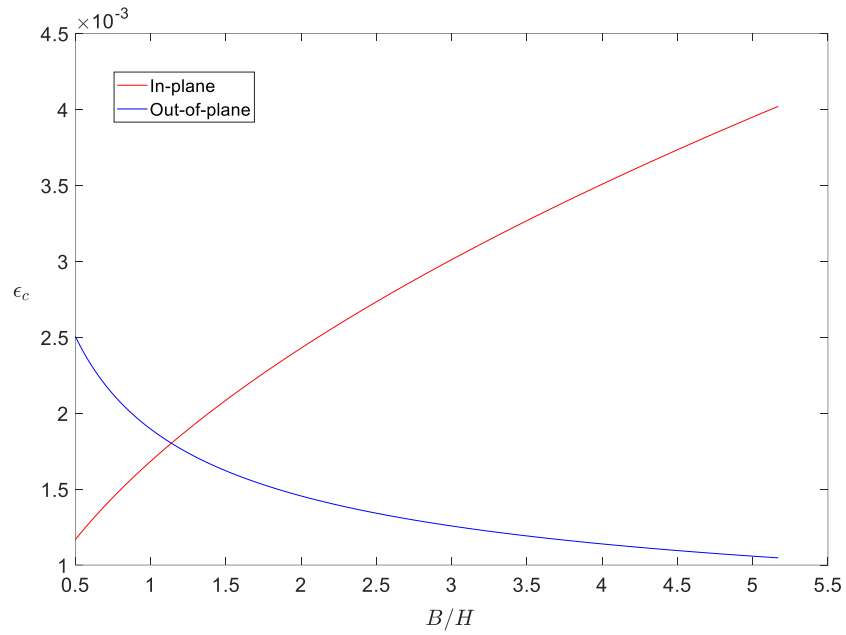


Figure 4.3: Critical in-plane-/out-of-plane buckling strain when $\bar{E}_s/E_b = 2.65 \times 10^{-5}$ ($E_s = 2$ MPa for PDMS substrate, and $E_b = 101$ GPa for effective Young's modulus of (40, 30) Si nanoribbon with core-sheath structure). Transition point occurs at $B/H \approx 1.138$.

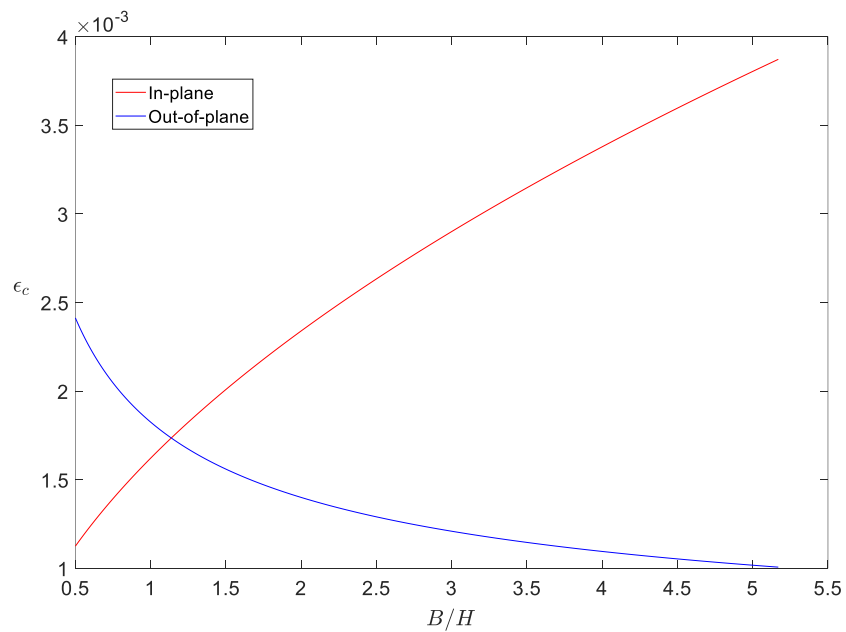


Figure 4.4: Critical in-plane-/out-of-plane buckling strain when $\bar{E}_s/E_b = 2.47 \times 10^{-5}$ ($E_s = 2$ MPa for PDMS substrate, and $E_b = 108$ GPa for effective Young's modulus of (200, 30) Si nanoribbon with core-sheath structure). Transition point occurs at $B/H \approx 1.137$.

For clarification purpose, Figure 4.3 and 4.4 show the critical buckling strain for a rectangular cross-section when $\bar{E}_s/E_b = 2.65 \times 10^{-5}$ and 2.47×10^{-5} respectively, which are corresponding to Si nanoribbons having width of 40 nm and 200 nm. Based on the minimum energy approach, both plots indicate that buckling mode transition point occurs at approximately $B/H \approx 1.14$. In other word, the analytical solution infers that out-of-plane buckling is more energetically favorable when $B/H \geq 1.14$, and vice versa.

CHAPTER 5: FINITE ELEMENT MODELING OF MECHANICAL BUCKLING

Even though continuum modeling are well-established as powerful tools to capture the mechanics of materials, calibration of modeling parameters with precise values derived from experiment is also critically important. Experimental approaches must be combined with a broad range of materials analytical techniques to yield full suite data necessary to elucidate the underlying mechanics-driven phenomenon.⁷⁶ Therefore, in this work, we intended to justify the observed buckling phenomenon of the individual silicon nanoribbons with finite element analysis (FEA). The computational work was divided into two sections where it began with modeling the pre-straining of PDMS substrate and followed by the buckling behavior of the Si nanoribbon.

5.1 Modeling pre-straining of PDMS substrate

To ensure that the computational modeling of the mechanical buckling of individual Si nanoribbons mimic the actual experiment, the simulation work began with modeling the pre-straining of the PDMS substrate using actual experimental data. The force and strain data captured by the Instron Bluehill 3 software were used as an input to simulate the substrate pre-straining.

5.1.1 Determining the substrate strain energy potential

It is well-known that polydimethylsiloxane (PDMS) is a widely used elastomer

which exhibits nonlinear hyperelastic behavior and its mechanical properties are highly dependent on the mixing ratio^{62,77,78} and curing conditions (*i.e.* curing temperature and duration)⁷⁹. Owing to its variable elastic properties, it is of paramount importance to identify the appropriate strain energy potential associated with the as-fabricated PDMS samples. To do this, the nonlinear material properties of PDMS were modeled from experimentally measured loading rate of the as-fabricated PDMS samples using Abaqus/CAE software (version 2016.HF2). In this work, the experimental data on a single 100% cyclic tension of the exact substrate were modeled with C3D20H element using various material models available in Abaqus. Out of a total of 17 models, ten models were identified as the prospective material formulations based on the “*Evaluate*” option provided in Abaqus. This option allows the users to perform standard tests with the experimental data using multiple strain energy potentials, and later make comparison to select the potential that provides the best fit.

The nonlinear fitting results for as-fabricated PDMS sample with the ten prospective strain energy potentials is shown in Figure 5.1. Based on three iterations, the results showed that only a few models were acceptable for the full range of strain region, namely third- and fourth-order Ogden, as well as fifth-order Reduced Polynomial, as clearly depicted in Figure 5.1 (c). The results were either too stiff or flexible in the measurement range using other strain energy potentials, as evidenced in Figure 5.1 (a-b). Considering the number of coefficients and average computational time required in the simulation (Figure 5.2), the third-order Ogden model is preferable over other models for the entire measurement range. More importantly, the nonlinear model of third-order Ogden model also matched the measured force-displacement curve well.

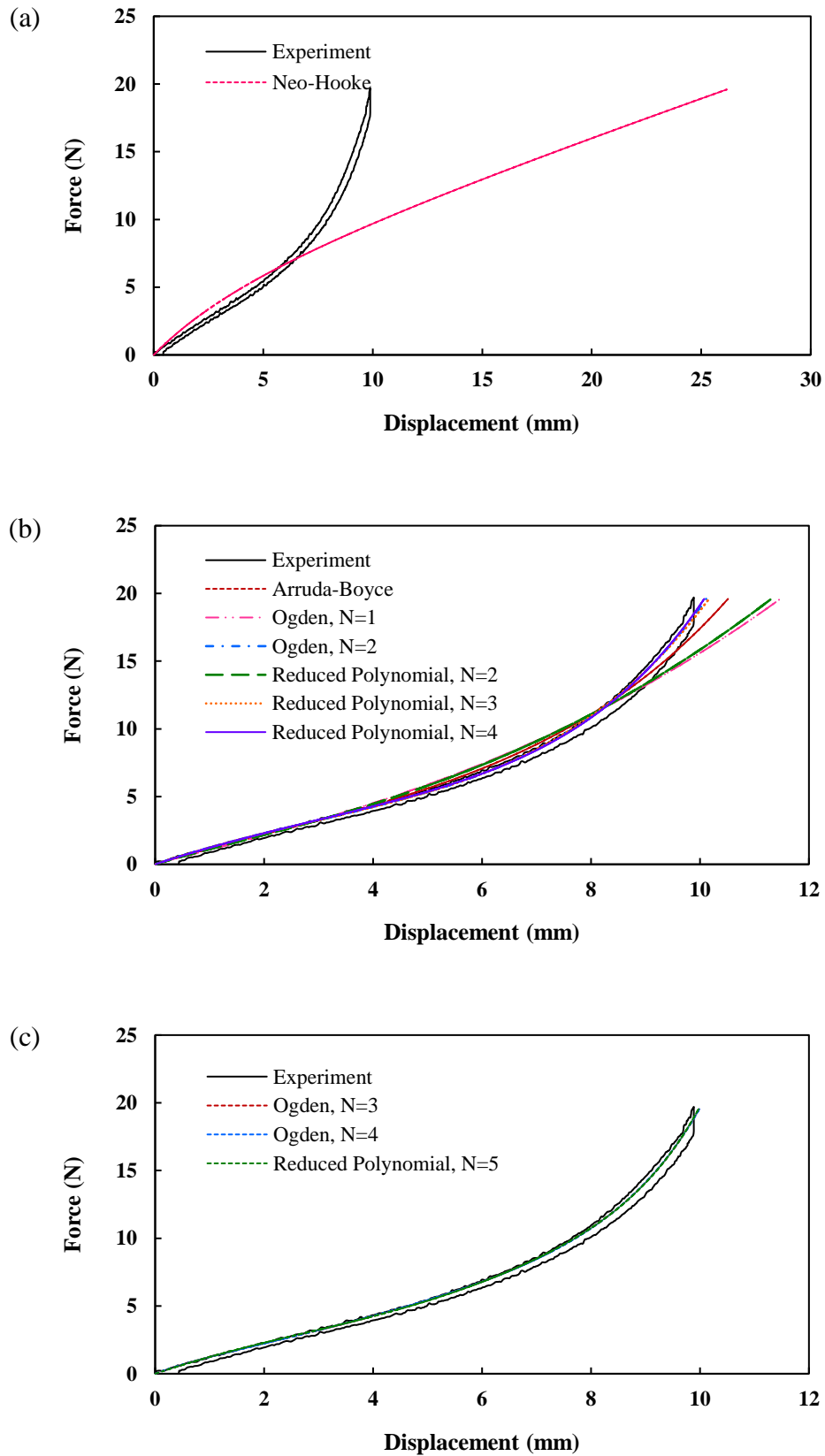


Figure 5.1: Comparison of nonlinear fitting results of PDMS sample using various material models available in Abaqus.

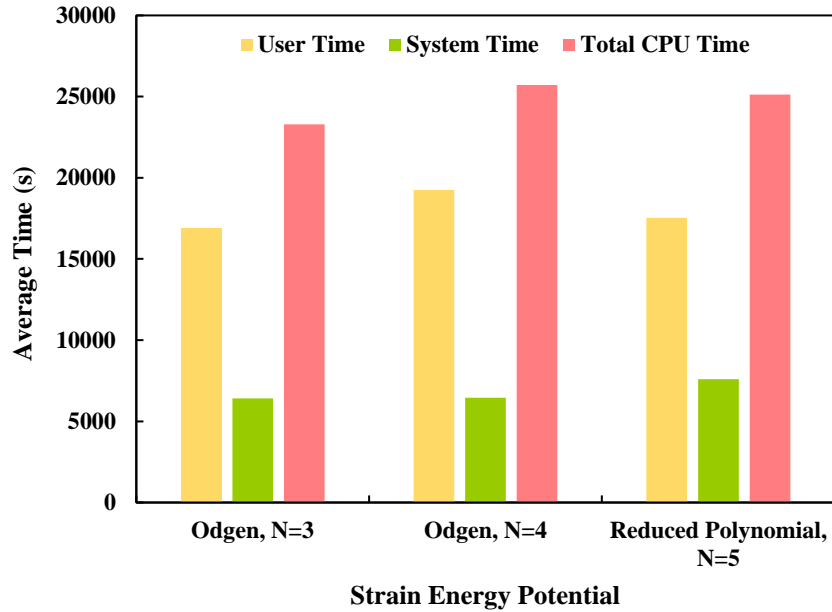


Figure 5.2: Comparison of computational time between various strain energy potentials associated with the simulation of PDMS substrate hyperelastic behavior.

It is noted that the pre-straining phenomenon of the PDMS substrate was initially modeled using experimentally measured loading rate as an input. Considering that strain rate of the substrate is the primary concern in this work instead of the loading rate, we later modeled the pre-straining phenomenon using the approach of forced displacement. Under the approach of forced displacement, we simplified the substrate model from a dumbbell structure into a rectangular block, which represented the gauge length region (length of 10 *mm*) of the original substrate. The computational model for the pre-strain of simplified substrate utilizing the approach of forced displacement is schematized in Figure 5.3 and the corresponding Cartesian coordinate system (o - xyz) is also included. The end surface of the z was fixed while displacement occurred at the opposite surface based on the experimentally measured strain rate. All the other surfaces were traction-free. The modeling output, that is the corresponding force-displacement curve of the simplified substrate model showed a good agreement to that

of the experimental data, as illustrated in Figure 5.4. Only a slight deviation was observed at the nonlinear and large strain region due to the boundary condition defined at the fixed end of the gauge length region as compared to that of the initial model. A maximum error of approximately 2.44% was detected at the mesh size of 0.5 mm and the error could be further minimized by employing finer mesh sizes. Therefore, mesh convergence analysis of the substrate was performed subsequently utilizing the simplified model together with the approach of forced displacement.

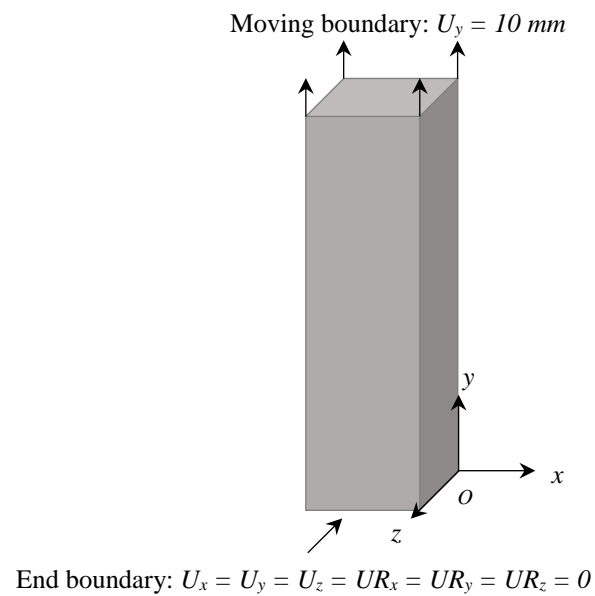


Figure 5.3: Boundary conditions applied in the finite element modeling of pre-strain of gauge length region of the PDMS substrate (*a.k.a.* simplified substrate).

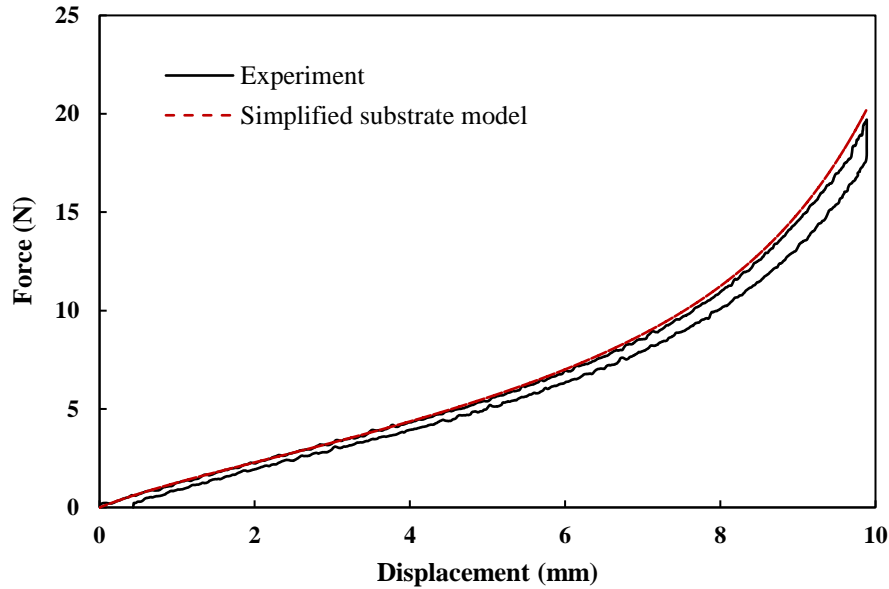


Figure 5.4: Force-displacement curve of pre-straining simplified substrate model agrees well to that of measured value.

5.1.2 Mesh convergence analysis on the substrate pre-straining

Mesh convergence analysis was carried out with the aim to ensure that the computational studies of buckling behavior of the beam/substrate system is reliable down to the nanoscale. In this work, convergence analysis was implemented for different mesh sizes, ranging between 0.05 – 0.5 mm. The mesh sizes were categorized into three groups, namely 0.1, 0.25, and 0.5 mm. It is noted that the entire pre-straining process (involving both tension and compression) took 357 seconds to complete and the transition occurred at the 184th second. Hence, the reaction force in y-axis experienced at the fixed end surface during the transition was used to compare to the maximum load of 19.7057 N recorded in the experiment as a form of mesh convergence evaluation. Table 5.1 indicates the dimensions at the moving end and reaction force at the fixed end surface of the 100% elongated substrate at various mesh sizes. Note that the length measurement is identical for all mesh sizes as the pre-strain of simplified

substrate model was computed based on forced displacement method and all models would eventually reach the same length.

Table 5.1: Dimensions and reaction force of 100% elongated substrate captured during the transition of tension-compression process, as a function of mesh size.

	Mesh size (mm)		
	0.1	0.25	0.5
Width (mm)	1.69358	1.69339	1.69293
Thickness (mm)	1.41131	1.41116	1.41088
Length (mm)	19.88692	19.88692	19.88692
Reaction force (N)	20.0688	20.1017	20.1870
Error (%)	1.84	2.01	2.44

5.1.3 Simplification of substrate pre-straining model

For the sake of simplicity, we further modified of substrate pre-straining model by only taking into account of the compression step. In other word, we modeled the substrate in its elongated form and later subjected it to an equivalent compressive strain. Dimensions outlined in Table 5.1 was employed to model the elongated substrate. Boundary conditions were defined as highlighted in Figure 5.5 to prevent rotation but allow surface expansion during the compression.

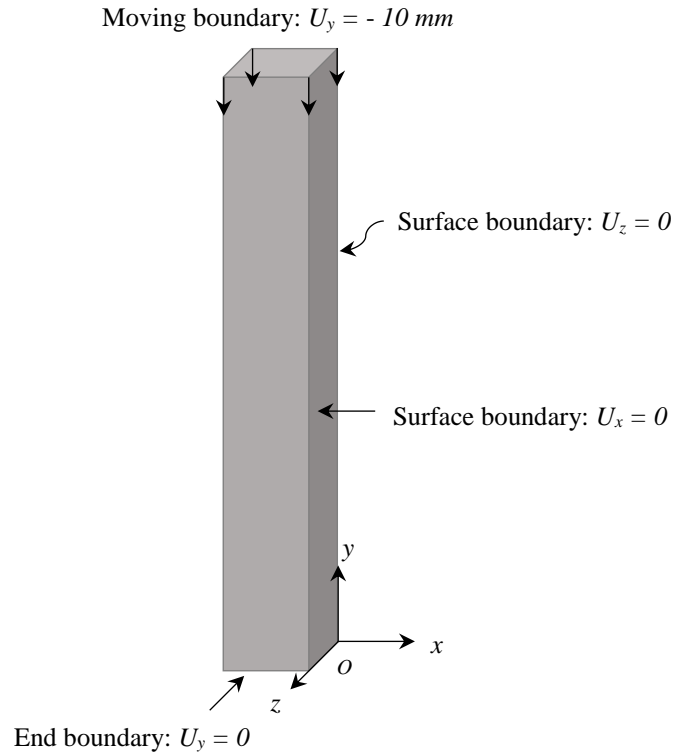


Figure 5.5: Boundary conditions applied in the finite element modeling of compression of an elongated gauge length region of the PDMS substrate.

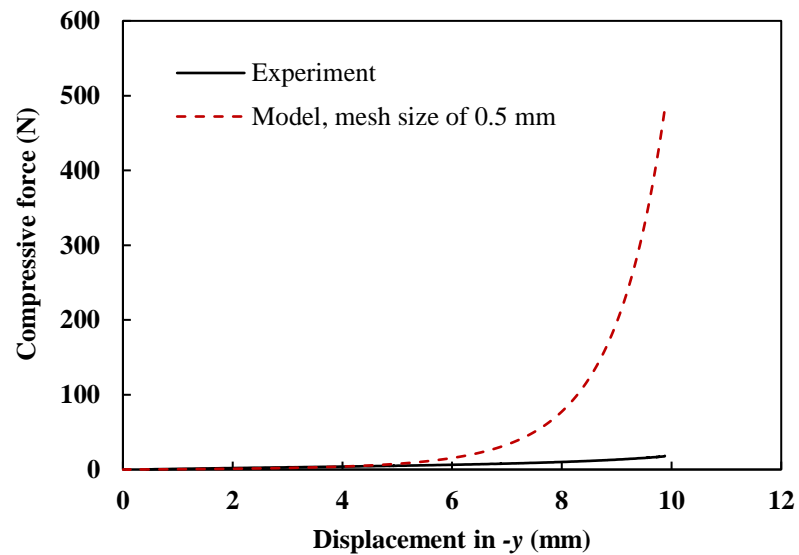


Figure 5.6: Comparison of force-displacement curve of substrate under compression between actual and simulation.

The simulation outcome showed that the substrate model was successfully compressed to half of its length without any surface wrinkling, however, the maximum load registered spiked to beyond 480 N, which is 25 times more than the actual load, as shown in Figure 5.6. We noted that a huge discrepancy existed on the compressive force due to the fact that the presence of internal stresses in the actual substrate upon tension were not considered in the simulation. Though so, since our primary concern was the strain rate and surface stability of the compressed substrate for the subsequent simulation work, the error in the maximum load became negligible.

Meanwhile, mesh convergence analysis was also conducted for four groups of mesh size by gauging the difference between original and final dimensions of the simplified substrate model. Original dimensions refer to dimensions prior to the application of tensile force while the final ones denote that of at the end of the compression. Table 5.2 clearly implies that the results are converging for all mesh sizes with an error of approximately 0.5%.

Table 5.2: Mesh convergence analysis of compressed substrate based on its width and thickness dimensions.

Mesh size (mm)	Dimension	Original (mm)	Final (mm)	Error (%)
0.5	Width	2.4	2.38696	0.543
	Thickness	2.0	1.98912	0.544
0.25	Width	2.4	2.38804	0.499
	Thickness	2.0	1.99003	0.498
0.1	Width	2.4	2.38830	0.487
	Thickness	2.0	1.99024	0.487

5.2 Modeling mechanical buckling of Si nanoribbons

Having the appropriate deformation scheme of the substrate, we can now proceed to model the buckling behavior of the Si nanoribbons on the compliant substrate. To further improve the computational time, only half of one-hundredth of the size of the actual substrate gauge length region was simulated in the subsequent buckling analysis. Though so, the substrate dimensions were carefully chosen to be sufficiently large, *i.e.* more than two orders of magnitude larger than the thickness of the nanoribbon, such that the solutions are insensitive to either the substrate size or external boundary conditions.

The elongated substrate was modeled with square cross-section of $8 \times 8 \mu\text{m}$ and a length of $100 \mu\text{m}$ whilst the nanoribbon has a core-sheath structure with a rectangular cross-section. Substrate and ribbon were modeled as solid with C3D20H and C3D20 element, respectively. Unlike the previous literature^{17,28,58}, the ribbon was not perfectly bonded to the substrate surface, instead both were only bonded at the ribbon ends using “tie” constraints in the Abaqus software. Additionally, the interfacial properties were defined in terms of friction coefficient and shear stress at the interface. Static friction coefficient and shear stress between Si nanowires and PDMS substrate obtained from the literature⁵² were used in the simulation.

However, at this point, the buckling behavior of the Si nanoribbons having core-sheath structure has not been successfully simulated. By using the contact properties values obtained from the literature, the ribbons were only seen to slide off the substrate surface instead of undergoing buckling deformation, upon the application of compressive stress. Further refinement on the contact properties between the two constituents and calibration of the model are needed to ensure the appropriate buckling behavior of the Si nanoribbons are being computed.

CHAPTER 6: CONCLUSIONS & FUTURE WORK

6.1 Conclusions

With the aim to comprehend the buckling-based metrology, we have performed investigation on the effect of aspect ratio, along with the consideration on core-sheath structure, on the buckling profile of individual silicon nanoribbons on an elastomeric substrate under mechanical buckling approach. Interfacial adhesion between the ribbons and the substrate was also enhanced through UVO surface treatment of the substrate and its effect on the ribbon buckling behavior was studied. On top of that, analytical solution adopted from the literature was also employed to understand the buckling phenomenon of the individual Si nanoribbons. Though finite element modeling (FEM) was anticipated to enhance the understanding of the buckling behavior under finite strain, the simulation work has not been successful at this moment. The following conclusions were obtained based on our studies.

On the pristine elastomeric substrate, the individual silicon nanoribbons exhibited increased buckling wavelength with the increase of aspect ratio, owing to the greater effective Young's modulus in larger ribbons. In terms of buckling mode, three forms of buckling mode were observed in this work. While ribbons having aspect ratio $B/H < 1.20$ demonstrated in-plane buckling mode, ribbons with aspect ratio greater than 1.20 exhibited out-of-plane buckling mode. The findings agreed well with the adopted analytical solution which suggested that $B/H \approx 1.14$ is transition point of the buckling mode. Meanwhile, two variants of out-of-plane buckling mode was observed in this work, *i.e.* incline-to-plane and normal-to-plane. Owing to the asymmetrical feature of

the ribbons and application of 100% pre-strain, ribbons with $1.68 \leq B/H \leq 2.70$ buckled incline-to-plane with excessive incline angle with respect to the normal direction of substrate surface. In contrast, normal-to-plane buckling mode was predominant in ribbons having larger aspect ratio, *i.e.* $B/H = 5.12$ in our case, yet partial of the ribbons failed to buckle.

In response to the UVO treatment, the treatment duration appeared to impose trivial effect on the buckling profile due to the fact that UVO treatment did not cause severe alteration on the substrate bulk modulus, which may influence the buckling wavelength. In other word, the UVO treatment within 150 s imposed negligible effect on the ribbon buckling wavelength. Though so, the treatment seemed to improve the interfacial adhesion marginally whereby normal-to-plane buckling mode became partially possible on ribbons with aspect ratio 2.70 during treatment duration of 150 s, and all ribbons having aspect ratio 5.12 were able to buckle upon treatment. Ribbons having aspect ratio below 2.70 retained the inherent buckling mode upon treatment. On the other hand, transition of buckling mode as a function of treatment duration was not observed in this work owing to the unequal area moment of inertia of the ribbon structure.

6.2 Future work

Even though nanoribbons buckled under large strain, the intrinsic buckling mode is uncertain and whether further deformation occurs. Hence, in order to better understand the deformation of the nanoribbons having various aspect ratios under mechanical buckling of large strain, an *in-situ* test under the microscope would allow one to visualize the buckling phenomenon so that the critical buckling strain could be identified.

Whilst UVO surface treatment is a promising method to improve interfacial adhesion between ribbon and substrate, its effectiveness is highly dependent on the hydrophobic recovery rate which may be influenced by substrate surface condition (*e.g.* porosity and surface defects) and environmental condition (*e.g.* humidity and temperature). It is therefore important to assess the substrate surface condition prior to testing and a controlled test environment is recommended. Furthermore, in our context where UVO surface treatment of the substrate is performed under pre-strained condition, its wettability measurement and assessment of hydrophobic recovery should be carried out as such to provide a more representative measurement. In addition, evaluation on the static and kinetic friction of Si nanoribbons on the PDMS substrate (under both untreated and treated condition) is necessary to comprehend the contact properties which is important for the subsequent simulation work. Even though static friction of Si nanowires on UVO treated substrate have been reported in the literature, no work have been found on Si nanoribbons of various aspect ratios and having core-sheath structure.

In order to better adopt the existing models available in literature as a form of metrology, the nanostructures must have high level of structural perfection, and of relatively long length. This is because Newtonian mechanics used to describe the buckling behavior is known to be valid down to length scales of approximately 10 atomic spacing for defect-free materials.¹⁴ Furthermore, only small strain (*i.e.* pre-strain within linear elastic region of substrate used) is involved to cause buckling so that compressive force applied must not exceed van der Waals attraction which may cause delamination of nanostructures from substrate. Care should also be taken to ensure well alignment of nanostructures on the substrate along the axial loading direction, as well

as good interfacial adhesion in order to warrant the success of buckling-based metrology technique on 1D nanostructures to probe its elastic modulus.

REFERENCES

- 1 Cao, Y.-P., Zheng, X.-P., Li, B. & Feng, X.-Q. Determination of the elastic modulus of micro-and nanowires/tubes using a buckling-based metrology. *Scripta Materialia* **61**, 1044-1047 (2009).
- 2 Zhu, Y. Mechanics of Crystalline Nanowires: An Experimental Perspective. *Applied Mechanics Reviews* **69**, 010802 (2017).
- 3 Zhu, Y., Ke, C. & Espinosa, H. Experimental techniques for the mechanical characterization of one-dimensional nanostructures. *Experimental Mechanics* **47**, 7-24 (2007).
- 4 Tan, E. & Lim, C. Mechanical characterization of nanofibers—A review. *Composites Science and Technology* **66**, 1102-1111 (2006).
- 5 Gianola, D. & Eberl, C. Micro-and nanoscale tensile testing of materials. *JOM Journal of the Minerals, Metals and Materials Society* **61**, 24-35 (2009).
- 6 Ding, W., Calabri, L., Chen, X., Kohlhaas, K. M. & Ruoff, R. S. Mechanics of crystalline boron nanowires. *Composites Science and Technology* **66**, 1112-1124 (2006).
- 7 Qin, Q., Xu, F., Cao, Y., Ro, P. I. & Zhu, Y. Measuring true Young's modulus of a cantilevered nanowire: effect of clamping on resonance frequency. *Small* **8**, 2571-2576 (2012).
- 8 Murphy, K. F., Chen, L. Y. & Gianola, D. S. Effect of organometallic clamp properties on the apparent diversity of tensile response of nanowires. *Nanotechnology* **24**, 235704 (2013).
- 9 Stafford, C. M. *et al.* A buckling-based metrology for measuring the elastic moduli of polymeric thin films. *Nature materials* **3**, 545-550 (2004).
- 10 Stafford, C. M., Vogt, B. D., Harrison, C., Julthongpiput, D. & Huang, R. Elastic moduli of ultrathin amorphous polymer films. *Macromolecules* **39**, 5095-5099 (2006).
- 11 Wilder, E. A., Guo, S., Lin-Gibson, S., Fasolka, M. J. & Stafford, C. M. Measuring the modulus of soft polymer networks via a buckling-based metrology. *Macromolecules* **39**, 4138-4143 (2006).
- 12 Ryu, S. Y. *et al.* Lateral buckling mechanics in silicon nanowires on elastomeric substrates. *Nano letters* **9**, 3214-3219 (2009).
- 13 Xiao, J. *et al.* Mechanics of nanowire/nanotube in-surface buckling on elastomeric substrates. *Nanotechnology* **21**, 085708 (2010).

- 14 Khang, D.-Y. *et al.* Molecular scale buckling mechanics in individual aligned single-wall carbon nanotubes on elastomeric substrates. *Nano letters* **8**, 124-130 (2008).
- 15 Xiao, J. *et al.* Mechanics of buckled carbon nanotubes on elastomeric substrates. *Journal of Applied Physics* **104**, 033543 (2008).
- 16 Jiang, H. *et al.* Finite width effect of thin-films buckling on compliant substrate: experimental and theoretical studies. *Journal of the Mechanics and Physics of Solids* **56**, 2585-2598 (2008).
- 17 Chen, Y., Liu, Y., Yan, Y., Zhu, Y. & Chen, X. Helical coil buckling mechanism for a stiff nanowire on an elastomeric substrate. *Journal of the Mechanics and Physics of Solids* **95**, 25-43 (2016).
- 18 Khang, D. Y., Rogers, J. A. & Lee, H. H. Mechanical buckling: mechanics, metrology, and stretchable electronics. *Advanced Functional Materials* **19**, 1526-1536 (2009).
- 19 Bowden, N., Brittain, S., Evans, A. G., Hutchinson, J. W. & Whitesides, G. M. Spontaneous formation of ordered structures in thin films of metals supported on an elastomeric polymer. *Nature* **393**, 146-149 (1998).
- 20 Chen, C. M. & Yang, S. Wrinkling instabilities in polymer films and their applications. *Polymer International* **61**, 1041-1047 (2012).
- 21 Kim, H. S. & Crosby, A. J. Solvent-Responsive Surface via Wrinkling Instability. *Advanced materials* **23**, 4188-4192 (2011).
- 22 Kish, A. & Samavedam, G. Track buckling prevention: theory, safety concepts, and applications. (2013).
- 23 Yang, S., Khare, K. & Lin, P. C. Harnessing surface wrinkle patterns in soft matter. *Advanced Functional Materials* **20**, 2550-2564 (2010).
- 24 Huck, W. T. *et al.* Ordering of spontaneously formed buckles on planar surfaces. *Langmuir* **16**, 3497-3501 (2000).
- 25 Chen, X. & Hutchinson, J. W. Herringbone buckling patterns of compressed thin films on compliant substrates. *Journal of applied mechanics* **71**, 597-603 (2004).
- 26 Chan, E. P. & Crosby, A. J. Fabricating microlens arrays by surface wrinkling. *Advanced Materials* **18**, 3238-3242 (2006).
- 27 Lin, P.-C. & Yang, S. Spontaneous formation of one-dimensional ripples in transit to highly ordered two-dimensional herringbone structures through sequential and unequal biaxial mechanical stretching. *Applied Physics Letters* **90**, 241903 (2007).

- 28 Song, J. *et al.* Buckling of a stiff thin film on a compliant substrate in large deformation. *International Journal of Solids and Structures* **45**, 3107-3121 (2008).
- 29 Chung, J. Y., Nolte, A. J. & Stafford, C. M. Surface Wrinkling: A Versatile Platform for Measuring Thin-Film Properties. *Advanced materials* **23**, 349-368 (2011).
- 30 Volynskii, A., Bazhenov, S., Lebedeva, O. & Bakeev, N. Mechanical buckling instability of thin coatings deposited on soft polymer substrates. *Journal of materials science* **35**, 547-554 (2000).
- 31 Jiang, H. *et al.* Finite deformation mechanics in buckled thin films on compliant supports. *Proceedings of the National Academy of Sciences* **104**, 15607-15612 (2007).
- 32 Tahk, D., Lee, H. H. & Khang, D.-Y. Elastic moduli of organic electronic materials by the buckling method. *Macromolecules* **42**, 7079-7083 (2009).
- 33 Cranston, E. D. *et al.* Determination of Young's modulus for nanofibrillated cellulose multilayer thin films using buckling mechanics. *Biomacromolecules* **12**, 961-969 (2011).
- 34 Rodriquez, D. *et al.* Comparison of Methods for Determining the Mechanical Properties of Semiconducting Polymer Films for Stretchable Electronics. *ACS Applied Materials & Interfaces* **9**, 8855-8862 (2017).
- 35 Duan, Y., Huang, Y. & Yin, Z. Competing buckling of micro/nanowires on compliant substrates. *Journal of Physics D: Applied Physics* **48**, 045302 (2015).
- 36 Morales, A. M. & Lieber, C. M. A laser ablation method for the synthesis of crystalline semiconductor nanowires. *Science* **279**, 208-211 (1998).
- 37 Ye, H., Titchenal, N., Gogotsi, Y. & Ko, F. SiC nanowires synthesized from electrospun nanofiber templates. *Advanced materials* **17**, 1531-1535 (2005).
- 38 Gordon, M. J., Baron, T., Dhalluin, F., Gentile, P. & Ferret, P. Size effects in mechanical deformation and fracture of cantilevered silicon nanowires. *Nano letters* **9**, 525-529 (2009).
- 39 Liu, F. *et al.* Individual boron nanowire has ultra-high specific Young's modulus and fracture strength as revealed by in situ transmission electron microscopy. *ACS nano* **7**, 10112-10120 (2013).
- 40 Ma, J., Liu, Y., Hao, P., Wang, J. & Zhang, Y. Effect of different oxide thickness on the bending Young's modulus of SiO₂@ SiC nanowires. *Scientific reports* **6** (2016).
- 41 Wang, N., Tang, Y., Zhang, Y., Lee, C. S. & Lee, S. Nucleation and growth of Si nanowires from silicon oxide. *Physical Review B* **58**, R16024 (1998).

- 42 Wang, Z. L. Mechanical properties of nanowires and nanobelts. *Dekker Encyclopedia of Nanoscience and Nanotechnology*, 1773-1786 (2004).
- 43 Duan, Y., Huang, Y., Yin, Z., Bu, N. & Dong, W. Non-wrinkled, highly stretchable piezoelectric devices by electrohydrodynamic direct-writing. *Nanoscale* **6**, 3289-3295 (2014).
- 44 Xu, F., Lu, W. & Zhu, Y. Controlled 3D buckling of silicon nanowires for stretchable electronics. *Acs Nano* **5**, 672-678 (2010).
- 45 Sun, Y. & Rogers, J. A. Structural forms of single crystal semiconductor nanoribbons for high-performance stretchable electronics. *Journal of Materials Chemistry* **17**, 832-840 (2007).
- 46 Efimenko, K., Wallace, W. E. & Genzer, J. Surface modification of Sylgard-184 poly (dimethyl siloxane) networks by ultraviolet and ultraviolet/ozone treatment. *Journal of colloid and interface science* **254**, 306-315 (2002).
- 47 Oláh, A., Hillborg, H. & Vancso, G. J. Hydrophobic recovery of UV/ozone treated poly (dimethylsiloxane): adhesion studies by contact mechanics and mechanism of surface modification. *Applied Surface Science* **239**, 410-423 (2005).
- 48 Bodas, D. & Khan-Malek, C. Hydrophilization and hydrophobic recovery of PDMS by oxygen plasma and chemical treatment—An SEM investigation. *Sensors and Actuators B: Chemical* **123**, 368-373 (2007).
- 49 Bacharouche, J., Haidara, H., Kunemann, P., Vallat, M.-F. & Roucoules, V. Singularities in hydrophobic recovery of plasma treated polydimethylsiloxane surfaces under non-contaminant atmosphere. *Sensors and Actuators A: Physical* **197**, 25-29 (2013).
- 50 Özçam, A. E., Efimenko, K. & Genzer, J. Effect of ultraviolet/ozone treatment on the surface and bulk properties of poly (dimethyl siloxane) and poly (vinylmethyl siloxane) networks. *Polymer* **55**, 3107-3119 (2014).
- 51 Shamsavan, H., Quinn, J., d'Eon, J. & Zhao, B. Surface modification of polydimethylsiloxane elastomer for stable hydrophilicity, optical transparency and film lubrication. *Colloids and Surfaces A: Physicochemical and Engineering Aspects* **482**, 267-275 (2015).
- 52 Qin, Q. & Zhu, Y. Static friction between silicon nanowires and elastomeric substrates. *ACS nano* **5**, 7404-7410 (2011).
- 53 Waddell, E. A. *et al.* Surface modification of Sylgard 184 polydimethylsiloxane by 254nm excimer radiation and characterization by contact angle goniometry, infrared spectroscopy, atomic force and scanning electron microscopy. *Applied Surface Science* **254**, 5314-5318 (2008).
- 54 Hillborg, H., Tomczak, N., Oláh, A., Schönherr, H. & Vancso, G. J. Nanoscale hydrophobic recovery: A chemical force microscopy study of UV/ozone-treated cross-linked poly (dimethylsiloxane). *Langmuir* **20**, 785-794 (2004).

- 55 Duffy, D. C., McDonald, J. C., Schueller, O. J. & Whitesides, G. M. Rapid prototyping of microfluidic systems in poly (dimethylsiloxane). *Analytical chemistry* **70**, 4974-4984 (1998).
- 56 Childs, W. R., Motala, M. J., Lee, K. J. & Nuzzo, R. G. Masterless Soft Lithography: Patterning UV/Ozone- Induced Adhesion on Poly (dimethylsiloxane) Surfaces. *Langmuir* **21**, 10096-10105 (2005).
- 57 Bakos, T., Rashkeev, S. & Pantelides, S. Reactions and diffusion of water and oxygen molecules in amorphous SiO₂. *Physical review letters* **88**, 055508 (2002).
- 58 Chen, Y., Zhu, Y., Chen, X. & Liu, Y. Mechanism of the transition from in-plane buckling to helical buckling for a stiff nanowire on an elastomeric substrate. *Journal of Applied Mechanics* **83**, 041011 (2016).
- 59 Kim, J., Chaudhury, M. K. & Owen, M. J. Hydrophobic recovery of polydimethylsiloxane elastomer exposed to partial electrical discharge. *Journal of Colloid and Interface Science* **226**, 231-236 (2000).
- 60 Eddington, D. T., Puccinelli, J. P. & Beebe, D. J. Thermal aging and reduced hydrophobic recovery of polydimethylsiloxane. *Sensors and Actuators B: Chemical* **114**, 170-172 (2006).
- 61 Yang, L. *et al.* Thermal conductivity of individual silicon nanoribbons. *Nanoscale* **8**, 17895-17901 (2016).
- 62 Khanafer, K., Duprey, A., Schlicht, M. & Berguer, R. Effects of strain rate, mixing ratio, and stress-strain definition on the mechanical behavior of the polydimethylsiloxane (PDMS) material as related to its biological applications. *Biomedical microdevices* **11**, 503 (2009).
- 63 Torres, J. M., Stafford, C. M. & Vogt, B. D. Manipulation of the Elastic Modulus of Polymers at the Nanoscale: Influence of UV- Ozone Cross-Linking and Plasticizer. *ACS nano* **4**, 5357-5365 (2010).
- 64 Rogers, J., Lagally, M. & Nuzzo, R. Synthesis, assembly and applications of semiconductor nanomembranes. *Nature* **477**, 45 (2011).
- 65 Yang, Y. *et al.* in *ASME 2012 International Mechanical Engineering Congress and Exposition*. 2765-2767 (American Society of Mechanical Engineers).
- 66 Pawley, J. B. & Masters, B. R. Handbook of biological confocal microscopy. *Journal of biomedical optics* **13**, 029902 (2008).
- 67 Gao, F., Liu, H., Sheng, C., Zhu, C. & Zhu, S. Refractive index sensor based on the leaky radiation of a microfiber. *Optics express* **22**, 12645-12652 (2014).
- 68 Sung, L.-P., Jasmin, J., Gu, X., Nguyen, T. & Martin, J. W. Use of laser scanning confocal microscopy for characterizing changes in film thickness and

- local surface morphology of UV-exposed polymer coatings. *Journal of Coatings Technology and Research* **1**, 267-276 (2004).
- 69 Hu, S., Cho, J.-H. & Gracias, D. H. in *Three-Dimensional Nanoarchitectures* 1-28 (Springer, 2011).
- 70 Pilkey, W. D. *Analysis and design of elastic beams: Computational methods*. (John Wiley & Sons, 2002).
- 71 Koh, C. *et al.* Edge effects in buckled thin films on elastomeric substrates. *Applied Physics Letters* **91**, 133113 (2007).
- 72 Baca, A. J. *et al.* Printable single-crystal silicon micro/nanoscale ribbons, platelets and bars generated from bulk wafers. *Advanced Functional Materials* **17**, 3051-3062 (2007).
- 73 Childs, W. R. & Nuzzo, R. G. Decal transfer microlithography: a new soft-lithographic patterning method. *Journal of the American Chemical Society* **124**, 13583-13596 (2002).
- 74 Song, J., Tranchida, D. & Vancso, G. J. Contact mechanics of UV/ozone-treated PDMS by AFM and JKR testing: mechanical performance from nano- to micrometer length scales. *Macromolecules* **41**, 6757-6762 (2008).
- 75 Huang, Z., Hong, W. & Suo, Z. Nonlinear analyses of wrinkles in a film bonded to a compliant substrate. *Journal of the Mechanics and Physics of Solids* **53**, 2101-2118 (2005).
- 76 Xu, B. & Rogers, J. A. Mechanics-driven approaches to manufacturing—A perspective. *Extreme Mechanics Letters* **7**, 44-48 (2016).
- 77 Wang, Z., Volinsky, A. A. & Gallant, N. D. Crosslinking effect on polydimethylsiloxane elastic modulus measured by custom-built compression instrument. *Journal of Applied Polymer Science* **131** (2014).
- 78 Schneider, F., Fellner, T., Wilde, J. & Wallrabe, U. Mechanical properties of silicones for MEMS. *Journal of Micromechanics and Microengineering* **18**, 065008 (2008).
- 79 Johnston, I., McCluskey, D., Tan, C. & Tracey, M. Mechanical characterization of bulk Sylgard 184 for microfluidics and microengineering. *Journal of Micromechanics and Microengineering* **24**, 035017 (2014).